JAQUELINE DE PAULA REZENDE

INTERAÇÕES INTERMOLECULARES ENTRE ESTRUTURAS SUPRAMOLECULARES E MOLÉCULAS DE INTERESSE NA ÁREA DE ALIMENTOS

Tese apresentada à Universidade Federal de Viçosa, como parte das exigências do Programa de Pós-Graduação em Ciência e Tecnologia de Alimentos, para obtenção do título de *Doctor Scientiae*.

Orientadora: Ana Clarissa dos Santos Pires

Coorientadores: Luis Henrique Mendes da Silva

Márcia Cristina T. R. Vidigal

VIÇOSA - MINAS GERAIS
2019

Ficha catalográfica preparada pela Biblioteca Central da Universidade Federal de Viçosa - Câmpus Viçosa

T
R467i
2019

Rezende, Jaqueline de Paula, 1991-
Interações intermoleculares entre estruturas supramoleculares e moléculas de interesse na área de alimentos / Jaqueline de Paula Rezende. – Viçosa, MG, 2019.
93 f. : il. (algumas color.) ; 29 cm.

Orientador: Ana Clarissa dos Santos Pires.
Tese (doutorado) - Universidade Federal de Viçosa.
Inclui bibliografia.

1. Forças intermoleculares. 2. Nanoestruturas. 3. Detectores. 4. Proteínas transportadoras. I. Universidade Federal de Viçosa. Departamento de Tecnologia de Alimentos. Programa de Pós-Graduação em Ciência e Tecnologia de Alimentos. II. Título.

CDD 22. ed. 541.226

JAQUELINE DE PAULA REZENDE

INTERAÇÕES INTERMOLECULARES ENTRE ESTRUTURAS SUPRAMOLECULARES E MOLÉCULAS DE INTERESSE NA ÁREA DE ALIMENTOS

Tese apresentada à Universidade Federal de Viçosa, como parte das exigências do Programa de Pós-Graduação em Ciência e Tecnologia de Alimentos, para obtenção do título de *Doctor Scientiae*.

APROVADA: 06 de novembro de 2019.

Assentimento:

Jaqueline de Paula Rezende
Autora

Ana Clarissa dos Santos Pires
Orientadora

AGRADECIMENTOS

A Deus, por estar sempre comigo, meu melhor amigo, por guiar meus passos e me dar força para superar as dificuldades.

À Universidade Federal de Viçosa, através do Departamento de Ciência e Tecnologia de Alimentos, pela oportunidade de realização do doutorado.

À Coordenação de Aperfeiçoamento de Pessoal de Nível Superior (CAPES) pela concessão da bolsa de estudo. À Fundação de Amparo a Pesquisa do Estado de Minas Gerais (FAPEMIG) e ao Conselho Nacional de Desenvolvimento Científico e Tecnológico (CNPq) pelo apoio financeiro ao projeto. O presente trabalho foi realizado com apoio da CAPES – Brasil – Código de Financiamento 001.

À professora Ana Clarissa, pela orientação, amizade, incentivo e confiança depositada em mim desde a graduação, por todas as oportunidades de aprendizados e trabalhos. Sua orientação ao longo desses nove anos contribuiu de maneira fundamental não só para a realização desse trabalho, mas também para o meu crescimento pessoal e profissional.

Ao professor Luis Henrique, pela coorientação, amizade, ensinamentos, sugestões, oportunidades e disponibilidade em ajudar sempre.

À professora Márcia, pela coorientação, disponibilidade, dedicação, ensinamentos e contribuições.

Às professoras Manoela e Raquel por aceitarem o convite para participar da banca de defesa e pelas sugestões.

Ao grupo THERMA que orgulhosamente fiz parte desde o seu início, onde aprendi fazer pesquisa com ética e seriedade. Aos colegas de laboratório, pelo companheirismo, parceria, momentos de estudo e descontração. Ao grupo QUIVECOM, pela parceria, colaboração e disponibilização de equipamentos.

Ao laboratório de embalagens, Labem, pelas amizades e disponibilização de equipamentos. Aos meus amigos de Viçosa e a todos que contribuíram de alguma forma para essa conquista, muito obrigada!

Aos meus queridos pais Luiz Carlos e Adair, pelo amor, apoio, confiança, por serem meus exemplos de determinação e pela motivação incondicional. Às minhas queridas irmãs Juliana e Cristiane e meu cunhado Leonardo, pelo carinho, conselhos e apoio de sempre. Vocês serão sempre as razões de todos os meus esforços e motivos das minhas vitórias. À vocês, dedico esse trabalho!

"Dar o exemplo não é a melhor maneira de influenciar os outros – é a única."

Albert Schweitzer

RESUMO

REZENDE, Jaqueline de Paula, D.Sc., Universidade Federal de Viçosa, novembro de 2019. **Interações intermoleculares entre estruturas supramoleculares e moléculas de interesse na área de alimentos.** Orientadora: Ana Clarissa dos Santos Pires. Coorientadores: Luis Henrique Mendes da Silva e Márcia Cristina Teixeira Ribeiro Vidigal.

Estruturas supramoleculares são sistemas dinâmicos em razão da capacidade de modificar sua constituição em resposta a variações do meio circundante (solvente) e/ou de fatores físicos (temperatura, pressão, campo elétrico) e/ou interação com outras moléculas. Diante da diversidade constitucional e dinamismo dessas estruturas, é possível desenvolver novas estruturas com características e propriedades funcionais de interesse para a área de alimentos. O presente trabalho foi dividido em 3 artigos científicos e teve como objetivo desenvolver três estruturas supramoleculares, uma com capacidade sensora de detecção e duas como nanocarreadoras de moléculas hidrofóbicas. No primeiro artigo, o polidiacetileno (PDA) foi utilizado no desenvolvimento de sensores para detectar a presença do antibiótico enrofloxacina (ENRO) em meio aquoso, à 30 °C. As nanoestruturas sensoras, conhecidas como nanoblendas (NB), foram produzidas a partir da mistura de PDA, copolímeros tribloco (CT) e surfactante dodecil sulfato de sódio (SDS). As NBs de PDA/CT/SDS foram capazes de detectar ENRO em uma concentração cinco vezes menor do que o limite máximo permitido pela União Europeia. O aumento da sensibilidade do nanossensor que continha SDS foi atribuído à energia liberada a partir da interação intermolecular entre ENRO e SDS, favorecendo o processo de transição colorimétrica azul-vermelho do PDA. A metodologia de superfície de resposta mostrou que tanto a concentração de ENRO quanto de SDS influenciaram na resposta colorimétrica (RC) do sensor, sendo que a RC máxima obtida foi em [ENRO] = 2 μM e [SDS] = 14,6 mM. A taxa de transição colorimétrica também foi avaliada, sendo que a NB contendo 11,6 mM de SDS gastaria apenas 22 min para atingir 40% de RC, que é facilmente visível. O segundo artigo apresentou a termodinâmica e cinética de formação do complexo lactoferrina bovina (bLF) - epigalocatequina-3-galato (EGCG) obtidas pela técnica de ressonância plasmônica de superfície (SPR). A espectroscopia de fluorescência (FS) também foi empregada para obtenção dos dados termodinâmicos. A formação do complexo bLF-EGCG termodinamicamente estável ($\Delta G^o_{SPR} \approx$ -29,00 kJ mol^{-1}, $\Delta G^o_{FS} \approx$ -26,00 kJ mol^{-1}) em pH = 7,0 foi impulsionada entropicamente (ΔH^o_{SPR} = 14,26, ΔH^o_{FS} = 10,20 kJ mol^{-1} and $T\Delta S^o_{SPR} \approx$ 43,00, $T\Delta S^o_{FS} \approx$ 36,00 kJ mol^{-1}). Como os dados

termodinâmicos das duas técnicas foram similares, sugere-se que a interação entre as biomoléculas ocorreram em regiões próximas aos triptofanos presentes na proteína. O aumento da temperatura favoreceu a estabilidade do complexo bLF-EGCG causando aumento nas constantes de associação (k_a) e de dissociação (k_d) do complexo. No terceiro artigo foi avaliado o efeito da estrutura química do polifenol resveratrol (RES) na interação com a albumina do soro humano (HSA). Assim, os parâmetros cinéticos e termodinâmicos de formação de complexo entre a HSA e RES e um de seus análogos (RESAn1) foram avaliados por SPR. A constante de interação (K_b) e constantes cinéticas de associação (k_a) e dissociação (k_d) mostraram que a interação HSA-RESAn1 ($K_{b(HSA-RESAn1)}$~ 3,94 x 10^3 L mol^{-1}, $k_{a(HSA-RESAn1)}$~1,70 x 10^3 M^{-1} s^{-1}, $k_{d(HSA-RESAn1)}$~ 0,43 s^{-1}) foi mais intensa que HSA-RES ($K_{b(HSA-RES)}$~ 2,60 x 10^3 L mol^{-1}, $k_{a(HSA-RES)}$ ~ 1,20 x 10^3 $M^{-1}s^{-1}$, $k_{d(HSA-RES)}$~ 0,46 s^{-1}). A estrutura menos polar do RESAn1 em relação a do RES contribui para seu acesso às regiões hidrofóbicas no interior da HSA. A formação de ambos complexos foi entropicamente dirigida ($T\Delta S^0{}_{HSA-RES}$~ 33,8 and $T\Delta S^0{}_{HSA-RESAn1}$~ 56,4 KJ mol^{-1}) e favorecida com o aumento da temperatura. Esse estudo mostrou que pequenas mudanças na estrutura de um bioativo pode influenciar na sua interação com a HSA. Independente da finalidade das estruturas supramoleculares, os trabalhos buscaram avaliar e compreender as interações entre as moléculas que compõe o sistema, bem como, entre o sistema e moléculas presentes no meio em que se encontram. Portanto, o objetivo desses trabalhos foi fornecer dados que contribuam para a otimização do uso e aplicação das estruturas desenvolvidas.

Palavras-chave: Nanossensor ótico. Detecção de antibiótico. Termodinâmica de interação. Constantes cinéticas. Complexo ativado.

ABSTRACT

REZENDE, Jaqueline de Paula, D.Sc., Universidade Federal de Viçosa, November, 2019. **Intermolecular interactions between supramolecular structures and molecules of interest in the food**. Adviser: Ana Clarissa dos Santos Pires. Co-advisers: Luis Henrique Mendes da Silva and Márcia Cristina Teixeira Ribeiro Vidigal.

Supramolecular structures are dynamic systems because of ability to modify their constitution in response to variations in the surrounding environment (solvent) and / or physical factors (temperature, pressure, electric field) and / or interaction with other molecules. Faced with the constitutional diversity and dynamism of these structures, it is possible to develop new structures with functional characteristics and properties of interest to the food area. The present work was divided into 3 scientific articles and aimed to develop three supramolecular structures, one with sensing capacity and two as nanocarriers of hydrophobic molecules. In the first article, polydiacetylene (PDA) was used in the development of sensors to detect the presence of the antibiotic enrofloxacin (ENRO) in aqueous medium at 30 ° C. Sensor nanostructures, so-called nanoblends (NB), were produced from the mixture of PDA, triblock copolymers (TC) and sodium dodecyl sulfate surfactant (SDS). The PDA/ TC/ SDS NBs were able to detect ENRO at a concentration five times lower than the maximum limit allowed by the European Union. The increased sensitivity of the nanosensor containing SDS was attributed to the energy released from the intermolecular interaction between ENRO and SDS, favoring the blue-red colorimetric transition process of the PDA. The response surface methodology showed that both ENRO concentration and SDS influence the colorimetric response (CR) of the sensor, with the maximum CR obtained in [ENRO] = 2 μM and [SDS] = 14.6 mM. The colorimetric transition rate was also evaluated, and NB containing 11.6 mM SDS required only 22 min to reach 40% CR, which is easily visible. The second article presented the thermodynamics and kinetics of formation of bovine lactoferrin (bLF) - epigallocatechin-3-gallate (EGCG) complex obtained by surface plasmon resonance technique (SPR). Fluorescence spectroscopy (FS) was also used to obtain thermodynamic data. Formation of the thermodynamically stable bLF-EGCG complex ($\Delta G^o_{SPR} \approx$ -29.00 kJ mol^{-1}, $\Delta G^o_{FS} \approx$ -26.00 kJ mol^{-1}) at pH = 7.0 was entropically driven (ΔH^o_{SPR} = 14.26, ΔH^o_{FS} = 10.20 kJ mol^{-1} and $T\Delta S^o_{SPR} \approx$ 43.00, $T\Delta S^o_{FS} \approx$ 36.00 kJ mol^{-1}). As the thermodynamic data of the two techniques were similar, it is suggested that the interaction between the biomolecules occurred in regions close to the tryptophan present in the protein. The increase in temperature favored the stability of the bLF-EGCG complex

causing an increase in the association (k_a) and dissociation (k_d) constants of the complex. In the third article, the effect of the chemical structure of polyphenol resveratrol (RES) on interaction with human serum albumin (HSA) was evaluated. Thus, the kinetic and thermodynamic parameters of complex formation between HSA and RES and one of its analogs (RESAn1) were evaluated by SPR. The binding constant (K_b) and kinetic constants of association (k_a) and dissociation (k_d) showed that the HSA-ResAn1 interaction ($K_{b(HSA-ResAn1)}$~ 3.94 x 10^3 L mol^{-1}, $k_{a(HSA-ResAn1)}$~1.70 x 10^3 M^{-1} s^{-1}, $k_{d(HSA-ResAn1)}$~ 0.43 s^{-1}) was more intense than HSA-Res ($K_{b(HSA-Res)}$~ 2.60 x 10^3 L mol^{-1}, $k_{a(HSA-Res)}$ ~ 1.20 x 10^3 $M^{-1}s^{-1}$, $k_{d(HSA-Res)}$~ 0.46 s^{-1}). The less polar structure of ResAn1 relative to Res contributes to its access to the hydrophobic regions within the HSA. The formation of both complexes was entropically driven ($T\Delta S^0{}_{HSA-Res}$~ 33.8 and $T\Delta S^0{}_{HSA-ResAn1}$~ 56.4 KJ mol^{-1}) and favored with increasing temperature. This study showed that small changes in the structure of a bioactive may influence its interaction with the HSA. Regardless of the purpose of the supramolecular structures, the works sought to evaluate and understand the interactions between the molecules that make up the system, as well as between the system and molecules present in their environment. Therefore, the objective of these works was to provide data that contribute to the optimization of the use and application of the developed structures.

Keywords: Optical nanosensor. Antibiotic detection. Thermodynamic binding. Kinetic constants. Complex activated.

SUMÁRIO

INTRODUÇÃO GERAL

Estruturas supramoleculares são sistemas formados por moléculas ligadas por interações não-covalentes e, por isso são considerados sistemas naturalmente dinâmicos. Macromoléculas biológicas, tais como proteínas, carboidratos, lipídeos e ácidos nucléicos, participam da formação desse tipo de estrutura em organismos vivos. Dessa forma, a auto-organização dessas estruturas é considerado um dos processos fundamentais para a geração de matéria complexa e, consequentemente, para a evolução do universo (Gangemi, Puglisi, Pappalardo, & Trusso Sfrazzetto, 2018; Lehn, 2007).

As estruturas supramoleculares são capazes de modificar sua constituição por meio da associação, dissociação, troca ou reorganização de seus componentes em resposta a variações do meio circundante (solvente) e/ou dos fatores físicos (temperatura, pressão, campo elétrico) e/ou interação com outras moléculas. Esse caráter dinâmico e a grande diversidade constitucional tem atraído o interesse de pesquisadores para o desenvolvimento de novas estruturas com características e propriedades funcionais como base para a nanociência e nanotecnologia em diversas áreas (Lehn, 2007; Okesola & Smith, 2016; Zhou, Li, Du, & Xu, 2017).

Nanossensor é uma das formas de aplicação de estruturas supramoleculares na área de ciência e tecnologia de alimentos. A detecção de determinadas moléculas presentes em alimentos, tais como compostos alergênicos e contaminantes, é de grande interesse tanto para as indústrias como para a saúde do consumidor. Por exemplo, a enrofloxacina (ENRO) é um antibiótico muito utilizado para o tratamento de infecções, como a mastite, em bovinos leiteiros o que pode resultar na contaminação dos tecidos e biofluidos desses animais com resíduos de ENRO. A presença desse antibiótico em leite é prejudicial tanto para os consumidores, em caso de ingestão e desenvolvimento de resistência antimicrobiana, quanto para as indústrias, em razão do baixo rendimento e má qualidade dos produtos lácteos produzidos. Estruturas supramoleculares formadas a partir de polímeros, como o polidiacetileno e copolímeros tribloco, têm sido desenvolvidas para utilização como nanossensores colorimétricos. O polidiacetileno é um polímero que, além da capacidade de auto-organização, apresenta propriedades óticas que permite a mudança do comprimento de onda de máxima absorção em resposta a variações do meio que se encontra bem como na presença de determinadas moléculas. Essa alteração espectrofotométrica é conhecida como transição colorimétrica azul-vermelho e pode ser

observada visualmente (de Souza et al., 2016; Kang et al., 2012; Kwon et al., 2018; Mapazi, Matabola, Moutloali, & Ngila, 2017).

Outra aplicação das estruturas supramoleculares na área de alimentos envolve a pesquisa de compostos bioativos. Esses compostos presentes em pequenas quantidades nos alimentos são considerados bioativos por apresentarem propriedades benéficas à saúde humana. A epigalocatequina-3-galato (EGCG) e o resveratrol (RES) são exemplos de bioativos. EGCG é a principal catequina extraída do chá verde e apresenta a maior atividade antioxidante dentre as catequinas. O RES é encontrado principalmente em vinho tinto e possui propriedades antioxidantes, anti-inflamatória, antidiabética e também atua no combate à doenças neurodegenerativas. No entanto, apesar do potencial terapêutico desses dois polifenóis, a utilização deles é bastante limitada em razão da instabilidade à luz, ao calor e à variações de pH decorrentes do processo digestivo. Além disso, são pouco solúveis em água e, consequentemente, apresentam baixa biodisponibilidade (Foegeding, Plundrich, Schneider, Campbell, & Lila, 2017; Hu, Liu, Zhang, & Zeng, 2017; Rezaei, Fathi, & Jafari, 2019)

Sendo assim, o desenvolvimento de estruturas supramoleculares entre esses compostos e macromoléculas biológicas é uma estratégia para protegê-los contra degradação química. Proteínas globulares transportadoras, tais como a lactoferrina bovina (bLF) e a albumina do soro humano (HSA), possuem regiões hidrofóbicas e hidrofílicas em suas estruturas sendo macromoléculas estratégicas para essas finalidade (Faridi Esfanjani & Jafari, 2016; Hu et al., 2017). A formação de complexo entre essas proteínas e os polifenóis é uma maneira promissora para carrear esses compostos hidrofóbicos em meios hidrofílicos objetivando sua proteção química, aumento da solubilidade em água e biodisponibilidade.

Independente da finalidade das estruturas supramoleculares desenvolvidas, é fundamental conhecer as interações entre as moléculas que compõe o sistema, bem como, entre o sistema e moléculas presentes no meio em que se encontra. Esse conhecimento irá contribuir para potencializar as respectivas funcionalidades desejadas. Por exemplo, conhecer a termodinâmica e a cinética de formação de complexo proteína-bioativo é fundamental para otimizar as condições do uso desses complexos para diversas áreas, tais como, alimentícia, farmacológica e médica. No caso dos nanossensores colorimétricos, conhecer as forças motrizes que levam à transição de cor pode fornecer informações que

contribuem para aumentar sua sensibilidade e especificidade na detecção da molécula de interesse.

A termodinâmica de interação intermolecular pode ser caracterizada por diversas técnicas em diferentes condições experimentais. Quando a interação proteína-bioativo ocorre próximo à região dos sítios de aminoácidos fluoróforos da proteína, a técnica de espectroscopia de fluorescência (FS) permite a caracterização termodinâmica dessa interação. Por outro lado, a técnica de ressonância plasmônica de superfície (SPR) é capaz de fornecer os parâmetros termodinâmicos e cinéticos de interação independentemente do sítio de ligação da proteína envolvido na interação. Além disso, a técnica de SPR permite também a determinação de parâmetros cinéticos associados ao complexo ativado que contribuem para a compreensão da dinâmica de formação dos complexos proteína-bioativo.

Nesse contexto, além de visar a construção de sistemas supramoleculares funcionais, esse trabalho buscou determinar as forças motrizes de interação intermolecular envolvidas no processo de detecção de ENRO por nanossensores colorimétricos, bem como no processo de formação dos complexo bLF-EGCG e HSA-RES.

ARTICLE 1

Polydiacetylene/triblock copolymer/surfactant nanoblend: A simple and rapid method for the colorimetric screening of enrofloxacin residue

Article published in the journal *Food Chemistry*. doi:10.1016/j.foodchem.2018.12.033

Abstract

Colorimetric nanosensors formed of polydiacetylene (PDA), triblock copolymer (L64 or F68), and sodium dodecyl sulfate (SDS), so-called nanoblends, were developed to detect enrofloxacin (ENRO) in aqueous media. The nanosensors show hydrodynamic diameter ranging from 234.2 ± 3.5 to 801.6 ± 17.8 nm for SDS concentrations of 13.0–21.0 mM, respectively. The lowest limit of detection was 0.054 μM, which is five times smaller than the maximum limit allowed by the European Union. The response surfaces showed that both the SDS and ENRO concentrations influenced the colorimetric response (p<0.05), and kinetic rate of colorimetric transition (R_{CT}). SDS concentration between 11.0 and 14.0 mM in the nanoblend yielded the most sensitive nanosensors for detecting ENRO. When L64 was replaced by F68, the colorimetric response of the nanoblends was similar, but PDA/F68/SDS showed a slower R_{CT} than PDA/L64/SDS. The developed nanosensor is a sensitive and simple device for the fast detection of ENRO.

Keywords: Nanosensor; polydiacetylene; sodium dodecyl sulfate; triblock copolymer; antibiotic

Abbreviations

ENRO, enrofloxacin; PDA, polydiacetylene; SDS, sodium dodecyl sulfate; TCs, triblock copolymers; EO, ethylene oxide segment; PO, propylene oxide segment; L64, poly(ethylene oxide)-poly(propylene oxide)-poly(ethylene oxide) (molar mass of 2900 g mol^{-1}); F68, poly(ethylene oxide)-poly(propylene oxide)-poly(ethylene oxide) (molar mass of 8400 g mol^{-1}); LOD, limit of detection; CR, colorimetric response; R_{CT}, rate of colorimetric transition; ζ, zeta potential; D_h, hydrodynamic diameter; T_{tr}, temperature of chromatic transition; ΔE_{RB}, rotational energy barrier.

1. Introduction

Enrofloxacin (ENRO) is an antibiotic in the fluoroquinolone family. It is widely used in veterinary medicine to combat bacterial infections because of its broad antibacterial activity (Xu, Liu, Jia, & Shu, 2015). However, the use of this antibiotic to treat infections, such as mastitis, may result in the presence of ENRO residues in animal tissues and biofluids. The ingestion of antibiotic residues from the consumption of milk and dairy products is of great concern to human health, especially regarding antimicrobial resistance. Furthermore, the presence of antibiotics in milk causes losses in the food industry because of the low yield and quality of the manufactured products (Shi et al., 2018).

Therefore, detecting ENRO in foods of animal origin is extremely important for both the consumer and the food industry. Several methods for detecting ENRO have been developed including liquid chromatography (Choi et al., 2011; Lombardo-Agüí, García-Campaña, Cruces-Blanco, & Gámiz-Gracia, 2015; Terrado-Campos, Tayeb-Cherif, Peris-Vicente, Carda-Broch, & Esteve-Romero, 2017), terbium-sensitized luminescence (TSL) (Chen & Li, 2013), capillary electrophoresis (Lombardo-Agüí, García-Campaña, Gámiz-Gracia, & Cruces Blanco, 2010; Xu et al., 2015), and enzyme-linked immunosorbent assays (ELISA) (Chen et al., 2009; Huet et al., 2006; Zhang et al., 2011).

While these methods are accurate and sensitive, they require laborious sample preparation, sophisticated equipment, and significant expense; furthermore, they are time-consuming and can be environmentally damaging (Tian et al., 2016; Zhou et al., 2018). Hence, developing simple and rapid methods for the monitoring of ENRO residues in food would provide an important advance for controlling antibiotic residues in foods.

Polydiacetylenes (PDAs) are ene-yne conjugated polymers formed by the 1,4-addition of diacetylene monomers under ultraviolet radiation (254 nm). PDAs exhibit unique colorimetric properties, showing a blue–red colorimetric transition in response to different stimuli such as pH (Chanakul, Traiphol, Faisadcha, & Traiphol, 2014), temperature (Ferreira et al., 2018), as well as interactions with other molecules, such as organic solvents (Pattanatornchai, Charoenthai, Wacharasindhu, Sukwattanasinitt, & Traiphol, 2013; Pires et al., 2010), proteins (de Souza et al., 2016; Rezende et al., 2017), and some bacteria and viruses (Jiang et al., 2015; Pires et al., 2011).

PDAs can self-organize into different structures such as molecular films (García-Espejo et al., 2017) and vesicles (Shin, Shin, & Shin, 2017; Zhang et al., 2017; Zhang et al., 2018). Although vesicles have potential applications as colorimetric sensors with food applications (Pires et al., 2011), they show some limitations, such as low uniformity in their composition and organization (Ferreira et al., 2018). Recently, our research group developed new nanostructures formed of PDA and different triblock copolymers (TCs), called nanoblends, for use as nanosensors (de Souza et al., 2016; Ferreira et al., 2018; Rezende et al., 2017). These nanoblends present greater thermodynamic stability than PDA vesicles, and they do not require the use of organic solvents during their synthesis. In addition, their structures can be easily modulated, which allows the incorporation of several molecules within the sensor structure. It is well known that ENRO interacts with the anionic surfactant sodium dodecyl sulfate (SDS) (Seedher & Agarwal, 2009); hence, it could be used as a receptor molecule for ENRO to increase the sensor sensitivity of the nanoblends.

Therefore, in this study, we developed colorimetric nanoblends formed of PDA, TC (L64 or F68), and SDS for the detection of ENRO in aqueous media. In addition, we investigated the effect of SDS concentration on the nanosensor response, as well as exploring the effects of SDS and ENRO concentrations on the kinetics of the colorimetric transition of the nanoblends.

2. Material and methods

2.1. Materials

10,12-Pentacosadiynoic acid (97 wt%) was purchased from Fluka (USA). The TCs poly(ethylene oxide)-poly(propylene oxide)-poly(ethylene oxide) ($(EO)_n$-$(PO)_m$-$(EO)_n$) L64 and F68 (with average molar masses (M_m) of 2900 and 8400 g mol^{-1}, respectively), as well as sodium dodecyl sulfate (99 wt%) and enrofloxacin (98 wt%) were purchased from Sigma-Aldrich (USA). All chemicals were used without further purification. Milli-Q® water (EMD Millipore, Billerica, MA, USA) was used for the preparation of all solutions.

2.2. PDA nanosensor preparation

The nanoblends were prepared as described previously by de Souza et al., (2016), Ferreira et al., (2018), and Rezende et al., (2017) with some changes. PDA (1 mM) was dissolved in a TC/SDS solution containing a fixed concentration of TC (1%

w/w) but with different SDS concentrations (0, 13, 17, or 21 mM). This mixture was sonicated for 10 min (Sonics & Materials Inc., Model VC750, USA), and immediately filtered through a polyvinylidene fluoride (PVDF) filter. The suspension was kept at 4 °C for 12 to 72 h (depending on the SDS concentration) with the aim of orientating the PDA monomers to promote polymerization. Next, photopolymerization was carried out by exposing the suspension to UV radiation (254 nm) for 5 min until the suspension turned blue.

2.3. Characterization of the nanoblends

To characterize the nanoblends, we measured the zeta potential (ζ) and hydrodynamic diameter (D_h) of the nanostructures before and after the polymerization step using a Zetasizer Nano ZS90 (Malvern, UK). The samples were diluted 20 times to avoid the interference of the blue color on the measurements, and each experiment was repeated three times. The results are presented as the average of 10 measurements.

We also performed an analysis of the thermochromism of the nanoblends. The nanoblend samples were heated from 22 to 62 °C. The percentage of blue-to-red conversion of the PDAs was quantified by a parameter termed the "colorimetric response" (CR) (Eq. 1) (Charych, Nagy, Spevak, & Bednarskit, 1993).

$$CR(\%) = \left(\frac{\left({}^{A_{blue}}/_{A_{blue}+A_{red}} \right)_b - \left({}^{A_{blue}}/_{A_{blue}+A_{red}} \right)_a}{\left({}^{A_{blue}}/_{A_{blue}+A_{red}} \right)_b} \right) \times 100 \quad (1)$$

In Eq. 1, A is the absorbance of the blue (λ around 650 nm) and red components (λ around 540 nm), as determined by UV–Vis spectroscopy. The terms "blue" and "red" relate to the material appearance, and the indices "b" and "a" represent the absorbances before and after temperature exposure, respectively.

2.4. Colorimetric response in the presence of ENRO

To analyze the effect of ENRO on the PDA nanoblends, an ENRO solution (3.0 μM) was prepared in a TC/SDS solvent mixture of the same concentration to that used in the nanoblend. In this procedure, we aimed to prevent the dilution of the nanosensor suspension. Successive aliquots of ENRO solution were added to the nanoblend suspension until the final ENRO concentration of 2.0 μM was achieved. The mixtures were maintained at 30 °C over 60 min, and the spectra were obtained between 400 and

900 nm using a Lambda 35 UV-Vis spectrophotometer (Perkin Elmer Inc, Waltham, USA) at 30 °C. The CR of the nanoblend after ENRO addition was calculated using Eq. 1.

2.5. Kinetic experiments

The determination of the rate of colorimetric transition (R_{CT}) was performed over 60 min using four fixed ENRO concentrations (0.6, 1.0, 1.4, and 2.0 μM), at 30 °C. The R_{CT} was calculated by plotting the CR *versus* time and determining the slope in the linear region.

2.6. Fluorescence experiments

The same samples used to obtain the CR curves were analyzed with an LS55 fluorescence spectrophotometer (Perkin Elmer Inc, Waltham, USA) using quartz cells having a 1-cm path length. The fluorescence experiments were performed at 30 °C using an excitation wavelength (λ_{exc}) of 315 nm (at which ENRO is excited). The slit widths for both excitation and emission were fixed at 3.5 nm. The emission spectra were recorded in the 316–900 nm range.

2.7. Statistical analyses

All results were statistically analyzed. The best model to explain the effect of SDS and ENRO concentration on CR and R_{CT} was a complete second-order model, as shown in Eq. 2.

$$Y_1 = \beta_0 + \beta_1 X_{1i} + \beta_2 X_{2i} + \beta_{21} X_{1i}^2 + \beta_{22} X_{2i}^2 + \beta_{12} X_{1i} X_{2i} + e_i \quad (2)$$

In Eq. 2, Y_1 is the response variable, β_0 is the constant of the regression model, β_1 and β_2 are the first-order effects of the SDS and ENRO concentrations, respectively, β_{21} and β_{22} are the second-order effects of the SDS and ENRO concentrations, respectively, β_{12} is the interaction between SDS and ENRO, X_{1i} is the SDS concentration, X_{2i} is the ENRO concentration, and e_i is the experimental error NID $(0, \sigma^2)$.

The lack-of-fit, regression coefficients, and accuracy coefficients (SQREGRESSION/SQTREATMENTS) were evaluated. The analyses for adjusting the

proposed model were performed using SAS® (Statistical Analysis System – SAS, version 9.1, licensed for the Federal University of Viçosa).

The response surface methodology is an effective model with appropriate graphical representation for use when the response variable is influenced by several quantitative factors. Thus, the influence of the independent variables (SDS and ENRO concentration) on the response variables (CR and R_{CT}) were obtained by means of two response surfaces.

3. Results and discussion

3.1. Characterization of the PDA/TC/SDS nanoblends

Before applying the nanoblends as nanosensors to detect ENRO, their structures were characterized. PDA/TC nanostructures were formed by mixing two polymers to form spherical nanoaggregates with a D_h of 80.9 ± 4.1 nm and ζ-potential of −20.9 ± 1.2 mV. We have already suggested that the structure of nanoblends formed by PDA and TC consists of a hydrophobic core, which comprises the alkyl tail of PDA and the TC PO segments, surrounded by a hydrophilic shell formed by PDA carboxylic groups and TC EO segments (de Souza et al., 2016; Ferreira et al., 2018; Rezende et al., 2017). As the D_h for isolated TC molecules is around 4.0 nm, the size of nanoblends indicates that many PDA and TC molecules were aggregated. The negative ζ-potential points to the partial ionization of carboxylic groups of PDA that are located at the hydrophobic/hydrophilic interface of nanoblends. However, because the SDS molecules were also incorporated into the nanosensor, the nanoblend structure could be different.

The first difference between the PDA/L64 and PDA/L64/SDS nanoblends is related to the time needed for the diacetylene monomers to self-assemble into the correct structure to allow the polymerization reaction. We found that the time required for monomer organization increased with increasing SDS concentration, e.g., the times for the nanoblends to reach sufficient conditions for polymerization were 12, 24, 48, and 72 h for the PDA/L64/SDS nanostructures containing 0, 13, 17, and 21 mM SDS, respectively. The ζ-potential values were almost independent of the SDS concentration, whereas D_h increased as the amphiphilic concentration increased (Table S1). These results indicated that the surfactant molecules were entrapped in the sensor nanostructure, interacting with TC and PDA molecules.

The effect of SDS concentration on the magnitudes of ζ and D_h can be explained by considering the electrostatic repulsion between the carboxylic groups of the PDA

heads and the sulfate groups of the SDS molecules, which are both negatively charged and present at the hydrophobic/hydrophilic interface of nanoblends. Anionic surfactants, such as SDS, strongly interact with neutral polymers, such as L64 (Couderc-Azouani et al., 2005). Hence, we believe that SDS molecules have entered the nanoblend structure and formed domains between PDA chains, as well as between the PO segments of L64. Couderc-Azouani et al. (2005) studied the interaction between L64 and SDS molecules and found that the addition of SDS to L64 above the critical micellar concentration (CMC) leads to the formation of mixed L64/SDS nanoaggregates, which have an average radius of 2.0 nm (Couderc-Azouani et al., 2005). Therefore, our results indicate that PDA plays an important role in the nanostructure size, which is due to the aggregation of a significant number of these molecules (PDA, L64, and SDS).

To evaluate the effect of SDS on the optical properties of the nanoblends, we obtained the UV-vis spectra of the suspensions containing different SDS concentrations after polymerization under UV exposure for equal periods (30 s) (Fig. 1).

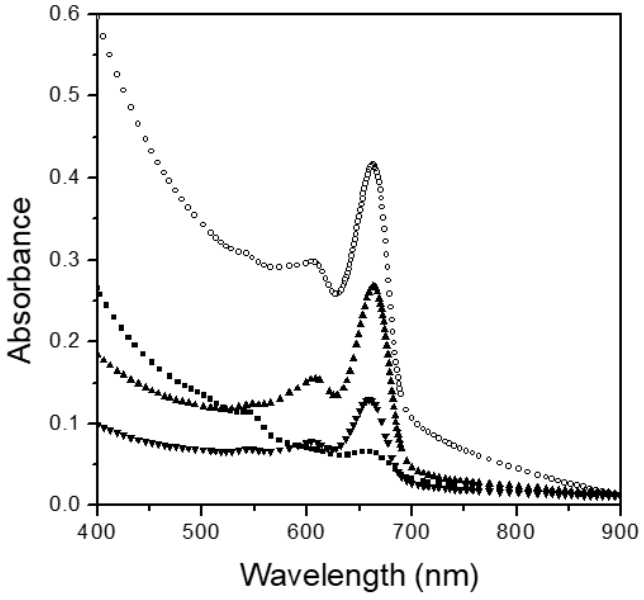

Fig. 1. Absorbance of the nanoblends formed of PDA (1 mM) and L64 1% (w/w) containing SDS concentrations of (■) 0, (○) 13, (▲) 17, and (▼) 21 mM at 25 °C and 30-s irradiation time.

All the nanosensor suspensions presented similar profile of electronic spectra, having a maximum absorption band at 640 nm and a shoulder at 590 nm. Clearly, the presence of SDS in the nanostructures enhanced the intensity of the electronic bands. In

the nanoblends containing 13 mM SDS, the intensity of the absorption bands increased significantly; however, above this concentration, these absorbances decreased. This means that there is an optimal SDS concentration that favors the packing of diacetylene molecules and increases the polymerization yield. The low polymerization yield at 17 and 21 mM SDS may be attributed to the increase in nanostructure size, which results in the diacetylene chains being further from each other, thus reducing the polymerization efficiency. Previously, we found that nanoblends synthesized with the addition of up to 3 mM cholesterol also presented better polymerization yields compared to the structure formed of PDA and L64 (Rezende et al., 2017).

To determine the effect of SDS on the rotational potential energetic barrier of the PDA, the temperature dependence of optical properties of nanostructures was investigated. The thermochromism profile of the nanosensor provides information about the rotational rigidity of the PDA chains. Fig. 2 shows the color transition of the PDA/L64/SDS nanoblends with different concentrations of SDS as a function of temperature.

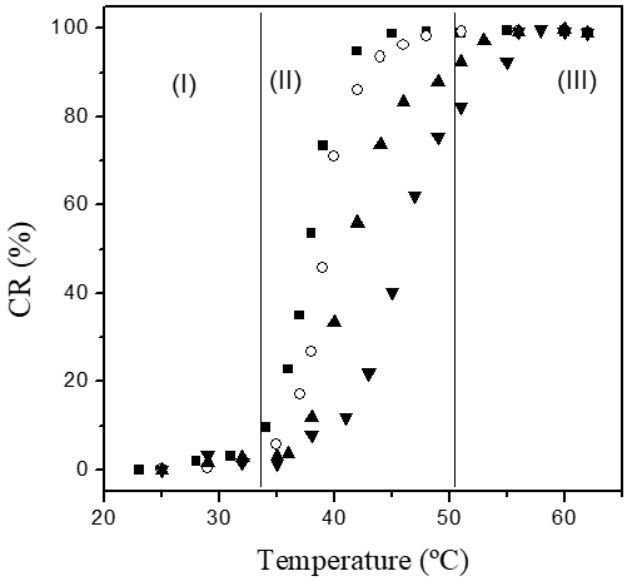

Fig. 2. Colorimetric response (CR, %) of the nanoblends formed of PDA (1 mM) and L64 1% (w/w) containing SDS concentrations of (■) 0, (○) 13, (▲) 17, and (▼) 21 mM as a function of temperature (°C).

All nanoblends presented the same sigmoidal CR profile with increasing temperature. We can divide the thermochromism graph into three regions: region I,

where the CR increased slightly with increasing temperature, region II, where there was an abrupt change in the CR in a small temperature range, indicating the existence of a thermodynamic cooperative process, and region III, where the CR was almost constant with increasing temperature. In region II, the temperature corresponding to the inflexion point of the curve is defined as the temperature of chromatic transition (T_{tr}) (Ferreira et al., 2018), and these values were higher with increasing SDS concentration in the nanoblend composition ($T_{tr\text{-}0\ mM}$= 38 °C, $T_{tr\text{-}13\ mM}$= 39 °C, $T_{tr\text{-}17\ mM}$= 42 °C, and $T_{tr\text{-}21\ mM}$= 47 °C). A well-accepted model to explain the color transition of PDA nanostructures is the rotation of the functional group around the carbon−carbon bond present in the PDA chains, which reduces the space for π-electron displacement and changes the electronic absorption. An energetic barrier must be overcome for this transition to occur (Carpick, Sasaki, Marcus, Eriksson, & Burns, 2004).

The T_{tr} value is related to the rotational energy barrier (ΔE_{RB}), following the relationship $n_{red}/n_{blue} \propto e^{-\Delta E_{RB}/KT}$, where n is the number of red and blue molecules, K is the Boltzmann constant, and T is the temperature. The system should be at T_{tr} for the molecules to have sufficient energy to transfer kinetic energy via molecular collisions for the PDA molecules to overcome the ΔE_{RB} (Krushev & Paul, 2002). Our results showed that, as the SDS concentration increased, the T_{tr} correspondingly increased, and, consequently, the ΔE_{RB} values increased, probably because of the formation of micro-domains of SDS that strongly interacted with the PDA chains (Rezende et al., 2017).

3.2. Polydiacetylene nanoblends as an optical nanosensor for enrofloxacin detection

Detecting ENRO by a simple methodology is an important approach for controlling antibiotic residues in food and, consequently, food safety. Hence, we explored the color transition ability of the PDA/TC/SDS nanoblends in the presence of a small amount of ENRO. Fig. 3 shows the CR profiles of the nanoblends with increasing ENRO concentrations at 30 °C.

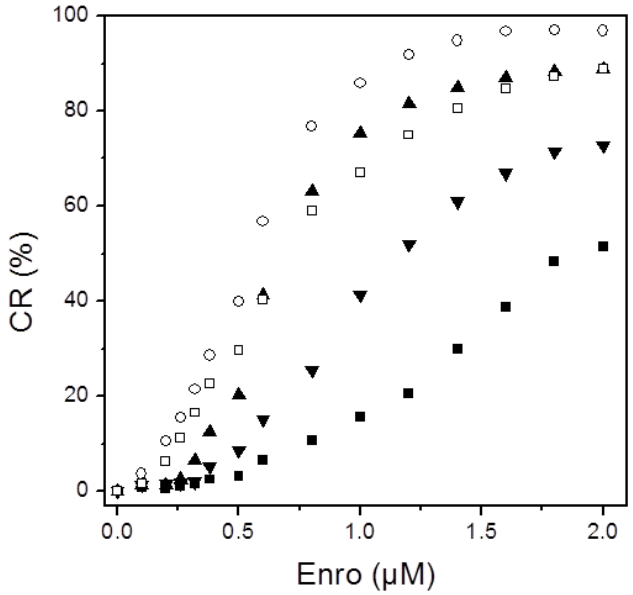

Fig. 3. Colorimetric response (CR, %) of the nanoblends formed of PDA (1mM) and L64 1% (w/w) and (■) 0, (○) 13, (▲) 17, and (▼) 21 mM SDS as a function of enrofloxacin concentration, at 30 °C.

Independent of the SDS concentration, higher ENRO concentrations led to higher CR values. However, the PDA/L64/SDS nanoblends showed superior CR values to those without the surfactant. The most sensitive nanoblend was that containing 13 mM SDS, followed by that containing 17 mM SDS, which achieved 92% and 74% CR, respectively, with 2.0 μM of ENRO. On the other hand, the nanoblend without SDS and that containing 21 mM SDS were less sensitive to the presence of ENRO, reaching CR values of only 28% and 40%, respectively (Fig. 3). The higher CR values for nanoblends containing 13 mM SDS can be explained by the balance between two energies; that is, i) the energy involved in the ENRO–SDS specific interaction (Seedher & Agarwal, 2009) and ii) the ΔE_{RB} of the PDA chains. Increasing the SDS concentration promotes interactions between ENRO and SDS but also increases ΔE_{RB}, as shown by the thermochromism results (Fig. 2). Hence, although there are fewer ENRO–SDS interactions in the presence of 13 mM SDS, this nanoblend showed a lower ΔE_{RB} than those containing 17 and 21 mM SDS.

To determine the role of ENRO partitioning from the bulk of the system to the hydrophobic core of nanoblends on the efficiency of the colorimetric transition of the nanosensors, we measured the fluorescence emission of ENRO (λ_{exc} = 315 nm and λ_{em} =

316–900 nm). Fig. S1 shows the fluorescence intensity of ENRO added to the nanoblend suspensions at the same concentrations used in the CR experiments.

The dependence of the ENRO fluorescence intensity on the ENRO concentration showed the same behavior for all nanoblends, independent of the SDS concentration present in the nanostructure at both temperatures. At low ENRO concentrations, the fluorescence intensity was a maximum, but, as the ENRO concentration increased, its fluorescence intensity decreased, demonstrating ENRO self-quenching, probably because of the ENRO transfer from the bulk to the interior of the nanoblend, which induced the formation of ENRO dimers.

The fluorescence data show that the amount of ENRO partitioned in the nanoblend interior is independent on the nanostructure composition (i.e., independent of the absence or presence SDS and the SDS concentration). However, because the PDA/L64/SDS CRs were higher than those of the PDA/L64 nanoblends, it is clear that the energy released from the ENRO–SDS interaction ($\Delta E_{\text{ENRO–SDS}}$) is the driving force for the PDA color change, resulting in the PDA conformational change. The Fig. S2 shows a schematic representation of the mechanistic basis of the nanoblend for detecting ENRO.

Because the SDS and ENRO concentrations are important factors influencing the colorimetric transition of the nanoblends, we modeled the significance of these factors on the CR of the nanoblends. Eq. 3 statistically model the effects of the SDS and ENRO concentrations on the CR. The complete second-order model was tested for lack-of-fit and parameter significance, and the coefficient of determination was greater than 98.7%. The model parameters that showed significance at the 5% probability level (t-test) were used to describe the CR mathematically. Hence, both the SDS and ENRO concentration influenced the CR ($p < 0.05$).

$$CR = -17.736 + 5.846[SDS] + 61.193[ENRO] - 0.291[SDS]^2 - 15.209[ENRO]^2 + 1.058[SDS][ENRO] \quad (3)$$

The quadratic effects of the SDS and ENRO concentrations and their interactions indicate that maximum CR was obtained at [ENRO] = 2.0 μM and [SDS] = 14.6 mM, as shown in Fig. S3. In the ENRO concentration curve, the concentration of SDS in the nanoblend that led to the highest CR was 9–14 mM, indicating that this surfactant concentration interval yielded the most efficient nanosensors.

Based on the CR results (Fig. 3), we calculated the limit of detection (LOD) for ENRO using the nanoblends (Rezende et al., 2017). The influence of the SDS concentration on the LOD was statistically modeled using Eq. 4. The second-order model was tested for lack-of-fit and parameter significance, and the coefficient of accuracy was higher than 99.9%. The first- and second-degree effect of the SDS concentration was significant, based on a 5% probability level (t-test).

$$LOD = 0.431 - 0.065[SDS] + 0.003[SDS]^2 \quad (4)$$

The quadratic effect of [SDS] indicates that the LOD decreased up to [SDS] = 11.6 mM (LOD=0.054 μM). This behavior is shown in Fig. S4. The European Union has set the maximum concentration limit of ENRO in milk as 100 μg mL^{-1}, which corresponds to 0.278 μM. Our results show that the nanoblends containing SDS were able to detect ENRO at levels almost five times less than this limit.

Other techniques for detecting ENRO in milk show different accuracy and sensitivity, e.g., liquid chromatography (LOD = 0.0001 μg mL^{-1} (Yao et al., 2015)), capillary electrophoresis (LOD = 0.0003 μg mL^{-1} (Lombardo-Agüí et al., 2010)) and enzyme-linked immunosorbent assays (LOD = 0.0002 μg mL^{-1} (Yu et al., 2018)). Although these techniques are more sensitive and accurate than the nanosensor developed by us, they usually require highly skilled personnel, use of hazardous reagents and/or expensive reagents or equipment, which makes them less practical for screening a large number of samples in a food industry. Thus, the nanoblend containing SDS can be considered low-cost and environment-friendly alternative technique with potential to detect ENRO in food matrices, e.g., milk and dairy products.

In addition, in previous works of our group, polydicetylenic nanoblends have demonstrated potential to be applied for detecting target molecules (de Souza et al., 2016) and changes in the food media, such as temperature (Ferreira et al., 2018). These findings are important for food preservation and quality. In addition, PDA/cholesterol nanoblends were successfully applied for detection of bovine serum albumin in milk (Rezende et al., 2017).

3.3. Kinetic rate of colorimetric transition of the nanoblends in the presence of ENRO

For a sensor to be considered suitable for food applications, in addition to its high sensitivity, it must also show fast responses to the analyte of interest. Bearing in

mind that both nanoblend composition (mainly SDS concentration) and ENRO played important roles on the CR of the nanoblends, we believe that these same parameters may influence the kinetics of the colorimetric transition of the nanosensors. Hence, the influence of the SDS and ENRO concentrations on the kinetic R_{CT} of nanoblends was statistically modeled using Eq. 5. We used a complete second-order model, which was tested for lack-of-fit and parameter significance using a 5% probability level (t-test). The coefficient of determination was greater than 99%. The plots of CR *versus* time that were used to obtain the kinetic R_{CT} are shown in Figs. S5a–d.

Linear and quadratic effects regarding the SDS concentration were observed, but only a linear influence of the ENRO concentration on the R_{CT} of the nanoblends was verified. The SDS and ENRO concentrations that resulted in the highest R_{CT} were 9.1 and 2.0 µM, respectively (R_{CT}= 4.0 % CR min^{-1}), as shown in Fig. 4.

$$RATE = -0.434 + 0.477[SDS] + 1.088[ENRO] - 0.025[SDS]^2 \quad (5)$$

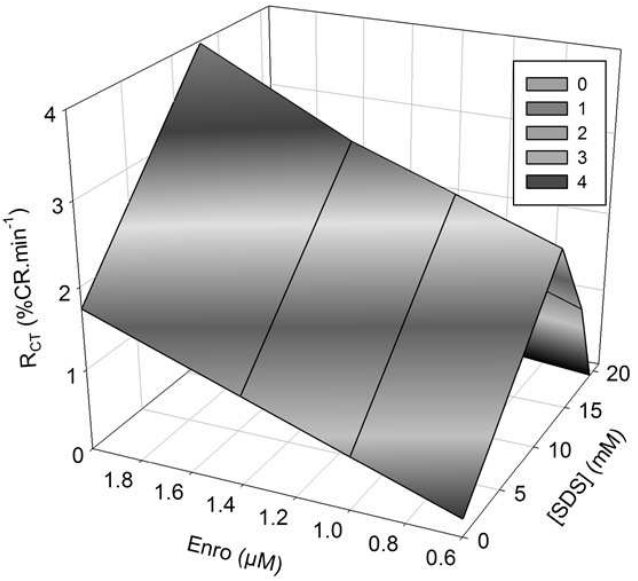

Fig. 4 – Response surface for the optimization of the rate of colorimetric transition of the nanoblends as a function of SDS and ENRO concentration (millimoles and micromoles, respectively), at 30 °C.

Applying the data obtained for the LOD (Eq. 4) to the response surface (Eq. 5), it was possible to determine that R_{CT} value for the LOD was 1.79% CR min^{-1}. Considering that 40% CR is easily visible to the naked eye for the identification of the

color change of PDA nanosensors (Gou et al., 2010; Pimsen, Khumsri, Wacharasindhu, Tumcharern, & Sukwattanasinitt, 2014; Pires et al., 2011), the transition takes only 22 min to achieve this value, which can be considered a rapid response.

Probably, the higher kinetic R_{CT} of the nanoblends containing SDS in the range between 9 and 13 mM is related to the higher speed at which ENRO molecules enter these nanoblends compared with nanostructures with other SDS concentrations. An experiment was performed to confirm this hypothesis: the ratio of fluorescence decay (F/F_0) as a function of time was plotted, where F is the fluorescence intensity at time t and F_0 is the fluorescence intensity at t_0 (Fig. S6).

The F/F_0 reduced with increasing time for all nanoblends, but the nanoblends containing 13 mM SDS showed a larger slope in the F/F_0 *versus* time curve, which indicates that ENRO molecules were partitioned faster to this nanoblend than to the others. Hence, this superior partitioning speed explains the higher kinetic R_{CT} of nanoblends in this range of surfactant concentration (9–13 mM of SDS).

3.4. Investigation of the role of the chemical structure of TC on the nanosensor properties

There is a great variety of TCs, all having different chemical structures. In addition, the nanoblends can be easily modulated by changing the composition and chemical nature of the constituents; thus, we replaced the L64 by F68 in the nanoblends containing 13 mM SDS. Both L64 and F68 have almost the same size of the hydrophobic part (i.e., the number of PO units are 31 and 30 for L64 and F68, respectively), but the former has an number of EO units (hydrophilic part) around 6 times smaller than the latter ($n_{EO\text{-}L64}$= 26 units and $n_{EO\text{-}F68}$= 152 units); consequently, F68 is more hydrophilic than L64 (de Souza et al., 2016).

Regarding the polymerization, it is interesting to observe that the PDA/F68/SDS nanoblends presented a very different behavior from that of PDA/L64/SDS at the same surfactant concentration. The time required for mixing before PDA/F68/SDS polymerization was 72 h, whereas only 24 h was required when L64 was used. These differences also resulted in a smaller polymerization yield for the PDA/F68/SDS than for the PDA/L64/SDS nanoblends (Fig. S7). This behavior is probably due to the larger size of the nanostructures formed with F68 (982.2 ± 23.3 nm) compared to those formed with L64 (234.2 ± 3.5 nm), which increased the distance between the diacetylene

monomers, thus reducing the efficiency of polymerization and decreasing the blue intensity of these nanoblends.

The ζ-potential values of the nanoblends were very different. For nanoblends containing the TC L64, the ζ-potential values were much more negative (about -40 mV) than that containing F68, whose ζ-potential value was -18.1 ± 1.1 mV. Considering that the ζ-potential value of the nanoblend without SDS was -20.9 ± 1.2 mV, these results indicate that the densities of charge of the PDA/L64 and PDA/F68/ (13 mM SDS) nanoblends were similar.

Concerning the thermochromism, the PDA/F68/SDS nanoblends showed $T_{tr} = 42$ °C. This result demonstrates that the interactions between PDA–PDA, PDA–TC, and PDA–SDS in the presence of F68 were different of those occurring in the presence of L64, resulting in a higher ΔE_{RB} for the nanoblends formed with the more hydrophilic TC.

In the presence of ENRO, PDA/F68/SDS showed similar behavior to PDA/L64/SDS at the same surfactant concentration (Fig. 5a), showing LOD of 0.071 μM. However, regarding the R_{CT}, the nanoblends containing F68 demonstrated slower rate than those with L64 and 13 mM SDS (Fig. 5b). This result is probably because of the higher diffusion time of ENRO through the hydrophilic shell and hydrophobic core of nanoblends formed with F68 compared with those formed with L64.

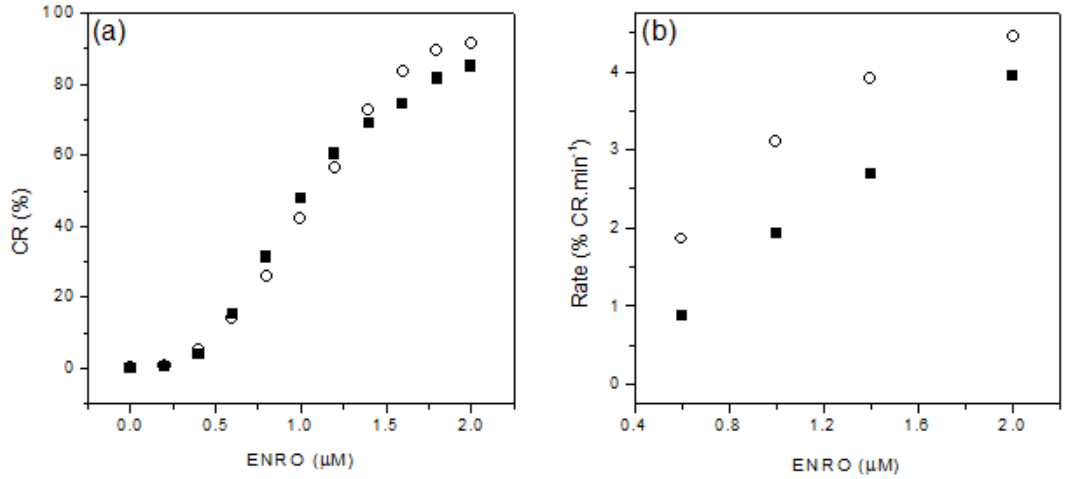

Fig. 5 – (a) Colorimetric response (CR, %) of the nanoblends and (b) rate (% CR min^{-1}) of colorimetric transition as a function of ENRO concentration of nanoblends: (■) PDA/F68/SDS and (○) PDA/L64/SDS, both nanoblends contain 13 mM SDS, at 30 °C.

It is important to emphasize that, regarding the CR values which represent equilibrium properties, PDA/F68/(13 mM SDS) and PDA/L64/(13 mM SDS) showed similar behaviors. However, when the kinetic parameters are considered, the nanoblend formed with L64 showed faster responses than that formed with F68. This is an important finding because an efficient sensor should combine high sensitivity with rapid response times.

4. Conclusions

PDA/TC/SDS nanosensors detected ENRO with a LOD of 0.054 μM at 30 °C, which is around five times smaller than the maximum limit allowed by the European Union. The nanosensor efficiency was dependent on the nanoblend composition, and the optimal SDS concentration was around 9–14 mM.

The detection mechanism of the nanosensor is the direct interaction between ENRO and SDS, which releases enough energy to overcome the PDA ΔE_{RB}. For the ENRO–SDS interaction to occur, the diffusion of ENRO from the bulk system to the nanosensor hydrophobic core is necessary, and we have shown that the kinetics of this ENRO transfer was independent of the nanoblend chemical composition.

The response surface showed that both the concentration of ENRO and that of SDS influenced the R_{CT}, and the nanoblends with surfactant concentrations of 9 and 13 mM are rapid nanosensors.

The replacement of L64 for F68 changed the nanostructure of the sensor, especially its size, which directly impacted the R_{CT}. Hence, although the equilibrium CR behaviors of PDA/L64/SDS and PDA/F68/SDS were similar, the kinetic results were very different because of the slower diffusion of ENRO through the larger shell and core of the F68 macromolecules compared to those of L64.

Considering future applications of the nanoblends developed and chemically characterized in our work, the nanoblend containing 11.6 mM of SDS at 30 °C requires only 22 min to reach 40% CR, which is easily visible to the naked eye. Therefore, our results show that these nanoblends are promising for the cheap and easy preparation of nanosensors for the detection of antibiotic residues in different food matrices. Our results showed a strong specificity of the nanoblends for detecting enrofloxacin. However, some sources of limitations may reduce the efficiency of detection. For example, food samples containing molecules absorbing in blue ou red region and/or

turbid samples should be cleaned-up by centrifugation, liquid-liquid extration, filtration or precipitation before the detection analysis.

Declarations of interest

All the authors declare no conflict of interest.

Acknowledgments

The authors wish to thank the Coordenação de Aperfeiçoamento de Pessoal de Nível Superior (CAPES), Conselho Nacional de Desenvolvimento Científico e Tecnológico (CNPq), and Fundação de Apoio à Pesquisa de Minas Gerais (FAPEMIG) for their financial support.

References

Carpick, R. W., Sasaki, D. Y., Marcus, M. S., Eriksson, M. a, & Burns, A. R. (2004). Polydiacetylene Films: a Review of Recent Investigations into Chromogenic Transitions and Nanomechanical Properties. *Journal of Physics: Condensed Matter*, *16*(23), 679–697. https://doi.org/10.1088/0953-8984/16/23/R01

Chanakul, A., Traiphol, N., Faisadcha, K., & Traiphol, R. (2014). Dual colorimetric response of polydiacetylene/Zinc oxide nanocomposites to low and high pH. *Journal of Colloid and Interface Science*, *418*, 43–51. https://doi.org/10.1016/j.jcis.2013.11.083

Charych, D. H., Nagy, J., Spevak, W., & Bednarskit, M. D. (1993). Direct Colorimetric Detection of a Receptor-Ligand Interaction by a Polymerized Bilayer Assembly Author (s): Deborah H . Charych , Jon O . Nagy , Wayne Spevak and Mark D . Bednarski Published by : American Association for the Advancement of Science Stab. *Science*, *261*(5121), 585–588.

Chen, G., & Li, Q. (2013). Luminescence Screening of Enrofloxacin and Ciprofloxacin Residues in Swine Liver after Dispersive Liquid–Liquid Microextraction Cleanup. *Journal of Agricultural and Food Chemistry*, *61*(1), 98–102. https://doi.org/10.1021/jf3042038

Chen, J., Xu, F., Jiang, H., Hou, Y., Rao, Q., Guo, P., & Ding, S. (2009). A novel quantum dot-based fluoroimmunoassay method for detection of Enrofloxacin residue

in chicken muscle tissue. *Food Chemistry*, *113*(4), 1197–1201. https://doi.org/10.1016/j.foodchem.2008.08.006

Choi, J.-H., Mamun, M. I. R., Abd El-Aty, A. M., Park, J.-H., Shin, E.-H., Yeon Park, J., … Shim, J.-H. (2011). Development of a single-step precipitation cleanup method for the determination of enrofloxacin, ciprofloxacin, and danofloxacin in porcine plasma. *Food Chemistry*, *127*(4), 1878–1883. https://doi.org/10.1016/j.foodchem.2011.02.027

Couderc-Azouani, S., Sidhu, J., Thurn, T., Xu, R., Bloor, D. M., Penfold, J., … Wyn-Jones, E. (2005). Binding of Sodium Dodecyl Sulfate and Hexaethylene Glycol Mono- n -Dodecyl Ether to the Block Copolymer L64: Electromotive Force, Microcalorimetry, Surface Tension, and Small Angle Neutron Scattering Investigations of Mixed Micelles and Polymer/Micellar S. *Langmuir*, *21*(22), 10197–10208. https://doi.org/10.1021/la047312q

de Souza, L. C., Rezende, J. de P., Pires, A. C. dos S., da Silva, L. H. M., da Silva, M. do C. H., Castrillon, E. D. C., & de Andrade, N. J. (2016). Polydiacetylene/triblock copolymer nanoblend applied as a sensor for micellar casein: A thermodynamic approach. *Food Chemistry*, *197*, 841–847. https://doi.org/10.1016/j.foodchem.2015.11.071

Ferreira, G. M. D., Ferreira, G. M. D., Hespanhol, M. do C., Rezende, J. de P., Pires, A. C. dos S., Ortega, P. F. R., & da Silva, L. H. M. (2018). A simple and inexpensive thermal optic nanosensor formed by triblock copolymer and polydiacetylene mixture. *Food Chemistry*, *241*, 358–363. https://doi.org/10.1016/j.foodchem.2017.08.115

García-Espejo, G., Pérez-Morales, M., Goldmann, M., Martín-Romero, M. T., Giner-Casares, J. J., & Camacho, L. (2017). Organization and structure of mixed Langmuir films composed of polydiacetylene and hemicyanine. *Journal of Colloid and Interface Science*, *508*, 583–590. https://doi.org/10.1016/j.jcis.2017.08.069

Gou, M., Guo, G., Zhang, J., Men, K., Song, J., Luo, F., … Wei, Y. (2010). Time–temperature chromatic sensor based on polydiacetylene (PDA) vesicle and amphiphilic copolymer. *Sensors and Actuators B: Chemical*, *150*(1), 406–411. https://doi.org/10.1016/j.snb.2010.06.041

Huet, A.-C., Charlier, C., Tittlemier, S. A., Singh, G., Benrejeb, S., & Delahaut, P. (2006). Simultaneous Determination of (Fluoro)quinolone Antibiotics in Kidney,

Marine Products, Eggs, and Muscle by Enzyme-Linked Immunosorbent Assay (ELISA). *Journal of Agricultural and Food Chemistry*, *54*(8), 2822–2827. https://doi.org/10.1021/jf052445i

Jiang, L., Luo, J., Dong, W., Wang, C., Jin, W., Xia, Y., … He, H. (2015). Development and evaluation of a polydiacetylene based biosensor for the detection of H5 influenza virus. *Journal of Virological Methods*, *219*, 38–45. https://doi.org/10.1016/j.jviromet.2015.03.013

Krushev, S., & Paul, W. (2002). The Role of Internal Rotational Barriers in Polymer Melt Chain Dynamics. *Macromolecules*, *35*, 4198–4203.

Lombardo-Agüí, M., García-Campaña, A. M., Cruces-Blanco, C., & Gámiz-Gracia, L. (2015). Determination of quinolones in fish by ultra-high performance liquid chromatography with fluorescence detection using QuEChERS as sample treatment. *Food Control*, *50*, 864–868. https://doi.org/10.1016/j.foodcont.2014.10.027

Lombardo-Agüí, M., García-Campaña, A. M., Gámiz-Gracia, L., & Cruces Blanco, C. (2010). Laser induced fluorescence coupled to capillary electrophoresis for the determination of fluoroquinolones in foods of animal origin using molecularly imprinted polymers. *Journal of Chromatography A*, *1217*(15), 2237–2242. https://doi.org/10.1016/j.chroma.2010.02.016

Pattanatornchai, T., Charoenthai, N., Wacharasindhu, S., Sukwattanasinitt, M., & Traiphol, R. (2013). Control over the color transition behavior of polydiacetylene vesicles using different alcohols. *Journal of Colloid and Interface Science*, *391*, 45–53. https://doi.org/10.1016/j.jcis.2012.10.004

Pimsen, R., Khumsri, A., Wacharasindhu, S., Tumcharern, G., & Sukwattanasinitt, M. (2014). Colorimetric detection of dichlorvos using polydiacetylene vesicles with acetylcholinesterase and cationic surfactants. *Biosensors and Bioelectronics*, *62*, 8–12. https://doi.org/10.1016/j.bios.2014.05.069

Pires, A. C. dos S., Soares, N. de F. F., da Silva, L. H. M., da Silva, M. do C. H., De Almeida, M. V., Le Hyaric, M., … Reis, S. G. (2011). A colorimetric biosensor for the detection of foodborne bacteria. *Sensors and Actuators B: Chemical*, *153*(1), 17–23. https://doi.org/10.1016/j.snb.2010.09.069

Pires, A. C. S., Soares, N. de F. F., da Silva, L. H. M., da Silva, M. C. H., Mageste, A. B., Soares, R. F., … Andrade, N. J. (2010). Thermodynamic Study of Colorimetric

Transitions in Polydiacetylene Vesicles Induced by the Solvent Effect. *The Journal of Physical Chemistry B*, *114*(42), 13365–13371. https://doi.org/10.1021/jp105604t

Rezende, J. de P., Ferreira, G. M. D., Ferreira, G. M. D., da Silva, L. H. M., do Carmo Hepanhol da Silva, M., Pinto, M. S., & Pires, A. C. dos S. (2017). Polydiacetylene/triblock copolymer nanosensor for the detection of native and free bovine serum albumin. *Materials Science and Engineering: C*, *70*, 535–543. https://doi.org/10.1016/j.msec.2016.09.009

Seedher, N., & Agarwal, P. (2009). Various Solvent Systems for Solubility Enhancement of Enrofloxacin. *Indian Journal of Pharmaceutical Sciences*, *71*(1), 82–87. https://doi.org/10.4103/0250-474X.51958

Shi, Q., Huang, J., Sun, Y., Yin, M., Hu, M., Hu, X., … Zhang, G. (2018). Utilization of a lateral flow colloidal gold immunoassay strip based on surface-enhanced Raman spectroscopy for ultrasensitive detection of antibiotics in milk. *Spectrochimica Acta - Part A: Molecular and Biomolecular Spectroscopy*, *197*, 107–113. https://doi.org/10.1016/j.saa.2017.11.045

Shin, Y. J., Shin, M. J., & Shin, J. S. (2017). Permeation-induced chromatic change of a polydiacetylene vesicle with nonionic surfactant. *Colloids and Surfaces A: Physicochemical and Engineering Aspects*, *520*, 459–466. https://doi.org/10.1016/j.colsurfa.2017.02.014

Terrado-Campos, D., Tayeb-Cherif, K., Peris-Vicente, J., Carda-Broch, S., & Esteve-Romero, J. (2017). Determination of oxolinic acid, danofloxacin, ciprofloxacin, and enrofloxacin in porcine and bovine meat by micellar liquid chromatography with fluorescence detection. *Food Chemistry*, *221*, 1277–1284. https://doi.org/10.1016/j.foodchem.2016.11.029

Tian, H., Wang, J., Zhang, Y., Li, S., Jiang, J., Tao, D., & Zheng, N. (2016). Quantitative multiresidue analysis of antibiotics in milk and milk powder by ultra-performance liquid chromatography coupled to tandem quadrupole mass spectrometry. *Journal of Chromatography B: Analytical Technologies in the Biomedical and Life Sciences*, *1033-1034*, 172–179. https://doi.org/10.1016/j.jchromb.2016.08.023

Xu, X., Liu, L., Jia, Z., & Shu, Y. (2015). Determination of enrofloxacin and ciprofloxacin in foods of animal origin by capillary electrophoresis with field

amplified sample stacking–sweeping technique. *Food Chemistry*, *176*, 219–225. https://doi.org/10.1016/j.foodchem.2014.12.054

Yao, K., Zhang, W., Yang, L., Gong, J., Li, L., Jin, T., & Li, C. (2015). Determination of 11 quinolones in bovine milk using immunoaffinity stir bar sorptive microextraction and liquid chromatography with fluorescence detection. *Journal of Chromatography B*, *1003*, 67–73. https://doi.org/10.1016/j.jchromb.2015.09.008

Yu, X., Zhang, X., Wang, Z., Jiang, H., Lv, Z., Shen, J., … Wen, K. (2018). Universal simultaneous multiplex ELISA of small molecules in milk based on dual luciferases. *Analytica Chimica Acta*, *1001*, 125–133. https://doi.org/10.1016/j.aca.2017.11.038

Zhang, H., Jiang, J., Wang, Z., Chang, X., Liu, X., Wang, S., … Chen, J. (2011). Development of an indirect competitive ELISA for simultaneous detection of enrofloxacin and ciprofloxacin. *Journal of Zhejiang University SCIENCE B*, *12*(11), 884–891. https://doi.org/10.1631/jzus.B1100076

Zhang, Y., Bromberg, L., Lin, Z., Brown, P., Van Voorhis, T., & Hatton, T. A. (2018). Polydiacetylene functionalized with charged termini for device-free colorimetric detection of malathion. *Journal of Colloid and Interface Science*, *528*, 27–35. https://doi.org/10.1016/j.jcis.2018.04.098

Zhang, Y., Northcutt, J., Hanks, T., Miller, I., Pennington, B., Jelinek, R., … Dawson, P. (2017). Polydiacetylene sensor interaction with food sanitizers and surfactants. *Food Chemistry*, *221*, 515–520. https://doi.org/10.1016/j.foodchem.2016.09.168

Zhou, J., Nie, W., Chen, Y., Yang, C., Gong, L., Zhang, C., … Feng, X. (2018). Quadruplex gold immunochromatogaraphic assay for four families of antibiotic residues in milk. *Food Chemistry*, *256*(November 2017), 304–310. https://doi.org/10.1016/j.foodchem.2018.02.002

SUPPLEMENTARY MATERIALS

Table S1 – Hydrodynamic diameter (D_h) and zeta potential (ζ) variations of PDA/L64 1.0% (w/w) nanoblends, containing 0, 13, 17, and 21 mM SDS. Time required for PDA/L64 or PDA/L64/SDS mixing without polymerization (●), and minimum time required for the UV polymerization of the mixture (●), at 25 °C.

[SDS]		Time between sonication and polymerization				
		0 h	12 h	24 h	48 h	72 h
0 mM	D_h (nm)	62.7 ± 3.1	80.9 ± 4.1			
	ζ (mV)	-19.0 ± 0.9	-20.9 ± 1.2			
	Color of mixture	●	●			
13 mM	D_h (nm)	470.5 ± 6.7	285.9 ± 3.9	234.2 ± 3.5		
	ζ (mV)	-40.5 ± 2.3	-42.2 ± 2.6	-41.6 ± 2.8		
	Color of mixture	●	●	●		
17 mM	D_h (nm)	751.6 ± 12.5	744.1 ± 13.5	794.1 ± 16.4	772.3 ± 15.6	
	ζ (mV)	-42.2 ± 2.0	-43.7 ± 3.0	-43.3 ± 2.2	-42.3 ± 2.5	
	Color of mixture	●	●	●	●	
21 mM	D_h (nm)	255.3 ± 12.3	974.7 ± 18.4	498.3 ± 14.2	618.6 ± 23.1	801.6 ± 17.8
	ζ (mV)	-58.6 ± 3.9	-48.4 ± 3.6	-45.9 ± 3.3	-45.6 ± 2.8	-42.7 ± 2.7
	Color of mixture	●	●	●	●	●

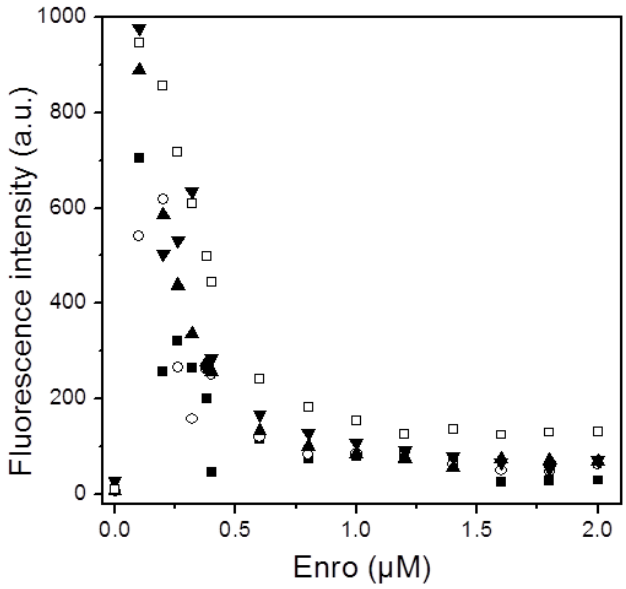

Fig. S1. Fluorescence intensity of ENRO as a function of its concentration in the nanoblends formed of PDA (1mM) + L64 1% (w/w) + SDS at (■) 0, (○) 13, (▲) 17, and (▼) 21 mM, at 30 °C.

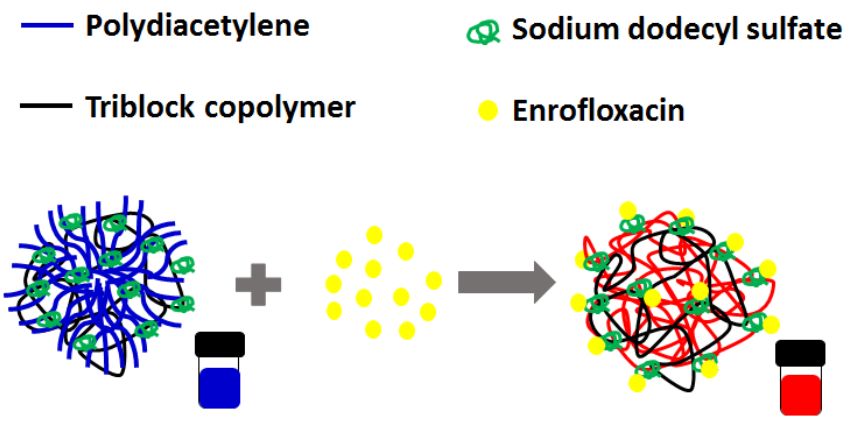

Fig. S2 – Schematic representation of enrofloxacin recognition by PDA/triblock copolymer/SDS nanoblend.

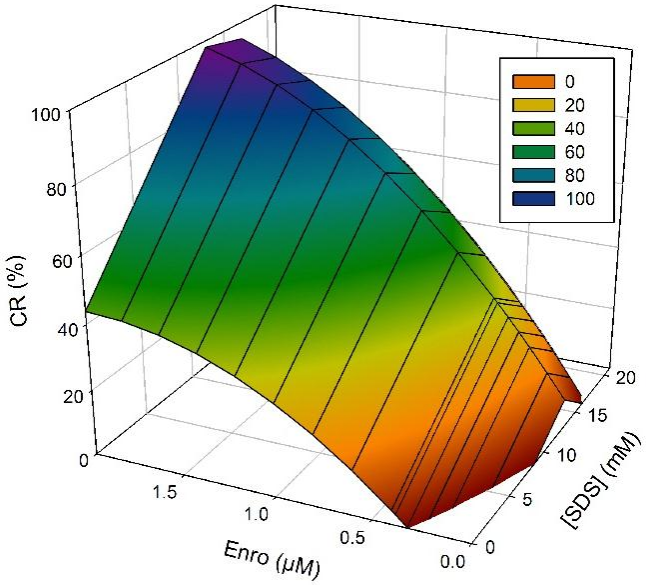

Fig. S3 - Response surface for the optimization of the CR of PDA/L64/SDS nanoblends as a function of SDS and ENRO concentrations (millimoles and micromoles, respectively), at 30 °C.

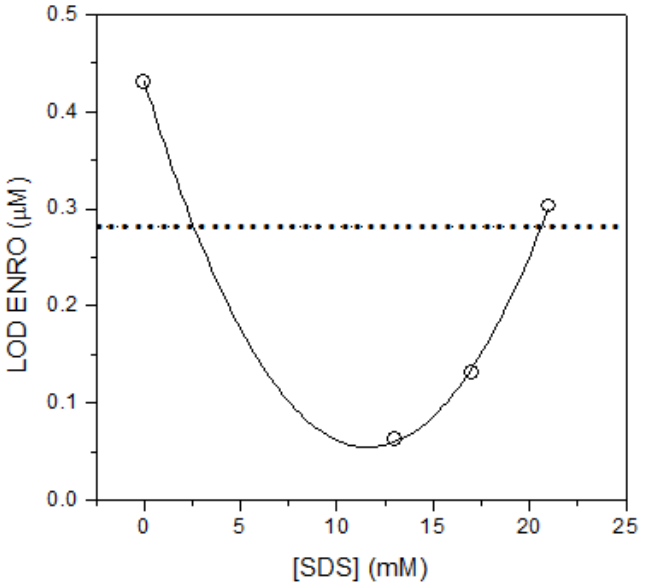

Fig. S4 – Limit of detection (LOD) (○) of enrofloxacin (ENRO) of PDA/L64/SDS nanoblends as a function of SDS concentration, at 30 °C. The dotted line represents the maximum concentration limit for ENRO in milk, as stipulated by the European Union.

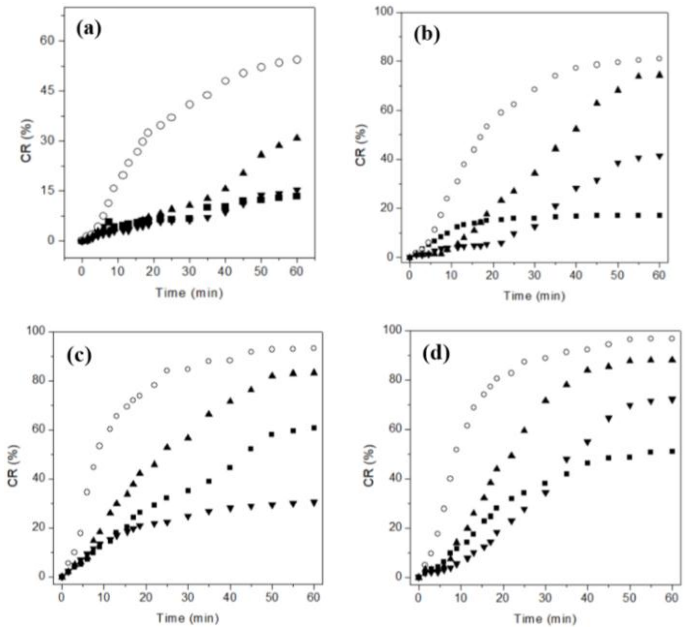

Fig. S5 – Plots of CR (%) *versus* time (min) for nanoblends formed of PDA (1 mM) and L64 1% (w/w) at (■) 0, (○) 13, (▲) 17, and (▼) 21 mM SDS as a function of ENRO concentration: (a) 0.6 µM of ENRO; (b) 1.0 µM of ENRO; (c) 1.4 µM of ENRO; and (d) 2.0 µM of ENRO, at 30 °C.

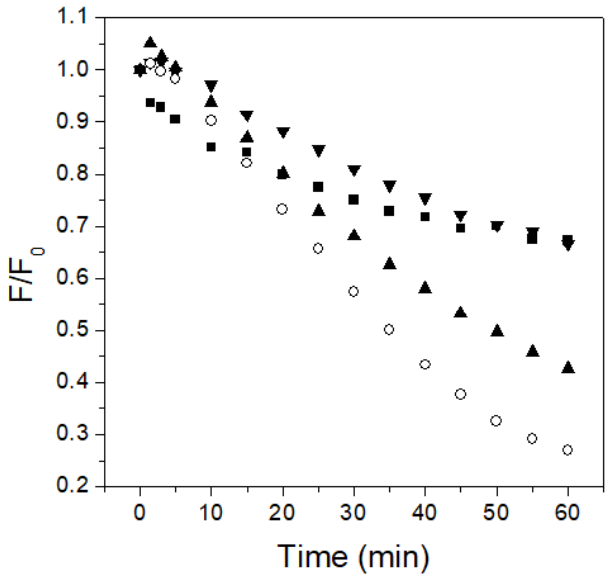

Fig. S6 – F/F_0 of ENRO (2.0 µM) added to nanoblends formed of PDA (1mM) + L64 1% (w/w) + SDS at (■) 0, (○) 13, (▲) 17, and (▼) 21 mM, at 30 °C.

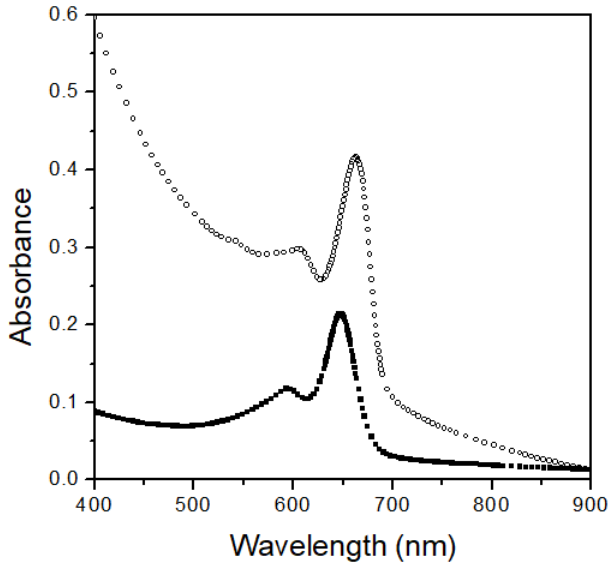

Fig. S7. Absorbance of the nanoblends formed of (○) PDA (1 mM) + L64 1% (w/w) + 13 mM SDS and the nanoblend formed of (■) PDA (1 mM) + F68 1% (w/w) + 13 mM SDS, at 25 °C.

ARTICLE 2

Thermodynamic and Kinetic Study of Epigallocatechin-3-Gallate-Bovine Lactoferrin Complex Formation Determined by Surface Plasmon Resonance (SPR): A Comparative Study with Fluorescence Spectroscopy

Article published in the journal *Food Hydrocolloids*.
doi:10.1016/j.foodhyd.2019.04.065

Abstract

The complexation between protein and polyphenol affects their biological functions. A complete understanding of such interactions requires comprehensive thermodynamic and kinetic characterizations. Surface plasmon resonance (SPR) and fluorescence spectroscopy (FS) described similarly the thermodynamic of interaction between bovine lactoferrin (bLF) and epigallocatechin-3-gallate (EGCG). The formation of the bLF-EGCG complex is spontaneous ($\Delta G^o_{SPR} \approx$ -29.00 kJ mol^{-1}, $\Delta G^o_{FS} \approx$ -26.00 kJ mol^{-1}) and entropically driven (ΔH^o_{SPR} = 14.26, ΔH^o_{FS} = 10.20 kJ mol^{-1} and $T\Delta S^o_{SPR} \approx$ 43.00, $T\Delta S^o_{FS} \approx$ 36.00 kJ mol^{-1}). The kinetic parameters obtained by SPR showed that the reaction occurs through an activated complex, whose energetic formation parameters from the association of free molecules ($E_{act\,(a)}$ = 49.5 kJ mol^{-1}, $\Delta H^{\ddagger}_a$ = 47.0 kJ mol^{-1}, and $T\Delta S^{\ddagger}_a$= -2.10 kJ mol^{-1}) were higher than those in the opposite direction (namely the dissociation of the stable complex, $E_{act\,(d)}$ = 17.4 kJ mol^{-1}, $\Delta H^{\ddagger}_d$ = 32.8 kJ mol^{-1}, and $T\Delta S^{\ddagger}_d$ = -45.10 kJ mol^{-1}), except for $\Delta G^{\ddagger}$ ($\Delta G^{\ddagger}_a$ = 49.1 kJ mol^{-1} and $\Delta G^{\ddagger}_d$ = 77.9 kJ mol^{-1}). This study provides useful information for optimizing the use of bLF–EGCG complex as a bioactive compound in different systems, such as medical, food, cosmetic, and pharmaceutical formulations.

Keywords: rate constants; activated complex; entropy increasing.

1. Introduction

Proteins are important biomacromolecules that function through binding to other molecules (Du et al., 2016). They could be applied in delivery systems in food or medical formulations for drugs or bioactive molecules, because they bind with small molecules via noncovalent interactions to form specific complexes that are biocompatible and stable (Shapira, Assaraf, & Livney, 2010). Milk proteins are promising for such nanovehicles, since their mainly hydrophobic structure allows them to act as natural vehicles for bioactive molecules that usually are also hydrophobic (Leilabadi-Asl, Divsalar, Saboury, & Parivar, 2018). Furthermore, milk proteins are inexpensive, widely available, generally recognized as safe (GRAS), and show excellent nutritional value and sensory properties (Głąb & Boratyński, 2017).

Bovine lactoferrin (bLF) is a globular milk glycoprotein of approximately 700 amino acid residues with a molecular weight of about 80 kDa. Its relatively high isoelectric point (pI ≈ 8.5) indicates that it is positively charged over a wide pH range, including neutral pH (Li, Li, Luo, Wang, & Zheng, 2017; Yang, Liu, Xu, Yuan, & Gao, 2014). In addition to being an iron carrier, bLF exerts several important biological activities, such as antimicrobial, antioxidant, anticarcinogenic, and anti-inflammatory ones (Liu, Wang, Ma, & Gao, 2016; Scala et al., 2017; Siqueiros-Cendón et al., 2014). However, only a few studies have examined the interaction between bLF and bioactive molecules (Bourbon, Cerqueira, & Vicente, 2016; Chaharband et al., 2018).

The polyphenol epigallocatechin-3-gallate (EGCG) (Fig. S1, Supporting Information) is the major bioactive catechin in green tea, exhibiting many biological activities, such as antiviral (including that against Zika virus) (Sharma, Murali, Singh, & Giri, 2017), neuroprotective (against Alzheimer (Walker et al., 2015) and Parkinson (Xu, Langley, Kanthasamy, & Reddy, 2017) diseases), and anticancer activities (Abd El-Rahman, Shehab, & Nashaat, 2017). EGCG also contributes to the prevention of cardiovascular diseases and the regulation of endocrine and immune systems (Chung et al., 2014; Yang, Wang, Lu, & Picinich, 2009). Previous studies reported the beneficial effect of protein-EGCG binding on the polyphenol activities, such as the increase in its antioxidant activity and bioavailability (Zagury, Kazir, & Livney, 2019) and antitumor efficacy (Wu et al., 2017).

To optimize the use of protein-EGCG complexes in different systems, it is important to study the kinetic and thermodynamic properties of these complexes

formation. Several researchers have reported the thermodynamic parameters of complex formation between EGCG and proteins, and all of them used fluorescence spectroscopy (FS) and isothermal titration calorimetry (ITC) techniques. Poncet-Legrand et al., (2007) showed that EGCG formed a complex with proline-rich protein with a binding constant (K_b) of approximately 10^5 L mol^{-1}, and standard enthalpy change (ΔH^0) and standard entropy change ($T\Delta S^0$) of -25.1 and -0.9 kJ mol^{-1}, respectively. The same kind of enthalpy-driven complexation was seen for EGCG interacting with porcine gastric mucin (Zhao, Chen, Yakubov, Aminiafshar, & Han, 2012), insulin (Wang, Liu, Dong, & Sun, 2012), fragments of amyloid β-peptide (Wang, Dong, & Sun, 2012), and lipase (X. Wu et al., 2013). On the other hand, Wang et al., (2012) found the formation of the EGCG-amyloid β-peptide complex to be an entropy-driven process (ΔH^0 = 2.09 and $T\Delta S^0$ = 35.12 kJ mol^{-1}). To the best of our knowledge, only one work by Yang et al., (2014) examined the thermodynamics of complex formation between EGCG and bLF, using FS and ITC techniques at 25 °C and pH 6.0. The K_b value was determined to be in the order of 10^5 L mol^{-1}, and the complex formation was also enthalpically favored and entropically unfavored.

However, the kinetics of protein-EGCG complex formation especially for the bLF-EGCG system has not been explored. The kinetic parameters for complexation provide detailed information about the underlying molecular dynamics. Such information could be obtained by surface plasmon resonance (SPR), which has an advantage over other techniques by allowing real-time measurements and being label-free. Meanwhile, the other study on the thermodynamics of bLF-EGCG complex formation was based on FS and ITC. Therefore, in this study we used SPR to determine the interaction between bLF and EGCG at physiological pH. Specifically, we report the thermodynamic parameters (K_b, ΔH^0, $T\Delta S^0$, ΔG^0, and complex stoichiometry) and the kinetic parameters [association and dissociation rate constants, activation energy (E_{act}), activation enthalpy change ($\Delta H^{\ddagger}$), activation entropy change ($T\Delta S^{\ddagger}$), and activation Gibbs free energy change ($\Delta G^{\ddagger}$)]. To support the SPR data, we also used fluorescence spectroscopy to compare with the thermodynamic results obtained by SPR.

2. Materials and methods

2.1. Materials

(-)-EGCG (95%) and bLF (85%) were purchased from Sigma-Aldrich (USA). Dibasic sodium phosphate (Na_2HPO_4) (reagent grade) and sodium phosphate monohydrate ($NaH_2PO_4 \cdot H_2O$) (reagent grade) were obtained from Vetec (Brazil). Research-grade CM5 sensor chips and coupling reagents [*N*-ethyl-*N*',*N*''-(dimethylaminopropyl)carbodiimide (EDC), *N*-hydroxysuccinimide, (NHS), and 1 M ethanolamine hydrochloride, pH 8.5] were purchased from GE Healthcare (USA).

2.2. bLF–EGCG binding followed by SPR measurement

The kinetics and thermodynamics of complex formation between bLF and EGCG were studied, in triplicate, by SPR using a Biacore X100 instrument (GE Healthcare, Pittsburgh, PA, USA). The bLF was immobilized on three CM5 sensor chip surfaces [average 3894 resonance units (RU)], using a Biacore Amine Coupling Kit according to the manufacturer's instructions.

The CM5 chips were activated for 7 min with a 1:1 (v/v) EDC/NHS mixture at 0.1 mol L^{-1} for each solution with a flow rate of 20 µL min^{-1}, then 30 µg mL^{-1} of bLF in 10 mmol L^{-1} sodium acetate (pH 4) solution was injected for 7 min, resulting in a low-density immobilization of bLF (about 3894 RU) that minimizes potential mass transport and crowding artifacts. The excess activated carboxyl groups were blocked with ethanolamine for 7 min. To correct for systematic noise and instrument drift, a flow cell was prepared as described above but without the bLF immobilization and used as a reference surface.

The bLF–EGCG interaction was investigated at pH 7.0 and five different temperatures between 12 and 28 ºC. EGCG solutions with concentrations ranging from 30 to 54 µM (30, 32, 34, 36, 38, 40, 42, 44, 46, 48, 50 and 54 µM) were prepared in the flowing buffer. The buffer was injected before each bLF–EGCG binding cycle to obtain the baseline. Real-time complex formation was investigated by an optical method, which measured small changes in the refractive index of the medium near (within ~100 nm) the sensor chip surface and translated them into a change in RU.

2.3. bLF–EGCG binding followed by fluorescence spectroscopy (FS) analysis

Fluorescence spectra were recorded on a LS55 spectrofluorometer (Perkin Elmer Inc, Waltham, USA) equipped with a thermostatted compartment using 1.0 cm quartz cuvettes. The working solution of bLF (2 μM) and EGCG (500 μM) were dissolved in a mixture of phosphate buffer (pH 7.0) and DMSO (buffer: DMSO, 20:1). The interaction of bLF with EGCG was studied by the fluorescence quenching titration method. To a quartz cuvette, 2.0 mL of bLF solution was added, and then a certain amount (25 μL) of polyphenol solution was gradually titrated manually into the cell by using a microinjector. The concentration of EGCG varied from 0 to 65.2 μM (0, 6.2, 12.2, 18.1, 23.8, 29.4, 34.9, 40.2, 45.5, 50.6, 55.6, 60.4 and 65.2 μM), all samples were mixed thoroughly and kept 2 min before measurements. Fluorescence spectra were recorded in the absence and presence of polyphenol in the range of 300–500 nm at the excitation wavelength of 295 nm, at five different temperatures between 20 and 45 ºC. The excitation and emission slit widths were both kept at 5 nm and the scanning speed of 500 nm min^{-1}.

The EGCG absorbs light at wavelengths near the excitation and emission wavelengths used for fluorescence analysis. Therefore, absorbances of the samples at the excitation and emission wavelengths obtained on a UV-vis spectrophotometer were used to correct the inner-filter according to Eq. (1) (van de Weert & Stella, 2011):

$$F_{obs} = F.10^{-\frac{A_{ex}\cdot d_{ex}}{2}-\frac{A_{em}\cdot d_{em}}{2}} \quad (1)$$

where F_{obs} is fluorescence intensity obtained in spectrofluorometer, F is fluorescence intensity after correction of inner-filter effect, A_{ex} and A_{em} the measured change in absorbance value at the excitation and emission wavelength, respectively, caused by polyphenol addition and d_{ex} and d_{em} the cuvette pathlength in the excitation and emission direction (in cm), respectively.

3. Results and discussion

3.1. Kinetic parameters for bLF–EGCG complex formation

Many methods have been reported to study the thermodynamics of the binding of proteins to small molecules, including FS, ITC, and circular dichroism spectroscopy (Hudson et al., 2018; Kanakis et al., 2011; Yang et al., 2014). However, there is a scarcity of methods to determine the kinetic parameters of these interactions. Since SPR

could follow intermolecular interactions in real time, it is possible to obtain the kinetic parameters for the association and dissociation steps through a sensorgram (RU vs. time), as shown in Fig. 1.

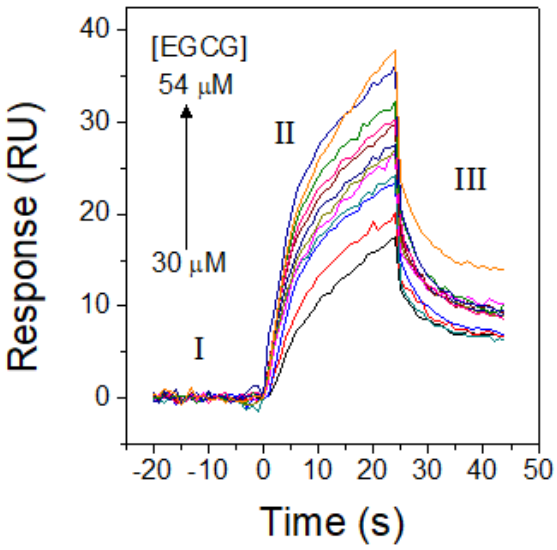

Fig. 1. Sensorgrams (RU vs time) for bLF–EGCG interactions formed by flowing 30-54 µM EGCG solutions over a CM5 low-density bovine lactoferrin-immobilized sensor-chip surface (3890 RU) at 25 ºC. The arrow indicates increasing EGCG concentration from 30 to 54 µM (30, 32, 34, 36, 38, 40, 42, 44, 46, 48, 50 and 54 µM). The sensorgrams obtained for other temperatures are showed in Fig. S2, Supporting Information.

The curves obtained from SPR could be divided into three phases. In phase I (from -20 to 0 s), only the buffer was injected to flow over both reference and bLF-immobilized channels of the sensor chip surface, and no difference in RU was observed. At 0 s, the buffer containing EGCG was injected into the system and flowed over both channels, thus inducing simultaneous bLF–EGCG association and dissociation and increasing the RU (phase II, from 0 to 25 s). After 25 s, the buffer was injected to flow over the CM5 chip surface, and mainly bLF–EGCG dissociation occurred, resulting in a decrease in RU (phase III).

During phases II and III, the kinetics can be represented as follows:

$$\mathrm{bLF} + \mathrm{EGCG} \underset{K_d}{\overset{K_a}{\rightleftarrows}} \mathrm{bLF{-}EGCG}$$

In phase II, with concurrent association and dissociation processes, the net change in bLF– EGCG complex concentration can be described by Eq. (2):

$$d[\text{bLF–EGCG}]/dt = k_a\,[bLF]_f[EGCG]_f - k_d[\text{bLF–EGCG}] \quad (2)$$

Where the first and second terms on the right-hand-side represent the complex formation and dissociation, respectively. $[bLF]_f$ and $[EGCG]_f$ are the concentrations of free bLF and EGCG molecules, k_a and k_d are the association and dissociation rate constants, respectively, and $[\text{bLF–EGCG}]$ is the concentration of complex immobilized on the SPR chip surface. Assuming that RU is proportional to $[\text{bLF–EGCG}]$, Eq. (2) can be rewritten in terms of SPR signal magnitude as:

$$d[RU(t)]/\text{dt} = k_a\,[RU_{max}(t_\infty)] - [RU(t)]\cdot[EGCG]_f - k_d\cdot[RU(t)] \quad (3)$$

where $[RU(t)]$ is the SPR signal obtained in the sensorgram at time t, and $[RU_{\max}(t_\infty)]$ is the SPR response at bLF saturation by EGCG. Considering that $k_a\cdot[EGCG] + k_d = k_{obs}$ (observed rate constant), by solving the differential Eq. (3) we obtained Eq. (4).

$$RU(t) = RU_{max}(t_\infty)[1 - e^{-k_{obs}(t)}] \quad (4)$$

During the dissociation phase (phase III), the RU change was mainly due to the dissociation of the bLF– EGCG complex:

$$\text{bLF–EGCG} \xrightarrow{kd} \text{bLF} + \text{EGCG}$$

The rate of this process can be expressed using SPR signal as:

$$d[RU(t)]/\text{dt} = -k_d\cdot[RU(t)] \quad (5)$$

The solution of the differential Eq. (5) is:

$$RU(t) = RU(t_m)\,e^{-k_d(t-t_m)} \quad (6)$$

where t_m is the time when phase III started.

The k_d and k_{obs} values were obtained by global fitting of the data for phases III and II to Eq. (6) and (4), respectively. At low polyphenol concentrations, the plot of k_{obs} vs. $[EGCG]$ was linear, and thus its slope represented the association rate constant between the free bLF and EGCG molecules.

Both k_a and k_d were measured at five different temperatures and are listed in Table 1. These values increased with increasing temperature, indicating that the higher the average molecular kinetic energy, the more frequent the association of free molecules and the dissociation of the complex. To the best of our knowledge, there are only two studies reporting the kinetic parameters of association between bioactive molecules and proteins. Cuccioloni et al., (2011) obtained the k_a and k_d values for EGCG and hydroxy-3-methyl-glutaryl-CoA reductase (HMGR) at 25 ºC using the IAsys plus biosensor system to be 2.9 × 10^4 L mol^{-1} s^{-1} and 0.0026 s^{-1}, respectively. Their k_a value for HMGR-EGCG is about two times higher than what we obtained for bLF-EGCG at the same temperature. Meanwhile, their k_d value dissociation was remarkably smaller (by a factor of 45). A likely explanation of this difference is that, while EGCG interacts with the cofactor site of the HMGR, the binding site on EGCG for bLF is not very specific, hence the weaker binding. Another example for non-specific site interaction was observed in the complexation of the transport protein bovine serum albumin (BSA) and the bioactive molecule curcumin at 25 ºC, where the k_a and k_d values were found to be 1.49 × 10^4 L mol^{-1} s^{-1} and 0.677 s^{-1}, respectively. Notably, these values are closer to those we obtained, but the k_d of bLF–EGCG was still about six times lower than that of BSA–curcumin (Hudson et al., 2018). Probably, in the former interaction the binding induced a stronger site fitting process (Paul & Weikl, 2016) than in the latter; thus, EGCG left the bLF at a slower rate than that of curcumin dissociation from BSA.

Table 1. Rate constants for the association (k_a) and dissociation (k_d) of the bLF–EGCG complex.

T	k_a	k_d
ºC	10^4 M^{-1} s^{-1}	s^{-1}
12	0.65 ± 0.02	0.061 ± 0.003
16	0.85 ± 0.04	0.068 ± 0.004
20	1.08 ± 0.07	0.083 ±0.006
24	1.25 ± 0.06	0.093 ± 0.008
25	1.65 ± 0.09	0.118 ± 0.010
28	2.08 ± 0.12	0.134 ± 0.011

Unfortunately, the previous study did not discuss the dependence of k_a and k_d on temperature, which will give the energetic parameters related to the formation and dissociation of the activated (or intermediate) complex, respectively. The activation energy (E_{act}) for the formation of the activated complex through association (a) or dissociation (d) was obtained using the Arrhenius approach (ln k_x ($x = a\ or\ d$) vs. 1/T, Fig. 2) by applying Eq. (7).

$$E_{act(x)}\ (T) = -R\ (d \ln k_x\ /d\ T) \tag{7}$$

where k_x (T) is the rate constant for $x = a$ or d (with the respective units of L mol^{-1} s^{-1} or s^{-1}) at temperature T (K), $E_{act(x)}$ (T) is the corresponding activation energy (kJ mol^{-1}), and R is the universal gas constant (8.3145 J mol^{-1} K^{-1}).

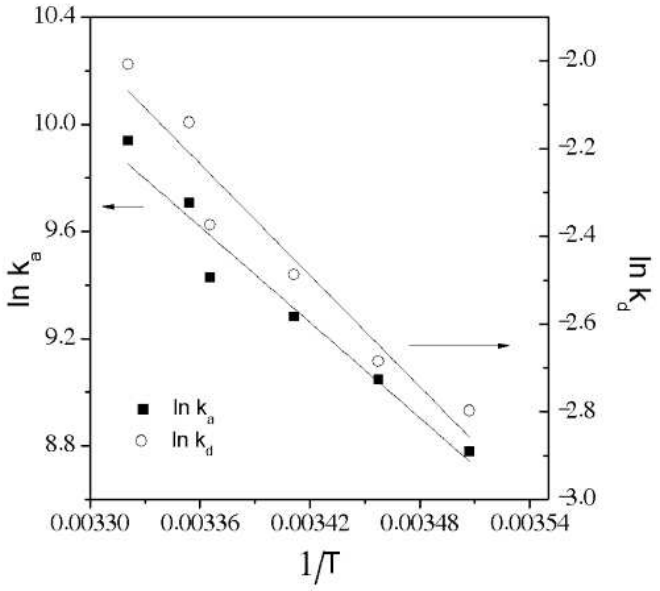

Fig. 2. Arrhenius plots of ln k_a (■) and ln k_d (○) associated with bLF−EGCG interactions as a function of inverse temperature.

The linearity of the Arrhenius plot suggests that the formation of the activated complex from free molecules association or from complex stable dissociation occurred in a single and simple step of induced fit site (Wang & Roberts, 2013). Yang et al., (2014) used a far-UV CD technique to find that, in the presence of 250 μM EGCG, there was a significant increase of bLF α-helix structures (from 21.2% to 31.9%) together with a remarkable reduction of β-sheet content (from 30.4% to 18.3%), while the content of the β-turn and unordered coil did not change notably. Therefore, the authors concluded that EGCG induced a progressive increase in the bLF α-helix/β-sheet ratio.

Our results showed that the E_{act} values were positive for both processes ($E_{act(a)}$ = + 49.5 kJ mol^{-1} and $E_{act(d)}$ = + 35.2 kJ mol^{-1}), showing that the association process absorbed 1.4 times more energy than the dissociation process. Hence, the formation of their activated complex from free reactants incurs a larger potential energy change than from the reverse direction (i.e., from the dissociation of the stable bLF−EGCG complex). De Paula et al. (2017) determined the E_{act} for the interaction between BSA and Congo Red (CR). The E_{act} values for the BSA-CR activated complex ($E_{act(a)}$ = + 35.9 kJ mol^{-1} and $E_{act(d)}$ = + 20.2 kJ mol^{-1}) were smaller than those found for the bLF−EGCG activated complex here. Therefore, despite the larger molecular volume of

CR compared to EGCG, the latter induced a larger conformational change in bLF than that of CR induced in BSA.

To determine the driving force for forming the activated complex, we calculated the activation Gibbs free energy changes according to Eq. (8), and its components [the activation enthalpy change ($\Delta H_x^{\ddagger}$), and the activation entropy change ($T\Delta S_x^{\ddagger}$)] using Eqs. (9) and (10), respectively.

$$\Delta G_x^{\ddagger}(T) = -RTln(k_x h/k_B T) \quad (8)$$

$$\Delta H_x^{\ddagger}(T) = E_{act(x)}(T) - RT \quad (9)$$

$$T\Delta S_x^{\ddagger}(T) = \Delta H_x^{\ddagger}(T) - \Delta G_x^{\ddagger}(T) \quad (10)$$

where h is the Planck's constant (6.62608 × 10^{-34} J s) and k_B is the Boltzmann constant (1.38066 × 10^{-23} J K^{-1}) at temperature T (K).

Interestingly, despite the higher $E_{act(a)}$ than $E_{act(d)}$, $\Delta G_a^{\ddagger}$ was smaller than $\Delta G_d^{\ddagger}$ (49.1 and 77.9 kJ mol^{-1}, respectively), indicating that the activated complex formation was faster from substrate association than from the dissociation of the stable complex. In order to understand the difference between the $\Delta G_a^{\ddagger}$ and $\Delta G_d^{\ddagger}$ values, we need to analyze their components ($\Delta H_x^{\ddagger}$ and $\Delta S_x^{\ddagger}$).

The formation of the activated complex from the free molecules (bLF and EGCG) association and bLF–EGCG stable complex dissociation was endothermic, with $\Delta H^{\ddagger}$ decreasing at higher temperatures in both cases. However, the activation enthalpy change was higher for the association ($\Delta H_{a\,(25\,^{\circ}C)}^{\ddagger}$ = 47.02 kJ mol^{-1}) than for the dissociation process ($\Delta H_{d\,(25\,^{\circ}C)}^{\ddagger}$ = 32.8 kJ mol^{-1}). In both cases, activated complex formation was accompanied by an entropy reduction ($T\Delta S_a^{\ddagger}$ = -2.10 kJ mol^{-1} and $T\Delta S_d^{\ddagger}$ = -45.10 kJ mol^{-1}, respectively) that was remarkable smaller for the association. This indicates that the dissociation of the activated complex to form the stable complex induced more conformational changes in the biopolymer than the formation of the activated complex from free reactants.

3.2. Thermodynamic parameters for bLF–EGCG complex formation obtained by SPR

Thermodynamic characterization of the bLF–EGCG complex formation was carried out to complement the kinetic study and gain further insight into the driving forces for complex formation. The thermodynamic parameters were calculated from the relationship between the kinetic rate constants of association (k_a) and dissociation (k_d) (Table 1) obtained by SPR (Day, Baird, Rich, & Myszka, 2002; Navratilova et al., 2007) at each temperature, according to Eqs. (11-14):

$$K_b = k_a/k_d \tag{11}$$

$$\Delta G^0 = -RTlnK_b \tag{12}$$

$$ln\,(K_{b2}/K_{b1}) = -\Delta H^0/R.(1/T_2 - 1/T_1) \tag{13}$$

$$T\Delta S^0 = \Delta H^0 - \Delta G^o \tag{14}$$

where K_b is the binding constant (L mol^{-1}), ΔG^0 is the standard Gibbs free energy change (kJ mol^{-1}), T is the temperature (K), R is the universal gas constant (8.3145 J mol^{-1} K^{-1}), ΔH^0 is the standard enthalpy change (kJ mol^{-1}), and ΔS^0 is the standard entropy change (kJ mol^{-1} T^{-1}).

The obtained thermodynamic parameters of bLF–EGCG complex formation are shown in Table 2. The K_b values obtained by SPR (K_b^{SPR}) were approximately 10^5 L mol^{-1} and these values increased with increasing temperature, showing that the complex formation was an endothermic process. The binding constants at 25 ºC determined by FS technique between EGCG and other milk proteins, such as α-casein (mixture of α_{s1}- and α_{s2}-caseins), β-casein, and β-lactoglobulin, were 7.4×10^3, 1.59×10^4, and 1.3×10^4 L mol^{-1}, respectively (Hasni et al., 2011; Kanakis et al., 2011). These values demonstrate that the bLF–EGCG interaction determined in our work is 10 to 20 times stronger than the EGCG interaction with these other milk proteins, suggesting bLF to be a promising EGCG carrier protein in different formulations. Despite the different thermodynamic conditions (pH 6.0 and EGCG and bLF concentration range) and the experimental technique (ITC) used by Yang et al., (2014), they obtained a K_b value very

close (1.36×10^5 L mol^{-1}) to ours, showing agreement between the ITC and SPR techniques. On the other hand, the K_b value for the EGCG–HMGR complex obtained using another optic sensor device was in the order of 10^7 L mol^{-1}. As previously discussed for the kinetic data, this high K_b value is attributed to the interaction of EGCG with a cofactor site of the HMGR (Cuccioloni et al., 2011). The negative ΔG^o_{SPR} values in the present study show that the system's chemical equilibrium favors the formation of the bLF–EGCG complex at all temperatures. The ΔG^o_{SPR} values also decreased with increasing temperature, indicating that the complexes were more stable at higher temperatures under the conditions we used.

Table 2. Thermodynamic parameters: Binding constant (K_b) and standard changes in Gibbs free energy (ΔG^0), enthalpy (ΔH^0), and entropy ($T\Delta S^0$) for the formation of the bLF–EGCG complex at different temperatures (T) and pH 7.0, obtained by surface plasmon resonance studies.

T (ºC)	K_b *	ΔH^0 **	R^2	ΔG^0 **	$T\Delta S^0$ **
12	1.06 ± 0.06	14.26±0.93	0.91	-27.45± 1.65	41.70±2.50
16	1.25 ± 0.09			-28.21±1.97	42.47±2.97
20	1.29 ± 0.08			-28.69±1.72	42.94±2.58
24	1.34 ± 0.10			-29.16± 2.33	43.42±3.47
25	1.40 ± 0.07			-29.37±1.46	43.63±2.18
28	1.56 ±0.11			-29.91±2.10	44.17± 3.09

* 10^5 L mol^{-1}, ** kJ mol^{-1}.

To understand the driving force to form the bLF-EGCG stable complex the enthalpic and entropic contributions were analyzed. The positive ΔH^o_{SPR} and $T\Delta S^o_{SPR}$ values indicate that this complex formation is entropically driven. A few studies have reported the thermodynamic parameters of interaction between EGCG and proteins such as proline-rich protein (Poncet-Legrand et al., 2007), amyloid β-peptide 42 (Wang, Liu, Dong, & Sun, 2010) and its fragments (Wang et al., 2012b), porcine gastric mucin (Zhao et al., 2012), insulin (Wang et al., 2012a), and pepsin (X. Wu et al., 2013). Contrary to our results, most of these studies reported the EGCG-protein interactions to be enthalpically driven ($-8 < \Delta H^0 < -30$ kJ mol^{-1}) and entropically unfavorable ($-50 < T\Delta S^0 < -0.9$ kJ mol^{-1}), except for the EGCG-amyloid β-peptide 42, which

showed positive ΔH^0 and $T\Delta S^0$ values (2.09 and 35.12 kJ mol^{-1}, respectively) (Wang et al., 2012). However, it is important to emphasize that proteins studied in the other papers are chemically and structurally distinct from bLF. Generally, thermodynamic results associated with positive ΔH^0 and $T\Delta S^0$ values are related with intermolecular interactions dominated by hydrophobic interactions between protein and ligand. The bLF has different hydrophobic regions (Bruni et al., 2016). Probably, the interaction between bLF and EGCG occurred in a hydrophobic pocket of this protein as well as it was found for EGCG-amyloid β-peptide 42, and thus hydrophobic interactions dominated the binding.

To the best of our knowledge, there is only one study of the interaction between EGCG and bLF (Yang et al., 2014), and the thermodynamic parameters reported therein were notably different from ours. However, in that case, conditions such as temperature, EGCG and bLF concentration ranges, and the buffer pH (6.0) were completely different from those used in our research. The entropy increase observed in our system could be attributed to: i) the configurational entropy gain associated with the release of the water/ion solvation shells from bLF and EGCG and ii) the conformation change of the bLF and EGCG molecules. Similar results were reported for other complexes between proteins and small ligands (de Paula et al., 2017; Hudson et al., 2018; Yuksel, Avci, & Erdem, 2010).

To evaluate the enthalpic contribution (ΔH^o_{SPR}), the effect of three molecular processes must be considered: the desolvation of bLF ($\Delta H_{des-bLF}$) and EGCG ($\Delta H_{des-EGCG}$) surfaces and the bLF–EGCG interaction ($\Delta H_{bLF-EGCG}$), as shown in Eq. (15).

$$\Delta H^o_{SPR} = \Delta H_{des-bLF} + \Delta H_{des-EGCG} + \Delta H_{bLF-EGCG} \quad (15)$$

The obtained positive ΔH^o_{SPR} value suggests that the energetic cost for bLF and EGCG desolvation was higher than the energy released by the interaction between the two molecules. Considering that EGCG contains three aromatic rings and eight hydroxyl groups (Fig. S1, Supporting Information), it can be inferred that EGCG-protein binding is mainly driven by hydrophobic interactions and hydrogen bonding. The hydrophobic interactions can occur between polyphenolic rings and hydrophobic amino acid residues, whereas the hydrogen bonds are formed between the hydroxyl

groups of EGCG and the amino or carbonyl groups of amino acid residues or side chains (Hasni et al., 2011; Yuksel et al., 2010). As the pI of bLF is approximately 8.5 and the pKa of phenolate groups is >7 (pKa of EGCG = 7.68), at pH 7.0 the protein is positively charged whereas EGCG is neutral (Muzolf, Szymusiak, Gliszczyńska-Świgło, Rietjens, & Tyrakowska, 2008; Yang et al., 2014), suggesting that electrostatic forces did not directly contribute to the interaction between EGCG and bLF in this case.

3.3. Thermodynamic parameters for bLF–EGCG complex formation obtained by FS

Considering that SPR is a relatively new technique to study binding between proteins and bioactive molecules, it is relevant to compare the SPR results with those obtained by a widely used technique for this purpose. Therefore, we performed the bLF–EGCG binding experiments using FS. This procedure differs from SPR because protein and ligand are in solution; moreover, FS focuses only on the interactions occurring in the fluorophore regions, mainly in sites containing Tryptophan (Trp).

The bLF has 13 Trp residues (Trp-8, Trp-16, Trp-22, Trp-24, Trp-125, Trp-138, Trp-268, Trp-347, Trp-361, Trp-448, Trp-467, Trp-549, and Trp-560) (Stănciuc et al., 2013), which conferred its intrinsic fluorescence, emitted with intensity at maximum wavelength (λ_{max}) at 334 nm. The addition of increasing EGCG concentrations into bLF solution quenched its fluorescence intensity emitted by the protein and leaded λ_{max} to a 4 nm red-shift (Fig. 3a). This red-shift indicates that Trp residues were moved to a more hydrophilic region (Condict, Kaur, Hung, Ashton, & Kasapis, 2019), without any relevant global protein conformational change. There was only a conformational change in the binding site on bLF for EGCG.

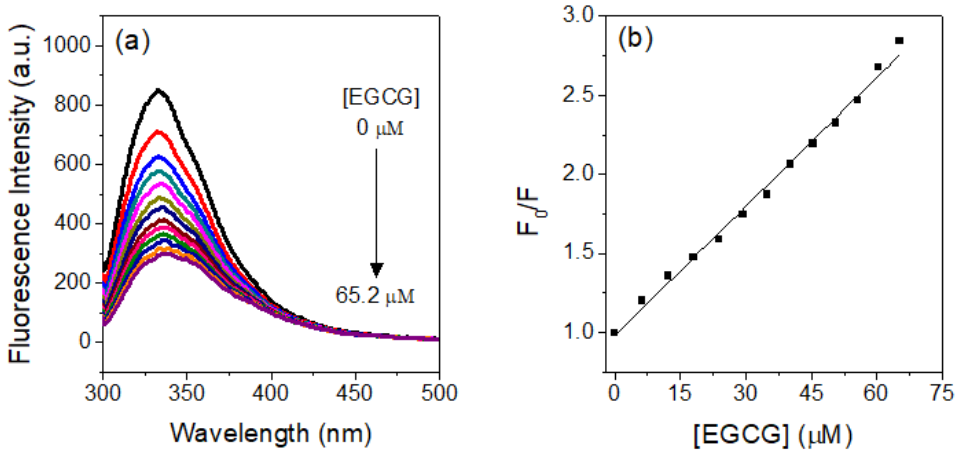

Fig. 3. (a) Fluorescence spectra of bLF (2 μM) with increasing concentrations of EGCG. The arrow indicates indicates increasing EGCG concentration from 0 to 65.2 μM (0, 6.2, 12.2, 18.1, 23.8, 29.4, 34.9, 40.2, 45.5, 50.6, 55.6, 60.4 and 65.2 μM), and (b) Stern-Volmer plot (F_0/F vs. EGCG concentration) for bLF interacting with increasing EGCG concentrations, at 25 °C and pH 7. The fluorescence spectra obtained for other temperatures are shown in Fig. S3, Supporting Information.

The fluorescence data were analyzed using the Stern-Volmer equation (Eq. 16).

$$\frac{F_0}{F} = 1 + K_{sv}[Q] = 1 + K_q\tau_0[Q] \quad (16)$$

Where F_0 and F are the fluorescence intensities of bLF before and after the addition of the EGCG, respectively, $[Q]$ is the EGCG concentration (mol·L^{-1}), K_{sv} is the Stern-Volmer quenching constant, τ_0 is the average protein fluorescence lifetime in the absence of the quencher (~10^{-8} s), and K_q is the biomolecular quenching constant.

From the fluorescence intensities, the values of K_{sv} were determined by linear regression (F_0/F vs. [Q]) (Fig. 3b). As K_{sv} values ranged from 2.48×10^4 to 3.97×10^4 L mol^{-1}, so the K_q values were of the order of 10^{12} L·mol^{-1}·s^{-1}, which are at least 100-fold higher than the maximum value for a diffusion-controlled quenching process (10^{10} L·mol^{-1}·s^{-1}) (Ren, Xiong, Li, & Li, 2019). Hence, the static mechanism is predominant in the complex formation between bLF and EGCG.

The thermodynamic binding parameters obtained by fluorescence, binding constant (K_b^{FS}) and stoichiometry (n) for the complex were further investigated using the modified Stern-Volmer model (Eq. 17). While the ΔG_{FS}^o, ΔH_{FS}^o, and $T\Delta S_{FS}^o$ values were calculated through previously discussed Eqs. 12, 13, and 14, respectively. The van't Hoff plot used to obtain ΔH_{FS}^o is shown in Fig. 4.

$$log\frac{F0-F}{F} = n\ logK_b - n\log\frac{1}{\left([Qt]-\left(\frac{F0-F}{F0}\right)[P]\right)} \quad (17)$$

Where F_0 and F are the fluorescence intensities of bLF in the absence and presence of EGCG, respectively, [Qt] is the total EGCG concentration, and [P] is the total bLF

concentration. The n value was obtained from the slope of the curve $log\frac{F0-F}{F}$ vs. $\log\frac{1}{\left([Qt]-\left(\frac{F0-F}{F0}\right)[P]\right)}$, and the K_b^{FS} value was found from its intercept.

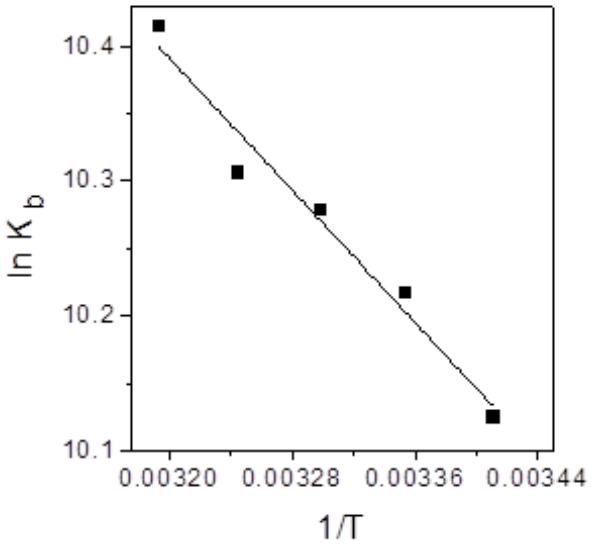

Fig. 4. The van't Hoff plot of bLF interaction with EGCG.

The thermodynamic parameters for the bLF–EGCG interaction obtained by FS are shown in Table 3. The K_b^{FS} values were of the order of 10^4 L mol^{-1} and, they also increased with temperature increment, displaying that, like SPR, more complexes were formed at superior temperatures. Negative ΔG_{FS}^o values were also found by FS at all temperatures, pointing to the product (bLF–EGCG) was favored in relation to the reactants (bLF and EGCG) in the equilibrium bLF + EGCG ⇋ bLF-EGCG. Regarding the ΔG_{FS}^o contributors, ΔH_{FS}^o and the $T\Delta S_{FS}^o$ values were 10.20±0.56 and 34.88-37.32 kJ mol^{-1}, respectively, which was very similar from those found by SPR (ΔH_{SPR}^o = 14.26 kJ mol^{-1} and $T\Delta S_{SPR}^o$ = 41.70 – 44.17 kJ mol^{-1}). This similarity between thermodynamic parameters measured by SPR and FS suggested that the main bLF-EGCG interaction sites are around Trp residues, and that biopolymer relative confinement on the CM5 chip surface did not alter the molecular mechanism of bLF-EGCG binding, as previously discussed on the SPR section.

4. Conclusion

Using the surface plasmon resonance and fluorescence spectroscopy techniques, EGCG was found to interact with bLF to form a thermodynamically stable complex at pH = 7, driven by an increase in the system's entropy. Thermodynamic parameters obtained by both techniques (SPR and FS) were very similar, suggesting that bLF-EGCG interaction occurs close to Trp surroundings, through one step molecular mechanism. SPR kinetic analysis of the formation of stable bLF-EGCG complex revealed the existence of an activated complex, and the potential barrier energy (PBE) of the system is higher on the association than on the dissociation step ($E_{act\ (a)}$ = 49.5 kJ mol^{-1} and $E_{act\ (d)}$ = 17.4 kJ mol^{-1}).

The formation of the activated complex from free EGCG and bLF molecules resulted in a small extension of biopolymer conformational site change, as shown by the small entropy decrease (-2.10 kJ mol^{-1}). On the other hand, forming the activated complex from the stable complex promoted in the former a large extension of conformational site change when compared with last structure, as expressed by the significant entropy decrease of 45.10 kJ mol^{-1}.

The increased in the temperature enhanced the kinetic rates of association and dissociation but in higher intensity the former. Consequently, a higher binding constant and stability occurred in higher temperatures, evidencing the role of temperature on the formation and stabilization of bLF-EGCG complexes.

In this standpoint, our study provided a complete kinetic and thermodynamic characterization of bLF-EGCG complex formation, yielding insights on the molecular dynamic occurring on the bLF binding site and EGCG molecules. These data could help optimize the practical applications of EGCG and bLF in different formulations.

Acknowledgments

The authors wish to thank the Coordenação de Aperfeiçoamento de Pessoal de Nível Superior (CAPES), Conselho Nacional de Desenvolvimento Científico e Tecnológico (CNPq), and Fundação de Apoio à Pesquisa de Minas Gerais (FAPEMIG) for their financial support.

Competing interests

The authors have declared that no competing interests exist.

References

Abd El-Rahman, S. S., Shehab, G., & Nashaat, H. (2017). Epigallocatechin-3-Gallate: The Prospective Targeting of Cancer Stem Cells and Preventing Metastasis of Chemically-Induced Mammary Cancer in Rats. *The American Journal of the Medical Sciences*, *354*(1), 54–63. https://doi.org/10.1016/J.AMJMS.2017.03.001

Bourbon, A. I., Cerqueira, M. A., & Vicente, A. A. (2016). Encapsulation and controlled release of bioactive compounds in lactoferrin-glycomacropeptide nanohydrogels: Curcumin and caffeine as model compounds. *Journal of Food Engineering*, *180*, 110–119. https://doi.org/10.1016/j.jfoodeng.2016.02.016

Bruni, N., Capucchio, M. T., Biasibetti, E., Pessione, E., Cirrincione, S., Giraudo, L., … Dosio, F. (2016). Peptides and Applications in Human and Veterinary Medicine. *Molecules*, *21*, 1–25. https://doi.org/10.3390/molecules21060752

Chaharband, F., Kamalinia, G., Atyabi, F., Mortazavi, S. A., Mirzaie, Z. H., & Dinarvand, R. (2018). Formulation and in vitro evaluation of curcumin-lactoferrin conjugated nanostructures for cancerous cells. *Artificial Cells, Nanomedicine and Biotechnology*, *46*(3), 626–636. https://doi.org/10.1080/21691401.2017.1337020

Chung, J. E., Tan, S., Gao, S. J., Yongvongsoontorn, N., Kim, S. H., Lee, J. H., … Ying, J. Y. (2014). Self-assembled micellar nanocomplexes comprising green tea catechin derivatives and protein drugs for cancer therapy. *Nature Nanotechnology*, *9*(11), 907–912. https://doi.org/10.1038/nnano.2014.208

Condict, L., Kaur, J., Hung, A., Ashton, J., & Kasapis, S. (2019). Combined spectroscopic, molecular docking and quantum mechanics study of β-casein and ferulic acid interactions following UHT-like treatment. *Food Hydrocolloids*, *89*, 351–359. https://doi.org/10.1016/J.FOODHYD.2018.10.055

Cuccioloni, M., Mozzicafreddo, M., Spina, M., Tran, C. N., Falconi, M., Eleuteri, A. M., & Angeletti, M. (2011). Epigallocatechin-3-gallate potently inhibits the in vitro activity of hydroxy-3-methyl-glutaryl-CoA reductase. *Journal of Lipid Research*, *52*(5), 897–907. https://doi.org/10.1194/jlr.M011817

Day, Y. S. N., Baird, C. L., Rich, R. L., & Myszka, D. G. (2002). Direct comparison of binding equilibrium , thermodynamic , and rate constants determined by surface- and solution-based biophysical methods. *Protein Science*, *11*, 1017–1025. https://doi.org/10.1110/ps.4330102.the

de Paula, H. M. C., Coelho, Y. L., Agudelo, A. J. P., Rezende, J. de P., Ferreira, G. M. D., Ferreira, G. M. D., … da Silva, L. H. M. (2017). Kinetics and thermodynamics of bovine serum albumin interactions with Congo red dye. *Colloids and Surfaces B: Biointerfaces*, *159*, 737–742. https://doi.org/10.1016/j.colsurfb.2017.08.036

Du, X., Li, Y., Xia, Y.-L., Ai, S.-M., Liang, J., Sang, P., … Liu, S.-Q. (2016). Insights into Protein–Ligand Interactions: Mechanisms, Models, and Methods. *International Journal of Molecular Sciences*, *17*(2), 144. https://doi.org/10.3390/ijms17020144

Głąb, T. K., & Boratyński, J. (2017). Potential of Casein as a Carrier for Biologically Active Agents. *Topics in Current Chemistry*, *375*(4). https://doi.org/10.1007/s41061-017-0158-z

Hasni, I., Bourassa, P., Hamdani, S., Samson, G., Carpentier, R., & Tajmir-Riahi, H.-A.

(2011). Interaction of milk α- and β-caseins with tea polyphenols. *Food Chemistry*, *126*(2), 630–639. https://doi.org/10.1016/j.foodchem.2010.11.087

Hudson, E. A., de Paula, H. M. C., Ferreira, G. M. D., Ferreira, G. M. D., Hespanhol, M. do C., da Silva, L. H. M., & Pires, A. C. dos S. (2018). Thermodynamic and kinetic analyses of curcumin and bovine serum albumin binding. *Food Chemistry*, *242*, 505–512. https://doi.org/10.1016/j.foodchem.2017.09.092

Kanakis, C. D., Hasni, I., Bourassa, P., Tarantilis, P. A., Polissiou, M. G., & Tajmir-Riahi, H.-A. (2011). Milk β-lactoglobulin complexes with tea polyphenols. *Food Chemistry*, *127*(3), 1046–1055. https://doi.org/10.1016/j.foodchem.2011.01.079

Leilabadi-Asl, A., Divsalar, A., Saboury, A. A., & Parivar, K. (2018). Probing the interaction of two chemotherapeutic drugs of oxali-palladium and 5-fluorouracil simultaneously with milk carrier protein of β-lactoglobulin. *International Journal of Biological Macromolecules*, *112*, 422–432. https://doi.org/10.1016/j.ijbiomac.2018.01.067

Li, H.-Y., Li, M., Luo, C., Wang, J.-Q., & Zheng, N. (2017). Lactoferrin Exerts Antitumor Effects by Inhibiting Angiogenesis in a HT29 Human Colon Tumor Model. *Journal of Agricultural and Food Chemistry*, acs.jafc.7b03390. https://doi.org/10.1021/acs.jafc.7b03390

Liu, F., Wang, D., Ma, C., & Gao, Y. (2016). Conjugation of polyphenols prevents lactoferrin from thermal aggregation at neutral pH. *Food Hydrocolloids*, *58*, 49–59. https://doi.org/10.1016/j.foodhyd.2016.02.011

Muzolf, M., Szymusiak, H., Gliszczyńska-Świgło, A., Rietjens, I. M. C. M., & Tyrakowska, B. (2008). pH-Dependent Radical Scavenging Capacity of Green Tea Catechins. *Journal of Agricultural and Food Chemistry*, *56*(3), 816–823. https://doi.org/10.1021/jf0712189

Navratilova, I., Papalia, G. A., Rich, R. L., Bedinger, D., Brophy, S., Condon, B., … Myszka, D. G. (2007). Thermodynamic benchmark study using Biacore technology. *Analytical Biochemistry*, *364*(1), 67–77. https://doi.org/10.1016/j.ab.2007.01.031

Paul, F., & Weikl, T. R. (2016). How to Distinguish Conformational Selection and Induced Fit Based on Chemical Relaxation Rates. *PLoS Computational Biology*, *12*(9), 1–17. https://doi.org/10.1371/journal.pcbi.1005067

Poncet-Legrand, C., Gautier, C., Cheynier, V., & Imberty, A. (2007). Interactions between Flavan-3-ols and Poly (L-proline) Studied by Isothermal Titration Calorimetry : Effect of the Tannin Strucuture. *Journal of Agricultural and Food Chemistry*, *55*, 9235–9240. https://doi.org/10.1021/jf071297o

Ren, C., Xiong, W., Li, J., & Li, B. (2019). Comparison of binding interactions of cyanidin-3-O-glucoside to β-conglycinin and glycinin using multi-spectroscopic and thermodynamic methods. *Food Hydrocolloids*, *92*, 155–162. https://doi.org/10.1016/J.FOODHYD.2019.01.053

Scala, M. C., Sala, M., Pietrantoni, A., Spensiero, A., Di Micco, S., Agamennone, M., … Campiglia, P. (2017). Lactoferrin-derived Peptides Active towards Influenza: Identification of Three Potent Tetrapeptide Inhibitors. *Scientific Reports*, *7*(1), 10593. https://doi.org/10.1038/s41598-017-10492-x

Shapira, A., Assaraf, Y. G., & Livney, Y. D. (2010). Beta-casein nanovehicles for oral delivery of chemotherapeutic drugs. *Nanomedicine: Nanotechnology, Biology, and Medicine*, *6*, 119–126. https://doi.org/10.1016/j.nano.2009.06.006

Sharma, N., Murali, A., Singh, S. K., & Giri, R. (2017). Epigallocatechin gallate, an active green tea compound inhibits the Zika virus entry into host cells via binding the envelope protein. *International Journal of Biological Macromolecules*, *104*, 1046–1054. https://doi.org/10.1016/j.ijbiomac.2017.06.105

Siqueiros-Cendón, T., Arévalo-Gallegos, S., Iglesias-Figueroa, B. F., García-Montoya, I. A., Salazar-Martínez, J., & Rascón-Cruz, Q. (2014). Immunomodulatory effects of lactoferrin. *Acta Pharmacologica Sinica*, *35*(5), 557–566. https://doi.org/10.1038/aps.2013.200

Stănciuc, N., Aprodu, I., Râpeanu, G., van der Plancken, I., Bahrim, G., & Hendrickx, M. (2013). Analysis of the Thermally Induced Structural Changes of Bovine Lactoferrin. *Journal of Agricultural and Food Chemistry*, *61*(9), 2234–2243. https://doi.org/10.1021/jf305178s

van de Weert, M., & Stella, L. (2011). Fluorescence quenching and ligand binding: A critical discussion of a popular methodology. *Journal of Molecular Structure*, *998*(1–3), 144–150. https://doi.org/10.1016/J.MOLSTRUC.2011.05.023

Walker, J. M., Klakotskaia, D., Ajit, D., Weisman, G. A., Wood, W. G., Sun, G. Y., … Schachtman, T. R. (2015). Beneficial Effects of Dietary EGCG and Voluntary Exercise on Behavior in an Alzheimer's Disease Mouse Model. *Journal of Alzheimer's Disease*, *44*(2), 561–572. https://doi.org/10.3233/JAD-140981

Wang, S.-H., Dong, X.-Y., & Sun, Y. (2012). Thermodynamic Analysis of the Molecular Interactions between Amyloid β-Protein Fragments and (−)-Epigallocatechin-3-gallate. *The Journal of Physical Chemistry B*, *116*(20), 5803–5809. https://doi.org/10.1021/jp209406t

Wang, S.-H., Liu, F.-F., Dong, X.-Y., & Sun, Y. (2010). Thermodynamic Analysis of the Molecular Interactions between Amyloid β-Peptide 42 and (−)-Epigallocatechin-3-gallate. *The Journal of Physical Chemistry B*, *114*(35), 11576–11583. https://doi.org/10.1021/jp1001435

Wang, S. H., Liu, F. F., Dong, X. Y., & Sun, Y. (2012). Calorimetric and spectroscopic studies of the interactions between insulin and (-)-epigallocatechin-3-gallate. *Biochemical Engineering Journal*, *62*, 70–78. https://doi.org/10.1016/j.bej.2012.01.005

Wang, W., & Roberts, C. J. (2013). Non-Arrhenius Protein Aggregation. *The AAPS Journal*, *15*(3), 840–851. https://doi.org/10.1208/s12248-013-9485-3

Wu, M., Jin, J., Jin, P., Xu, Y., Yin, J., Qin, D., … Du, Q. (2017). Epigallocatechin gallate-β-lactoglobulin nanoparticles improve the antitumor activity of EGCG for inducing cancer cell apoptosis. *Journal of Functional Foods*, *39*, 257–263. https://doi.org/10.1016/J.JFF.2017.10.038

Wu, X., He, W., Yao, L., Zhang, H., Liu, Z., Wang, W., … Cao, J. (2013). Characterization of binding interactions of (-)-epigallocatechin-3-gallate from green tea and lipase. *Journal of Agricultural and Food Chemistry*, *61*(37), 8829–8835. https://doi.org/10.1021/jf401779z

Xu, Q., Langley, M., Kanthasamy, A. G., & Reddy, M. B. (2017). Epigallocatechin Gallate Has a Neurorescue Effect in a Mouse Model of Parkinson Disease. *The Journal of Nutrition*, *147*(10), 1926–1931. https://doi.org/10.3945/jn.117.255034

Yang, C. S., Wang, X., Lu, G., & Picinich, S. C. (2009). Cancer prevention by tea: animal studies, molecular mechanisms and human relevance. *Nature Reviews*

Cancer, *9*(6), 429–439. https://doi.org/10.1038/nrc2641

Yang, W., Liu, F., Xu, C., Yuan, F., & Gao, Y. (2014). Molecular interaction between (-)-epigallocatechin-3-gallate and bovine lactoferrin using multi-spectroscopic method and isothermal titration calorimetry. *Food Research International*, *64*, 141–149. https://doi.org/10.1016/j.foodres.2014.06.001

Yuksel, Z., Avci, E., & Erdem, Y. K. (2010). Characterization of binding interactions between green tea flavanoids and milk proteins. *Food Chemistry*, *121*(2), 450–456. https://doi.org/10.1016/j.foodchem.2009.12.064

Zagury, Y., Kazir, M., & Livney, Y. D. (2019). Improved antioxidant activity, bioaccessibility and bioavailability of EGCG by delivery in β-lactoglobulin particles. *Journal of Functional Foods*, *52*, 121–130. https://doi.org/10.1016/J.JFF.2018.10.025

Zhao, Y., Chen, L., Yakubov, G., Aminiafshar, T., & Han, L. (2012). Experimental and Theoretical Studies on the Binding of Epigallocatechin Gallate to Puri fi ed Porcine Gastric Mucin. *The Journal of Physical Chemistry B*, *116*, 13010–13016.

Supporting Information

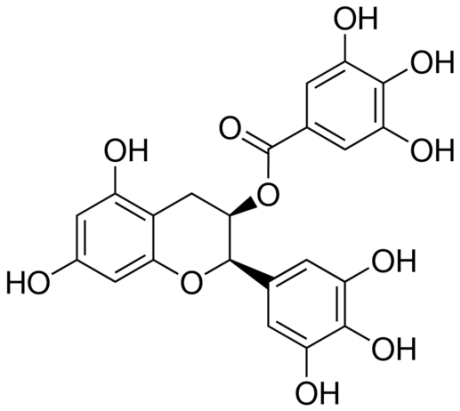

Fig. S1. Chemical structure of (−)-Epigallocatechin-3-gallate

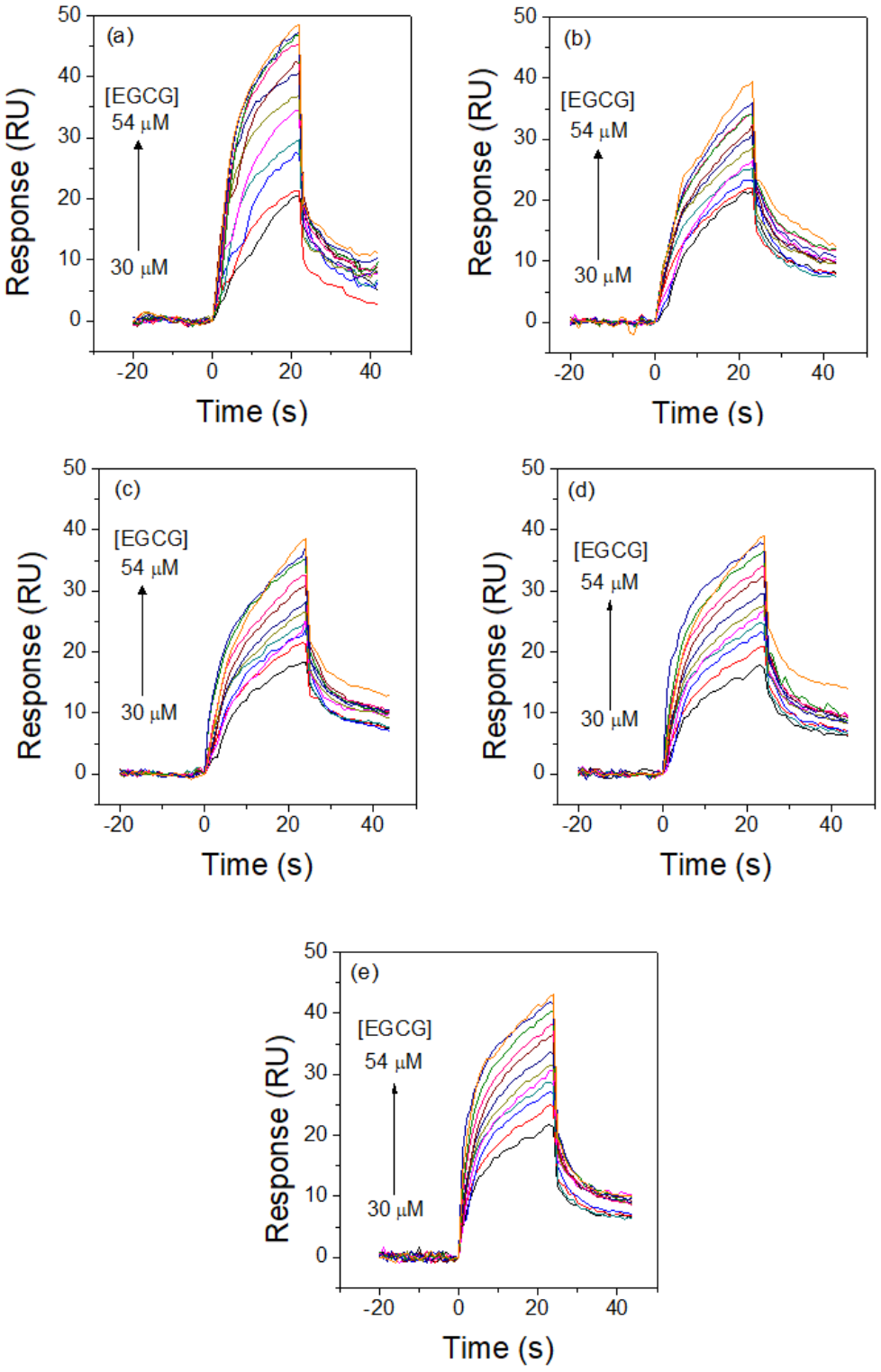

Fig. S2. Sensograms (RU vs Time) for bLF–EGCG interactions formed by flowing 30-54 μM EGCG solutions over a CM5 low-density bovine lactoferrin-immobilized sensor-chip surface (3890 RU), at following temperatures: (a) 12 ºC, (b) 16 ºC, (c) 20 ºC, (d) 24 ºC, (e) 28 ºC, and at pH 7.0. The arrow indicates increasing EGCG concentration from 30 to 54 μM (30, 32, 34, 36, 38, 40, 42, 44, 46, 48, 50 and 54 μM).

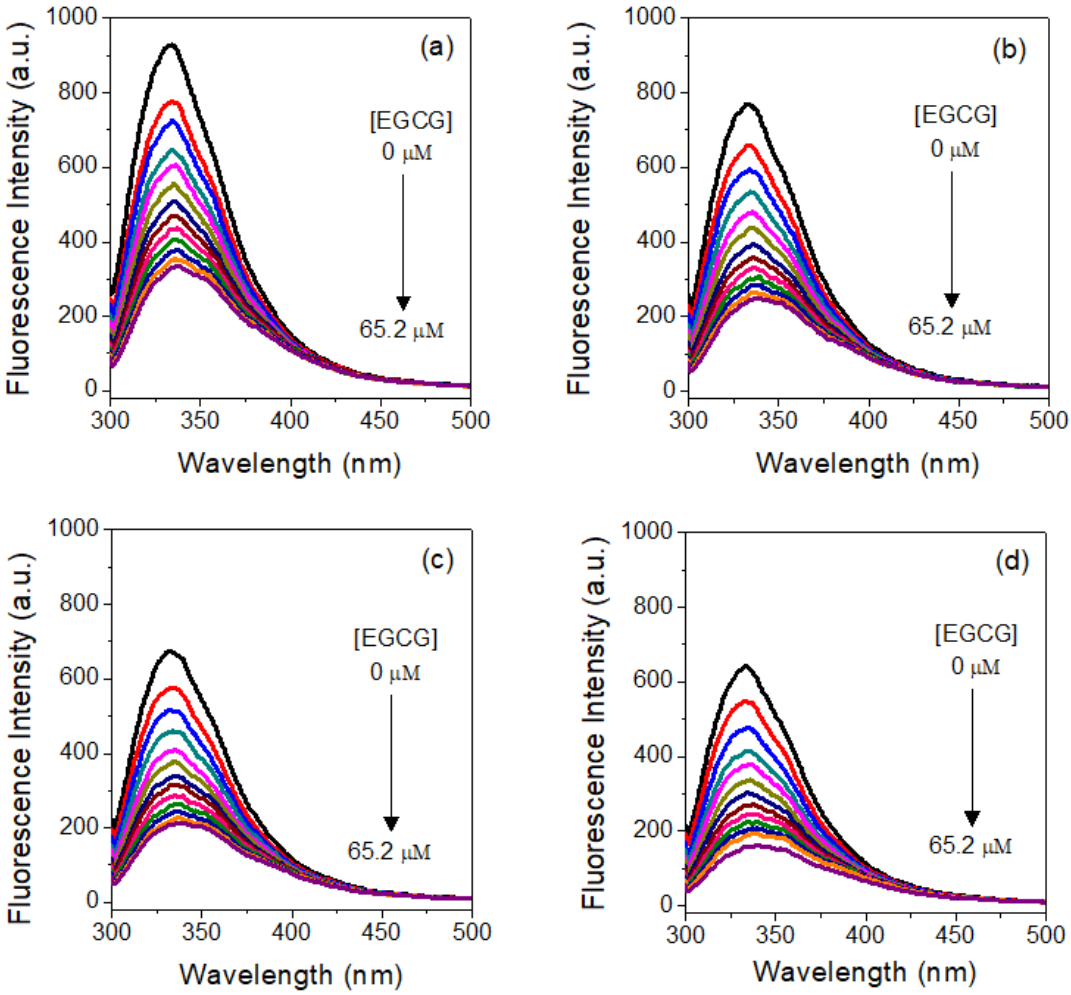

Fig. S3. Fluorescence spectra of bLF (2 μM) with increasing concentrations of EGCG, at following temperatures: (a) 20 °C, (b) 30 °C, (c) 35 °C, (d) 40 °C, and at pH 7.0. The arrow indicates increasing EGCG concentration from 0 to 65.2 μM (0, 6.2, 12.2, 18.1, 23.8, 29.4, 34.9, 40.2, 45.5, 50.6, 55.6, 60.4 and 65.2 μM).

ARTICLE 3

Human serum albumin-resveratrol complex formation: Effect of the phenolic chemical structure on the kinetic and thermodynamic parameters of the interactions

Article published in the journal *Food Chemistry*. doi: 10.1016/j.foodchem.2019.125514

Abstract

The thermodynamics and kinetics of binding between human serum albumin (HSA) and resveratrol (RES) or its analog (RESAn1) were investigated by surface plasmon resonance (SPR). The binding constant and the kinetic constants of association and dissociation indicated that RESAn1 has higher affinity toward HSA than does RES. The formation of these complexes was entropically driven ($T\Delta S^0{}_{HSA-RES} \cong 33.8$, $T\Delta S^0{}_{HSA-RESAn1} \cong 56.4$ KJ mol^{-1}). However, for both polyphenols, the activation energy (E_{act}) of association (a) of free molecules was higher than that for dissociation (d) of the stable complex ($E_{act(a)HSA-RES} = 11.37,\ E_{act(d)HSA-RES} = -3.06, E_{act(a)HSA-RESAn1} = 30.76,\ E_{act(d)HSA-RESAn1} = -5.24$ KJ mol^{-1}), and the rate of association was faster than that of dissociation since the activation Gibbs free energy ($\Delta G^{\ddagger}$) was lower for the former ($\Delta G^{\ddagger}_{aHSA-RES} \cong 54.73,\ \Delta G^{\ddagger}_{dHSA-RES} \cong 73.83, \Delta G^{\ddagger}_{aHSA-RESAn1} \cong 54.14, \Delta G^{\ddagger}_{dHSA-RESAn1} \cong 73.97$ KJ mol^{-1}). This study showed that small differences in the structure of polyphenols such as RES and RESAn1 influenced in the thermodynamics and kinetics of the complex formation with HSA.

Keywords: human serum albumin; resveratrol; resveratrol analogue; thermodynamic binding; kinetic constants; activated complex; comparative study

Chemical compounds studied in this article

Human serum albumin (PubChem CID: 72941834); resveratrol (PubChem CID: 445154)

1. Introduction

Resveratrol (RES, 3,5,4'-trihydroxystilbene, Fig. 1a) is a natural stilbenoid found in peanuts, dark chocolate, grapes, and wine; with red wine being the most notable source of RES in the human diet. This bioactive polyphenol exhibits many functional properties, including antioxidant, anti-inflammatory, neuro- and cardioprotective, anti-carcinogenic, anti-aging, anti-diabetic, and anti-obesity properties (Arcanjo, Luna, Madruga, & Estévez, 2018; Jannin et al., 2004; Lu et al., 2007).

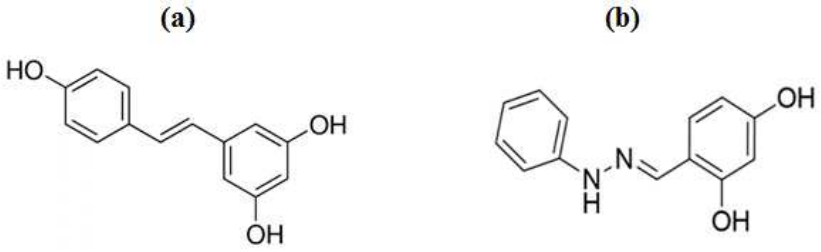

Fig. 1 Chemical structure of resveratrol **(a)** and its analog RESAn1 **(b)**.

The chemical stability of bioactive compounds is of great relevance to their corresponding biological activity. For instance, the observed functional activity of the RES degradation products is lower than that observed for the parent polyphenol. However, the use of RES in human therapeutic applications is quite limited because of its poor solubility in water (0.023 mg ml^{-1}), low oral bioavailability, and high chemical instability in aqueous media (tendency to suffer oxidation and high photosensitivity) (Fan, Liu, Gao, Zhang, & Yi, 2018; Pantusa, Bartucci, & Rizzuti, 2014). Therefore, significant efforts have been made toward the development of technologies that overcome these limitations.

To this end, researchers have synthesized various RES analogs (RESAn) with small changes in the RES structure aimed at improving their stability and/or functional properties (da Silva et al., 2018; Martins et al., 2018; Zimmermann-Franco et al., 2018). The RESAn 2,4-dihydroxybenzaldehyde phenylhydrazone (RESAn1, Fig. 1b) was produced by classic bioisosterism through substitution of the central C=C stilbenoid linkage by a C=N-NH hydrazone (da Silva et al., 2018).

In addition to the well-known biological properties of RES, RESAn1 also presents antileishmanial activity. It exhibited increased bioavailability due to its ability to cross biological membranes. This, coupled with its favorable gastrointestinal absorption, made it a promising drug candidate (da Silva et al., 2018). In addition, the anti-inflammatory and antioxidant properties of a series of RES analogs were improved compared to those of RES (Zimmermann-Franco et al., 2018). Therefore, it is of interest to develop delivery systems that stabilize RES and RESAn1 to preserve their biological and pharmacological activities during *in vivo* transit.

Human serum albumin (HSA), the most abundant protein in blood plasma, plays a dominant role in the transport and distribution of various endogenous and exogenous species, including polyphenols (Arcanjo et al., 2018; Pantusa et al., 2014). Jannin et al. (2004) evaluated the transport of RES to cellular targets and its cellular uptake. The authors found that HSA played a fundamental role in the distribution and bioavailability of RES in the bloodstream as well as the delivery of the compound to the cell surface, which is key in affecting its intracellular biological effect. Hence, HSA was considered a natural transporter of this polyphenol *in vivo*. HSA has also been found to protect RES from the degradative effects of radiation (Pantusa et al., 2014). The efficiency of a therapeutic substance is related to its affinity for binding to delivery proteins (Karimi et al., 2016).

Many studies have been done to investigate HSA-RES binding using fluorescence spectroscopy (FS); however, there have been discrepancies between the binding constants (K_b) obtained, which ranged from 9.1 x 10^4 to 4.5 x 10^6 L mol^{-1} (Arcanjo et al., 2018; Bourassa, Kanakis, Tarantilis, Pollissiou, & Tajmir-Riahi, 2010; Jiang, 2008; Lu et al., 2007; Mohos et al., 2018; N′ soukpoé-Kossi et al., 2006; Nair, 2015; Pantusa, Sportelli, & Bartucci, 2012; Tang et al., 2017; Wu et al., 2009). Although FS is widely used for interaction studies between proteins and small molecules, it presents some limitations, including the following: i) ability to detect interactions occurring only in regions near tryptophan residues (Bourassa et al., 2010; Hudson et al., 2018) and ii) RES can absorb light near the excitation and emission wavelengths used for FS experiments (Pantusa et al., 2014). These restrictions require additional care in data processing and interpretation.

SPR is a valuable and very sensitive technique for a real-time investigation of interactions between molecules because it is a label-free optical technique (Bahri, Henriquet, Pugnière, Marchesseau, & Chevalier-Lucia, 2019; Fathi, Mohammadzadeh-

Aghdash, Sohrabi, Dehghan, & Ezzati Nazhad Dolatabadi, 2018). Briefly, the general principle of this technique is based on the phenomenon of surface plasmon resonance. This phenomenon occurs when a polarized light beam is projected through a prism onto a thin metal film (gold in this case) and, at a specific angle of incidence, part of the incident radiation couples with the oscillating free electrons (plasmons) of the metal film. Thus, surface plasmon resonance can occur because of their matching frequencies. Due to the energy transfer that occurs during the resonance coupling, the intensity of the reflected light is reduced at the angle at which SPR is occurring. The resonance of the plasmons produces an evanescent wave that extends approximately 100 nm above the gold surface, changing the refractive index within this environment. This leads to a shift in the refraction angle where the intensity drop is observed. Therefore, when flow-through analyte (polyphenol) is injected into the sample channel, any binding of the analyte to the immobilized protein (HSA) will produce a small change in the refractive index of the gold surface. This change can be precisely quantified by a detector. This approach enables real-time measurement of biomolecular interactions wherein the changes in refractive index are proportional to complex formation (Bahri et al., 2019; Patching, 2014).

Therefore, in this study, we performed a complete kinetic and thermodynamic characterization of the interactions in HSA-RES and HSA-RESAn1 complexes using surface plasmon resonance (SPR).

2. Materials and methods

2.1 Materials

Solid standards of resveratrol (99%), and human serum albumin (96%) were purchased from Sigma-Aldrich (USA). The resveratrol analog 2,4-dihydroxybenzaldehyde phenylhydrazone (RESAn1) was synthesized according to da Silva et al. (2018). Dibasic sodium phosphate (Na_2HPO_4) and sodium phosphate monohydrate ($NaH_2PO_4 \cdot H_2O$) were purchased from Vetec (Brazil). CM5 sensor chips and coupling reagents [*N*-ethyl-*N*'-(dimethylaminopropyl)carbodiimide (EDC), *N*-hydroxysuccinimide (NHS) and ethanolamine hydrochloride] were purchased from GE Healthcare (USA). All chemicals and reagents used throughout the study were of analytical grade.

2.2 SPR analysis

SPR measurements were performed in triplicate using a Biacore X100 instrument (GE Healthcare, Pittsburgh, PA, USA). For this experiment, three CM5 sensor chips composed of carboxymethylated dextran covalently attached to a gold film were used. On the sensor chip surface were two flow channels: the sample channel (in which the protein will be immobilized) and the reference channel.

During the analysis, the response of the detector relates the dependency of the SPR signal (expressed in arbitrary Resonance Units (RU)) versus time (t) in graphs called sensorgrams, where one RU corresponds to 0.0001° shift in SPR angle. The output signal, or response, of the SPR is the difference of signals between the sample (with immobilized HSA) and reference (without immobilized HSA) channels.

2.2.1 Immobilization of HSA on the chip surface

Immobilization of HSA on the chip surface was performed according to an amino coupling protocol. First, the CM5 chip was activated by injecting a freshly prepared mixture of EDC (0.4 M) and NHS (0.1 M) (1:1 v/v) at a flow rate of 10 µl/min for 7 min. The HSA, at a concentration of 30 µg ml^{-1} in immobilization buffer (10 mM sodium acetate at pH 4.0), was injected into the sample channel and allowed to react for 7 min at a flow rate of 10 µl/min, resulting in a HSA immobilized densities averaging 3893 RU (RU values is proportional to actually bound HSA). The immobilization density applied in the present study was chosen in order to avoid the mass transport effect (de Paula et al., 2017). HSA was coupled to the chip surface in the sample channel through covalent bonding between its amine groups and the carboxyl groups of the CM5 sensor chip. The remaining carboxyl groups were blocked by injecting a solution of ethanolamine hydrochloride (1 M) at pH 8.5 for 7 min at a flow rate of 10 µL/min. The HSA was immobilized only in the sample channel of the sensor chip to allow for monitoring of possible non-specific interactions between the protein and the chip surface by means of the reference channel. The reference channel was activated with a 1:1 mixture of EDC/NHS and then treated with ethanolamine to block the carboxyl groups.

2.2.2 Analysis of RES and RESAn1 interactions with immobilized HSA

For the interaction experiments, the solutions of RES or RESAn1 were prepared in HBS-P buffer (0.01 M HEPES pH 7.4, 0.15 M NaCl, and 0.005% v/v surfactant P20) and DMSO (4%, v/v) immediately prior to analysis. To obtain the sensorgrams of the

interactions between the protein and the polyphenols, a range of polyphenol concentrations were analyzed: 100 to 220 µM (100, 120, 140, 160, 180, 200, and 220 µM) for RES and 70 to 130 µM (70, 80, 90, 100, 110, 120, and 130 µM) for RESAn1. The concentration range of polyphenols were chosen in order to obtain a linear relationship between observed rate constant (k_{obs}) and the amount of substance of polyphenols. The polyphenols were injected onto the HSA immobilized chip for 20 s at a flow rate of 10 µl/min. This flow rate was selected to avoid the mass effect, which occurs when the association of an analyte (polyphenols) to the ligand (protein) is limited by the diffusion of the analyte on the surface of the chip, i.e., when the diffusion rate is slower than the association rate. The experiments were carried out at six temperatures (12, 16, 20, 24, 25, and 28 °C). The HBS-P flowing buffer was injected twice for 30 s at a flow rate of 30 µl/min to regenerate the chip surface at the end of each experiment.

2.2.2.1. Kinetic study of HAS-polyphenol interaction

The entire data set were analyzed according to a one to one binding model, described by HSA + Pol ⇋ HSA-Pol.

In the data analysis, the integrated rate equations (Eqs. 1 and 2) were globally fitted to each sensorgram to determine the k_{obs} and the dissociation rate constant (k_d) while the association kinetic rate constant (k_a) was obtained through Eq. 3 (Rezende et al., 2019) (Fig. S1).

$$RU(t) = RU_{max}(t_\infty)[1 - e^{-k_{obs}(t)}] \quad \text{Eq. 1}$$

$$RU(t) = RU(t_m)\, e^{-k_d(t-t_m)} \quad \text{Eq. 2}$$

$$k_{obs} = k_a \cdot [Pol] + k_d \quad \text{Eq. 3}$$

where t_m is the time at which the descendant curve began, $RU(t)$ is the SPR response obtained in the sensorgram at time t, $RU_{\max}(t_\infty)$ is the SPR response when HSA is fully saturated by polyphenol, $RU(t_m)$ is the SPR response obtained in the sensorgram at time t_m, and $[Pol]$ is the concentration of RES or RESAn1.

Following the Transition State Theory" (TST) (Petersson, 2000; Privalov, 1996), the temperature dependence of the rate kinetic constants k_a and k_d was analyzed through

the Arrhenius equation (Eq. 4) to determine the activation energy required to form the activated complex from the association of free molecules ($E_{act(a)}$) and the dissociation of the thermodynamically stable complex ($E_{act(d)}$), respectively.

$$\ln k_x = lnA - \frac{E_{act(x)}}{RT} \quad \text{Eq. 4}$$

where k_x is the rate constant when $x = a$ or d (with the respective units of L mol^{-1} s^{-1} and s^{-1}) at temperature T (K), A is a pre-exponential factor, $E_{act(x)}$ is the corresponding activation energy (kJ mol^{-1}), and R is the universal gas constant (8.3145 J mol^{-1} K^{-1}) (Wang & Roberts, 2013).

The activation Gibbs free energy change ($\Delta G_x^{\ddagger}$) can be obtained from the Eyring equation (Eq. 5) (Wang & Roberts, 2013):

$$k_x = \frac{k_B T}{h} \exp\left(\frac{-\Delta G_x^{\ddagger}}{RT}\right) \quad \text{Eq. 5}$$

where k_B is the Boltzmann constant (1.38066 × 10^{-23} J K^{-1}) and h is Planck's constant (6.62608 × 10^{-34} J s) at temperature T (K).

The activation enthalpy change ($\Delta H_x^{\ddagger}$), and activation entropy change ($T\Delta S_x^{\ddagger}$) can be obtained through Eqs. 6 and 7 (Rezende et al., 2019), respectively, while the $\Delta C_{p(x)}^{\ddagger}$ values were calculated using the relationship in Eq. 8 (Nunes, de Paula, Coelho, da Silva, & Pires, 2019).

$$\Delta H_x^{\ddagger}(T) = E_{act(x)}(T) - RT \quad \text{Eq. 6}$$

$$T\Delta S_x^{\ddagger}(T) = \Delta H_x^{\ddagger}(T) - \Delta G_x^{\ddagger}(T) \quad \text{Eq. 7}$$

$$\Delta C_{p(x)}^{\ddagger} = \left(\frac{\partial(\Delta H_x^{\ddagger})}{\partial T}\right) \quad \text{Eq. 8}$$

2.2.2.2. Thermodynamic study of HAS-polyphenol interaction

The ratio between the kinetic rate constants yields the thermodynamic dissociation constant (K_D), as demonstrates the relationship: $K_D = {k_d}/{k_a}$. Since $K_D = {1}/{K_b}$, where K_b is the binding constant, the ΔG^0 was obtained from Eq. 9, the ΔH^0 was obtained from the Van't Hoff equation (Eq. 10, Fig. S2), and the entropic term ($T\Delta S^0$) was determined by the fundamental Gibbs relation (Eq. 11) (Hudson et al., 2018).

$$\Delta G^0 = -RTlnK_b \quad \text{Eq. 9}$$

$$ln\frac{K_{b2}}{K_{b1}} = -\frac{\Delta H^0}{R} \cdot \left(\frac{1}{T_2} - \frac{1}{T_1}\right) \quad \text{Eq. 10}$$

$$\Delta G^o = \Delta H^0 - T\Delta S^0 \quad \text{Eq. 11}$$

Here T is the temperature (K) and R is the universal gas constant (8.3145 J mol^{-1} K^{-1}).

All SPR experiments were performed in triplicate to ensure accuracy and the kinetic and thermodynamic results were expressed as the mean ± standard deviation, being the standard deviation between 2 and 6%.

3. Results and discussion

3.1 Kinetic analysis of RES and RESAn1 interactions with immobilized HSA

SPR was used to directly measure binding between an important transport protein, HSA, and two bioactive molecules with very similar chemical structures, RES and its analog RESAn1 (Fig. 1). In particular, one of the interacting molecules (RES or RESAn1) was dissolved in a mobile solution and made to flow over the immobilized HSA. To verify the possible influence of mass transfer, a low concentration of polyphenol was injected at different flow rates to observe their effects on the SPR response associated with polyphenol binding with the immobilized HSA (data not shown). These experiments demonstrated that the association and dissociation rates were independent of flow rate, therefore mass transfer was determined not to be an issue. Fig. 2 reports the sensorgrams obtained from the SPR kinetic experiments.

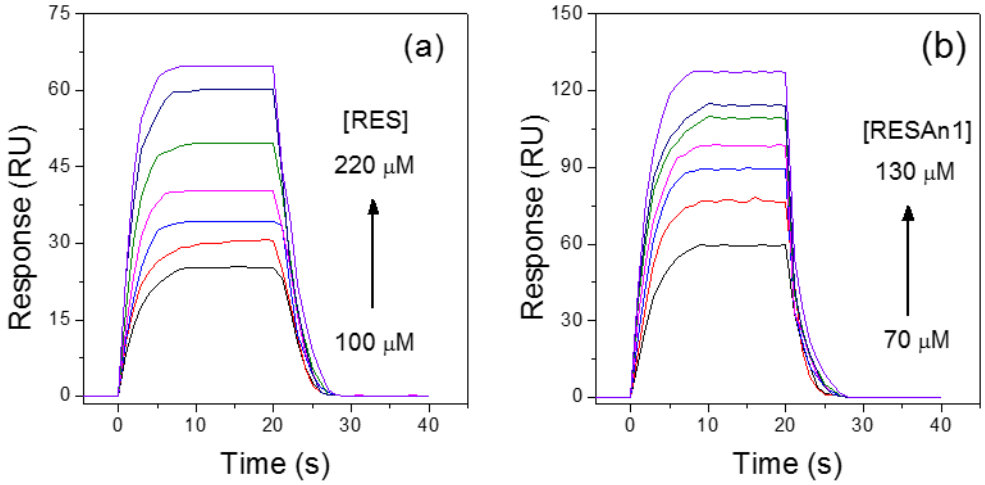

Fig. 2. Sensorgrams (Resonance units (RU) vs Time (s)) for (a) RES (100–220 µM) and (b) RESAn1 (70–130 µM) flowing over a CM5 low-density HSA-immobilized sensor-chip surface (3893 RU) at 25 °C. The arrows indicate increasing RES or RESAn1 concentration (sensorgrams obtained for other temperatures are showed in Fig. S3 for HSA-RES and Fig. S4 for HSA-RESAn1, Supporting Information).

Considering that RU is dependent on the refractive index of the environment above the surface of the chip (surface layer ≈ 100 nm), binding events, such as the association of molecules and/or dissociation of the complex, will lead to changes in this index. Therefore, we can consider that RU is directly related to complex formation between the polyphenol and the protein (He et al., 2017). The profiles of the sensorgrams were similar at all polyphenol concentrations. Two distinct regions (an ascendant and a descendant curve) were present in each sensorgram, corresponding to different binding events that occurred during the kinetic experiment.

A remarkable RU increase was noted in the 0 to 10 s interval, which can be attributed to the increase in the polyphenol concentration in proximity to the immobilized HSA in the sample channel, resulting in an increase in the interaction between polyphenol and protein (Rezende et al., 2019). This net change in RU signal is attributed to both the association of the reactants (RES or RESAn1 and HSA) and the dissociation of the formed complex; however, the association process predominates in this time range. However, between 10 and 20 s a plateau was reached, indicating that the association and dissociation speeds were equal (Hudson et al., 2019). After 20 s the RU signal decreased until it returned to the baseline. It should be kept in mind that after that time only buffer, lacking polyphenol, was flown over the immobilized HSA. The buffer could have thus removed

the polyphenol from HSA surface, resulting in the predominance of the dissociation process in the descendant region of the sensorgram.

The sensorgram data were fitted to Eq. 1-3 to obtain k_a and k_d values. The k_a value expresses the amount of HSA-polyphenol complex formed per second, while k_d is the percentage of complexes that dissociate per second. The k_a and k_d for both polyphenols interacting with HSA presented a linear behavior with temperature variation (Fig. 3).

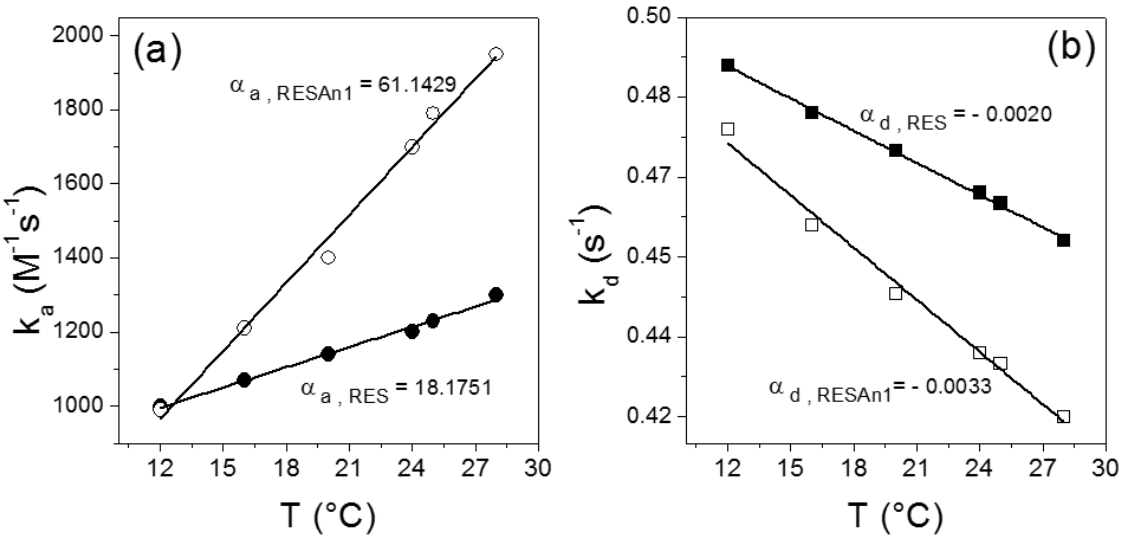

Fig 3. Rate constants for the (a) association (k_a) and (b) dissociation (k_d) of HSA-RES (closed symbol) and HSA-RESAn1 (open symbol) as a function of temperature. The black lines are the linear fitting for the curves, whose determination coefficients (R^2) were higher than 0.98 in all cases.

The increase in k_a and the decrease in k_d with the increase in temperature indicates that the higher the average molecular kinetic energy, the more frequent the association between free molecules and the less frequent the dissociation of the stable complex, i.e., the affinity between HSA and the polyphenols increased with an increase in temperature. However, the values of k_a for RESAn1 were higher than those obtained for RES, i.e., the rate for the association between free HSA and RESAn1 was faster as compared to that between HSA and RES. On the other hand, the k_d values of HSA-RESAn1 were smaller than those of HSA-RES at all temperatures. These results demonstrated that the addition of an NNH_2 functional group in the stilbenoid nucleus of RES to obtain RESAn1 (Fig. 1) contributed to an increase in its binding affinity for HSA.

3.2 Energetic parameters related to the activated complex formation

According to the general theory of the absolute rates of any chemical process, the speed of the steps occurring in this process are related to a molecular passage through a potential energy barrier (Eyring, 1935). Thus, the molecular dynamics probably proceed by a definite sequence of transition states with a decrease in Gibbs free energies, which is analyzed by TST. In the case of interactions between proteins and small molecules, the transition state is known as the activated (or intermediate) complex (de Paula et al., 2017). These activated complexes have a very unstable and short-lived nature, which prevents them from being observed directly (Arango-Restrepo, Rubi, & Barragán, 2018; Privalov, 1996); but the knowledge of the energetic parameters related to the association of free molecules and the dissociation of the thermodynamically stable complex to form the activated complexes yields important insight into the structure and the molecular dynamics of the formation of thermodynamically stable complexes (Shukla, Meng, Roux, & Pande, 2014).

Since $E_{act(x)}$ is temperature independent and constant over the range examined, Eq. 4 shows a linear relationship between $\ln k_x$ and the inverse of the absolute temperature. The Arrhenius equation is widely accepted to describe the influence of temperature on the rates of chemical processes, such as intermolecular interactions. The Arrhenius plot of the experimentally determined rate constants at varying temperatures (Fig. S5) yields a straight line with slope equal to $-\frac{E_{act(x)}}{R}$. This linearity reinforces that the potential energy barrier for the formation of the activated complex was temperature independent over the range of temperatures that were analyzed. Moreover, it indicates that the formation of the activated complex occurred in a simple single step process involving either the association of the free reactants or the dissociation of the thermodynamically stable complex (Wang & Roberts, 2013).

The $E_{act(a)}$ values were positive for both HSA-RES and HSA-RESAn1 ($E_{act(a),\ \mathrm{HSA-RES}}$ = +11.37 kJ mol^{-1} and $E_{act(a),\ \mathrm{HSA-RESAn1}}$ = +30.76 kJ mol^{-1}), however the latter was 2.7 times larger than the former. This result means that the polyphenol derivative (RESAn1) induced more conformational change (E_{conf} > 0) in the protein than RES, which can be associated with interactions occurring between the NNH_2 functional group of RESAn1 and amino acid residues of HSA. On the other hand, the $E_{act(d)}$ values

were negative ($E_{act(d),\ \mathrm{HSA-RES}}$ = −3.06 kJ mol^{-1} and $E_{act(d),\ \mathrm{HSA-RESAn1}}$ = −5.24 kJ mol^{-1}). These $E_{act(d)}$ values are derived from three main contributions: i) the energy of the conformational change required for HSA binding (E_{conf} > 0), ii) the solvating energy of HSA and polyphenol after the structural change to the stable complex (E_{sol} < 0), and iii) the energy resulting from intermolecular interactions between amino acid residues and polyphenols involved in the formation of the activated complex (E_{int} > 0) (Nunes et al., 2019). The negative $E_{act(d)}$ values are due to the relationship $|E_{conf} + E_{int}| < |E_{solv}|$, wherein the slightly more negative $E_{act(d),\ \mathrm{HSA-RESAn1}}$ value resulted from the greater energy released when the functional groups of RESAn1 are solvated.

The $\Delta G_x^{\ddagger}$ values were similar for the two polyphenols, both for the association and dissociation processes. Fig. 4a shows the relationship between $\Delta G_x^{\ddagger}$ and temperature, and in all cases, a positive linear relationship was observed.

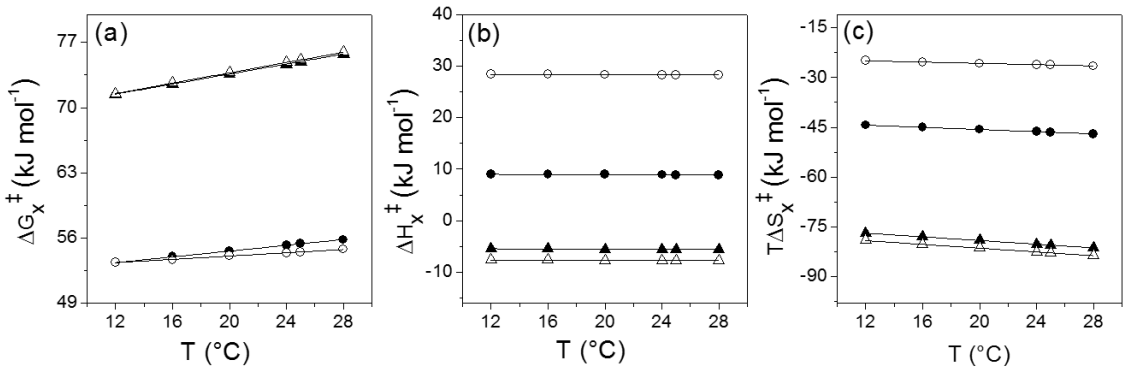

Fig 4. Energetic parameters for the formation of the activated complex between RES (closed symbol) or RESAn1 (open symbol) and HSA from the association of the free reagents (●, ○) or the dissociation of the stable complex (▲, Δ) at pH 7.4. (a) Activation Gibbs free energy change ($\Delta G_x^{\ddagger}$), (b) activation enthalpy change ($\Delta H_x^{\ddagger}$), (c) activation entropy change ($T\Delta S_x^{\ddagger}$). The black lines are the linear fitting, whose determination coefficients (R^2) were greater than 0.99 in all cases.

As $\Delta G_x^{\ddagger}$ is related to the rate of formation of the activated complex, these results demonstrated that the increase in the temperature yields slower formation of the activated complex between HSA and RES compared to that between HSA and RESAn1 ($\alpha_{\Delta G_a^{\ddagger}\ vs\ T,\ HSA-RES} = 0.1551$ and $\alpha_{\Delta G_a^{\ddagger}\ vs\ T,\ HSA-RESAn1} = 0.0876$). In contrast, the effect of increasing temperature on $\Delta G_x^{\ddagger}$ of the dissociation process was almost

independent of the polyphenols ($\alpha_{\Delta G_d^{\ddagger}\ vs\ T,\ HSA-RES} = 0.2688$ and $\alpha_{\Delta G_d^{\ddagger}\ vs\ T,\ HSA-RESAn1} = 0.2769$).

The formation of the activated complex from the association of the polyphenols with the HSA was found to occur faster than dissociation of the stable complex ($\Delta G_a^{\ddagger} < \Delta G_d^{\ddagger}$), although the energy barrier to the association was higher than that for the dissociation ($E_{act(a)} > E_{act(d)}$). These results could be correlated to the stability of the HSA-polyphenol complexes. Further knowledge regarding the enthalpic and entropic components of $\Delta G_x^{\ddagger}$ may contribute to elucidating the cause of this difference in association and dissociation parameters.

The activation enthalpy change ($\Delta H_x^{\ddagger}$), and activation entropy change ($T\Delta S_x^{\ddagger}$) are shown as a function of temperature in Figs. 4b and c, respectively. In addition to these parameters, the activation heat capacity change ($\Delta C_{p(x)}^{\ddagger}$) may also yield information about the magnitude of the intermolecular interactions, as well as the structural role and the reorganization of the solvent molecules involved in the formation of the activated complex (Perozzo, Folkers, & Scapozza, 2004). The $\Delta C_{p(x)}^{\ddagger}$ values were derived from the plots of $\Delta H_x^{\ddagger}$ versus T (Fig. 4b).

The enthalpic change in the association and dissociation processes were almost constant along the investigated temperature range (Fig. 4b). For the association process, the $\Delta H_a^{\ddagger}$ values were positive, while the energy cost for the association of HSA with RES was less than that for the association with RESAn1 ($\Delta H_{a,\ HSA-RES}^{\ddagger} \sim$ +9.0 kJ mol^{-1}, $\Delta H_{a,\ HSA-RESAn1}^{\ddagger} \sim$ +28.0 kJ mol^{-1}). In contrast, the stable complex dissociation was an enthalpically favored process, with similar $\Delta H_d^{\ddagger}$ values for both polyphenols ($\Delta H_{d,\ HSA-RES}^{\ddagger} \sim -5.0$ kJ mol^{-1}, $\Delta H_{d,\ HSA-RESAn1}^{\ddagger} \sim -7.0$ kJ mol^{-1}).

The formation of the activated complex was entropically unfavorable, independent of the process becoming more negative with the increase in the temperature (Fig. 4c). For the association process, the entropy was less negative for RESAn1 ($\alpha_{T\Delta S_a^{\ddagger}\ vs\ T,\ HSA-RESAn1} = -0.0960$) than for RES ($\alpha_{T\Delta S_a^{\ddagger}\ vs\ T,\ HSA-RES} = -0.1638$), while the dissociation values were similar for both molecules ($\alpha_{T\Delta S_d^{\ddagger}\ vs\ T,\ HSA-RES} = -0.2771$ and $\alpha_{T\Delta S_d^{\ddagger}\ vs\ T,\ HSA-RESAn1} = -0.2851$).

Therefore, the lower $\Delta G_a^{\ddagger}$ values ($\Delta G_{a,\ HSA-RES\ or\ HSA-RESAn1}^{\ddagger}$ ~ +55 kJ mol^{-1}) resulted from the positive enthalpy change and the negative entropy change, whose magnitude was lower than that of the reported dissociation process. On the other hand, although the $\Delta H_d^{\ddagger}$ values were negative for both polyphenols, the entropy change showed a large negative value, which was the cause of the high positive value of $\Delta G_d^{\ddagger}$ ($\Delta G_{d,\ HSA-RES\ or\ HSA-RESAn1}^{\ddagger}$ ~ +74 kJ mol^{-1}). This means that the formation of the thermodynamically stable complex from the activated complex occurs through a large increase in entropy (~ +80 kJ mol^{-1}), probably due to the increase in the degrees of freedom of the water molecules released from the solvation layers of the interaction site of the activated complex (de Paula et al., 2017).

Given that the relationship between $\Delta H_x^{\ddagger}$ and temperature were similar for both processes, consequently the $\Delta C_{p(x)}^{\ddagger}$ values were identical (~ -0.0083 kJ K^{-1} mol^{-1}) for both polyphenols and both formation processes (association and dissociation) (Fig. 4b). The $\Delta C_{p(a)}^{\ddagger}$ value corresponds to the difference between the $C_p^{\ddagger}$ of the HSA-polyphenol activated complex ($C_{p,\ HSA-Pol}^{\ddagger}$) and the C_P of the free reagents ($C_{P,\ HSA} + C_{P,\ Pol}$) (Nunes et al., 2019). Analogously, $\Delta C_{p(d)}^{\ddagger}$ refers to the difference between $C_{p,\ HSA-Pol}^{\ddagger}$ and the C_P of the stable HSA-polyphenol complex ($C_{P,\ stable\ HSA-Pol}$). This means that the energy transferred in the form of heat to potential energy components, responsible for the intermolecular interactions, is very similar among the three analyzed systems (free reagents, activated complex, and stable complex).

3.3 Thermodynamic study by SPR

The stability of the HSA-polyphenol complex and therefore its safe transport through blood depends on both the kinetics and the thermodynamics of complex formation. Polyphenol molecules, such as RES and RESAn1, are either bound to plasma proteins (HSA) or exist in an unbound (free) form in the circulatory system. The distribution, free concentration, and metabolism of polyphenols can be significantly altered as a result of their binding to HSA (Mohos et al., 2018; Schmidt, Gonzalez, & Derendorf, 2010; Shen et al., 2013). Therefore, knowing thermodynamic parameters, such as the dissociation constant (K_D), of the HSA-polyphenol complex is useful for the therapeutic application of these molecules, as well as for their pharmacokinetic and pharmacodynamic evaluation. The thermodynamic K_D yields a characterization of

polyphenol-protein interactions. Fig. 5 shows that the K_D values decreased linearly with the increase in temperature, wherein the decrease for HSA-RESAn1 was higher than for HSA-RES.

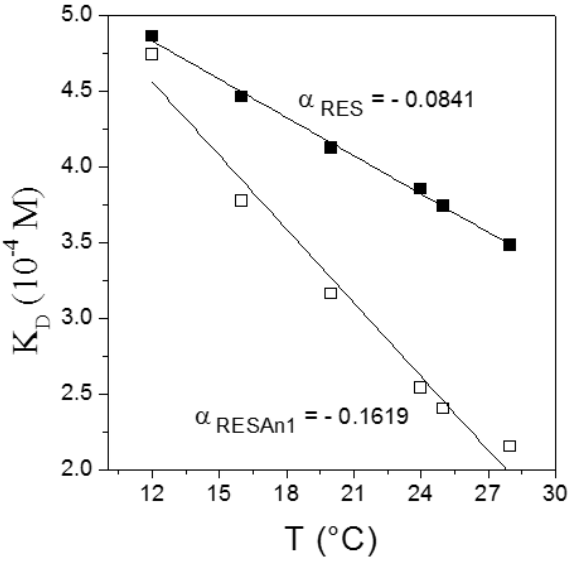

Fig. 5. The dissociation constant (K_D) for the HSA-RES (closed symbol) and HSA-RESAn1 (open symbol) complexes as a function of temperature. The black lines are the linear fitting, whose determination coefficients (R^2) were higher than 0.97 in all cases.

Temperature was an important parameter that affected the binding process; for example, an increase of 16 ºC reduced the K_D value by half for the HSA-RESAn1 complex (4.74 x 10^{-4} M to 2.15 x 10^{-4} M). This indicates that higher temperatures favor the stability of the HSA-polyphenol complex formed, especially in the case of the HSA-RESAn1 complex, since low K_D values indicate that the molecules have a greater tendency to remain complexed rather than in the free form (Taghipour, Zakariazadeh, Sharifi, Dolatabadi, & Barzegar, 2018).

Studies using FS techniques reported K_D values on the order of 10^{-6} M for the HSA-RES complexes at pH 7.0–7.4 and 25 °C (from 1.34 x 10^{-6} to 10.9 x 10^{-6} M) (Arcanjo et al., 2018; Bourassa et al., 2010; Jiang, 2008; Lu et al., 2007; Mohos et al., 2018; N′ soukpoé-Kossi et al., 2006; Pantusa et al., 2012; Tang et al., 2017; Wu et al., 2009). These results show values about 100-fold smaller than the K_D derived from our SPR experiments (Fig. 5).

Lelis et al. (2017) studied the binding of bovine serum albumin (BSA) and Ponceau4R dye and obtained K_D values on the order of 10^{-4} and 10^{-6} M by SPR and FS, respectively. Recently, Hudson et al. (2018) observed the same discrepancy in K_D values for a BSA-curcumin complex using both of these techniques. Our findings obtained by SPR presented a similar difference in magnitude when compared to fluorometric K_D values reported in the literature. Bahri et al. (2019) also obtained smaller K_D values for FS than for SPR for a β-casein-curcumin complex. It is known that the FS technique only evaluates binding sites around fluorescent amino acid residues, such as tryptophan (Trp). Therefore, the discrepancy in the results is probably related to the presence of other binding sites in HSA for the polyphenols, apart from Trp. When these other HSA binding sites participate in the interaction process, it leads to variation in the refractive index at the protein/solution interface and thus they modulate the K_D values more than the sites near Trp residues would on their own (Hudson et al., 2018; Lelis et al., 2017).

The binding of polyphenols to HSA aids their transport through blood and facilitates their delivery to the cell surface. However, the binding affinity should not be too high so as to allow the transfer of RES to the cellular interior (Latruffe, Menzel, Delmas, Buchet, & Lançon, 2014). Therefore, an understanding of the thermodynamic binding parameters, including the molecular forces that govern complex formation, such as the standard Gibbs free energy change (ΔG^0), standard enthalpy change (ΔH^0), and standard entropy change (ΔS^0), is essential to the successful application of these complexes. These thermodynamic binding parameters, at each temperature, are shown in Table 1.

The ΔG^o values were negative at all temperatures, which means that at thermodynamic equilibrium, the formation of the HSA-polyphenol complex is favored relative to the free reactants (HSA + Pol ⇋ HSA-Pol). In addition, the ΔG^o values decreased with an increase in temperature, and the formation of the HSA-RESAn1 complex was more favorable than that of the HSA-RES complex ($\Delta G^o_{HSA-RESAn1} < \Delta G^o_{HSA-RES}$) at all temperatures. Both the enthalpic and entropic components presented positive values indicating that the formation of the complexes was an endothermically and entropically driven process. Although the complex formation was driven by the hydrophobic effect for both polyphenols, the ΔH^o and $T\Delta S^o$ values showed different magnitudes. Therefore, the analysis of these parameters may contribute to explaining why HSA has a higher affinity for RESAn1.

Table 1. Thermodynamic parameters of interaction between HSA and RES or RESAn1 at pH 7.4 at different temperatures.

T (°C)	HSA-RES			HSA-RESAn1		
	ΔH° *	ΔG° *	TΔS° *	ΔH° *	ΔG° *	TΔS° *
12	14.43	-18.09	32.52	36.00	-18.12	54.12
16		-18.55	32.99		-18.96	54.96
20		-19.00	33.43		-19.64	55.64
24		-19.42	33.86		-20.45	56.45
25		-19.56	33.99		-20.65	56.65
28		-19.93	34.37		-21.14	57.14

* kJ mol^{-1}, for all parameters, the standard deviations were less than 3%.

Enthalpy is a measure of the total energy of a thermodynamic system and, for a binding process, ΔH^o reflects the energy change of the system when 1 mole of a small molecule binds to a protein. Therefore, considering the formation of the HSA-polyphenol complex, the ΔH^o values can be influenced by the following molecular processes: i) formation and disruption of non-covalent bonds, such as hydrogen and ionic bonds, and van der Waals interactions between the protein and the polyphenol ($\Delta H^o{}_{HSA-Pol} < 0$ for formation and $\Delta H^o{}_{HSA-Pol} > 0$ for disruption); ii) desolvation of the surface of the protein and polyphenol molecules ($\Delta H^o{}_{des-HSA} > 0$ and $\Delta H^o{}_{des-Pol} > 0$); and iii) interaction between water molecules released from the desolvation of both reactants ($\Delta H^o{}_{H_2O-H_2O} < 0$). Thus, the ΔH^o of the complex formation process is a global property resulting from the system as a whole, including favorable and unfavorable contributions not only from the solute, but also from the solvent.

The ΔH^o found for HSA-RESAn1 was higher than for HSA-RES (Table 1). We suggest that this difference was caused by the higher energy cost related to the $\Delta H^o{}_{des-Pol}$ term, owing to the desolvation of the stilbenoid nucleus present in the RESAn1 structure. Thus, the NNH_2 functional group is available to interact with HSA, contributing to an increased binding affinity.

Consequently, a greater number of water molecules are released during the formation of the HSA-RESAn1 complex leading to an increase in the overall entropy of the system. The values obtained for $T\Delta S^o$ ($T\Delta S^o{}_{HSA-RESAn1} > T\Delta S^o{}_{HSA-RES}$) corroborate this hypothesis, and in addition, their positive values indicate that hydrophobic interactions played an important role in the interaction between HSA and polyphenols. Wu et al. (2009) and Lu et al. (2007) also found that hydrophobic forces were the main drivers for complex formation between HSA and RES. Furthermore, RES exhibits a higher polarity than RESAn1 due to the presence of an additional OH group in its structure (Fig. 1). This greater polarity may have weakened its ability to penetrate into the inner hydrophobic regions of HSA.

Cao et al. (2016) evaluated the structure-affinity relationship of the binding of RES-derived stilbenoids to HSA through high performance affinity chromatography (HPAC) analysis. The affinity between pinostilbene and HSA was higher than that of RES and HSA. Pinostilbene is a simple hydrophobic derivative of RES whose only structural difference is the substitution of one of the three OH groups present in the parent RES by an OCH3 group (RES: 3,5,4′-OH; pinostilbene: 3,4′-OH,5-OCH_3). These results are in agreement with the theory proposed through our experimentation given that the structure of the RESAn1 analog studied here also shows greater hydrophobicity than RES.

4. Conclusion

SPR measurements implied that RES and RESAn1 interact with HSA resulting in the formation of thermodynamically stable HSA-polyphenol complexes in an aqueous media at pH 7.4. The formation of these complexes was driven by the increase in entropy in the system; also, the increase in temperature favored the stability of the complexes, regardless of the polyphenol. The results demonstrated that the binding affinity toward HSA was higher for RESAn1 than for RES. This was attributed to the lower polarity of RESAn1 as compared to RES, which can favor its penetration into the hydrophobic regions buried within HSA.

The association rate between HSA and RESAn1 was faster than that between HSA and RES. Moreover, the number of HSA-RESAn1 complexes dissociated per second was lower compared to that of HSA-RES complexes, reinforcing the hypothesis of a higher affinity of RESAn1 for HSA as compared to RES.

HSA-RES and HSA-RESAn1 complex formation occurred through the formation of activated complexes, which were less stable than free molecules and the thermodynamically stable HSA-polyphenol complexes. In both cases, the formation of these activated complexes from the association of the polyphenols and HSA occurred faster than the dissociation of the stable complexes.

The overall thermodynamic and kinetic analysis yielded a complete characterization of the energy and dynamics of formation of a complex between an important transport protein, namely HSA, and RES and RESAn1, representing two bioactive molecules.

Acknowledgements

The authors wish to thank the Conselho Nacional de Desenvolvimento Científico e Tecnológico (CNPq); the Coordenação de Aperfeiçoamento de Pessoal de Nível Superior (CAPES); CAPES/Pró-Forenses, the Fundação de Amparo à Pesquisa do Estado de Minas Gerais (FAPEMIG), the Financiadora de Estudos e Projetos (FINEP), and the Instituto Nacional de Ciências e Tecnologias Analíticas Avançadas (INCTAA) for their financial support.

Competing interests

The authors have declared that no competing interests exist.

References

Arango-Restrepo, A., Rubi, J. M., & Barragán, D. (2018). Kinetics and energetics of chemical reactions through intermediate states. *Physica A: Statistical Mechanics and Its Applications*, *509*, 86–96. https://doi.org/10.1016/j.physa.2018.05.132

Arcanjo, N. M. O., Luna, C., Madruga, M. S., & Estévez, M. (2018). Antioxidant and pro-oxidant actions of resveratrol on human serum albumin in the presence of toxic diabetes metabolites: Glyoxal and methyl-glyoxal. *Biochimica et Biophysica Acta (BBA) - General Subjects*, *1862*(9), 1938–1947. https://doi.org/10.1016/j.bbagen.2018.06.007

Bahri, A., Henriquet, C., Pugnière, M., Marchesseau, S., & Chevalier-Lucia, D. (2019). Binding analysis between monomeric β-casein and hydrophobic bioactive compounds investigated by surface plasmon resonance and fluorescence spectroscopy. *Food*

Chemistry, *286*, 289–296. https://doi.org/10.1016/J.FOODCHEM.2019.01.176

Bourassa, P., Kanakis, C. D., Tarantilis, P., Pollissiou, M. G., & Tajmir-Riahi, H. A. (2010). Resveratrol, Genistein, and Curcumin Bind Bovine Serum Albumin †. *The Journal of Physical Chemistry B*, *114*(9), 3348–3354. https://doi.org/10.1021/jp9115996

Cao, H., Jia, X., Shi, J., Xiao, J., & Chen, X. (2016). Non-covalent interaction between dietary stilbenoids and human serum albumin: Structure–affinity relationship, and its influence on the stability, free radical scavenging activity and cell uptake of stilbenoids. *Food Chemistry*, *202*, 383–388. https://doi.org/10.1016/j.foodchem.2016.02.003

da Silva, A. D., dos Santos, J. A., Machado, P. A., Alves, L. A., Laque, L. C., de Souza, V. C., … Capriles, P. V. S. Z. (2018). Insights about resveratrol analogues against trypanothione reductase of Leishmania braziliensis : molecular modeling, computational docking and in vitro antileishmanial studies. *Journal of Biomolecular Structure and Dynamics*, 1–34. https://doi.org/10.1080/07391102.2018.1502096

de Paula, H. M. C., Coelho, Y. L., Agudelo, A. J. P., Rezende, J. de P., Ferreira, G. M. D., Ferreira, G. M. D., … da Silva, L. H. M. (2017). Kinetics and thermodynamics of bovine serum albumin interactions with Congo red dye. *Colloids and Surfaces B: Biointerfaces*, *159*, 737–742. https://doi.org/10.1016/j.colsurfb.2017.08.036

Eyring, H. (1935). The Activated Complex and the Absolute Rate of Chemical Reactions. *Chemical Reviews*, *17*(1), 65–77. https://doi.org/10.1021/cr60056a006

Fan, Y., Liu, Y., Gao, L., Zhang, Y., & Yi, J. (2018). Improved chemical stability and cellular antioxidant activity of resveratrol in zein nanoparticle with bovine serum albumin-caffeic acid conjugate. *Food Chemistry*, *261*, 283–291. https://doi.org/10.1016/J.FOODCHEM.2018.04.055

Fathi, F., Mohammadzadeh-Aghdash, H., Sohrabi, Y., Dehghan, P., & Dolatabadi, J. E. N. (2018). Kinetic and thermodynamic studies of bovine serum albumin interaction with ascorbyl palmitate and ascorbyl stearate food additives using surface plasmon resonance. *Food Chemistry*, *246*, 228–232. https://doi.org/10.1016/j.foodchem.2017.11.023

He, J., Li, S., Xu, K., Tang, B., Yang, H., Wang, Q., & Li, H. (2017). Binding properties of the natural red dye carthamin with human serum albumin: Surface plasmon

resonance, isothermal titration microcalorimetry, and molecular docking analysis. *Food Chemistry*, *221*, 650–656. https://doi.org/10.1016/j.foodchem.2016.11.124

Hudson, E. A., de Paula, H. M. C., Ferreira, G. M. D., Ferreira, G. M. D., Hespanhol, M. do C., da Silva, L. H. M., & Pires, A. C. dos S. (2018). Thermodynamic and kinetic analyses of curcumin and bovine serum albumin binding. *Food Chemistry*, *242*, 505–512. https://doi.org/10.1016/j.foodchem.2017.09.092

Hudson, E. A., Rezende, J. de P., de Paula, H. M. C., Coelho, Y. L., da Silva, L. H. M., & Pires, A. C. dos S. (2019). Energetic parameters of β-casein/quercetin activated and thermodynamically stable complex formation accessed by Surface Plasmon Resonance. *Colloids and Surfaces B: Biointerfaces*, *181*, 798–805. https://doi.org/10.1016/J.COLSURFB.2019.06.048

Jannin, B., Menzel, M., Berlot, J.-P., Delmas, D., Lançon, A., & Latruffe, N. (2004). Transport of resveratrol, a cancer chemopreventive agent, to cellular targets: plasmatic protein binding and cell uptake. *Biochemical Pharmacology*, *68*(6), 1113–1118. https://doi.org/10.1016/j.bcp.2004.04.028

Jiang, Y. L. (2008). Design, synthesis and spectroscopic studies of resveratrol aliphatic acid ligands of human serum albumin. *Bioorganic & Medicinal Chemistry*, *16*(12), 6406–6414. https://doi.org/10.1016/j.bmc.2008.05.002

Karimi, M., Bahrami, S., Ravari, S. B., Zangabad, P. S., Mirshekari, H., Bozorgomid, M., … Hamblin, M. R. (2016). Albumin nanostructures as advanced drug delivery systems. *Expert Opinion on Drug Delivery*, *13*(11), 1609–1623. https://doi.org/10.1080/17425247.2016.1193149

Latruffe, N., Menzel, M., Delmas, D., Buchet, R., & Lançon, A. (2014). Compared Binding Properties between Resveratrol and Other Polyphenols to Plasmatic Albumin: Consequences for the Health Protecting Effect of Dietary Plant Microcomponents. *Molecules*, *19*(11), 17066–17077. https://doi.org/10.3390/molecules191117066

Lelis, C. A., Ferreira, G. M. D., Ferreira, G. M. D., Hespanhol, M. do C., Pinto, M. S., da Silva, L. H. M., & Pires, A. C. dos S. (2017). Determination of driving forces for bovine serum albumin-Ponceau4R binding using surface plasmon resonance and fluorescence spectroscopy: A comparative study. *Food Hydrocolloids*, *70*, 29–35. https://doi.org/10.1016/J.FOODHYD.2017.03.027

Lu, Z., Zhang, Y., Liu, H., Yuan, J., Zheng, Z., & Zou, G. (2007). Transport of a Cancer

Chemopreventive Polyphenol, Resveratrol: Interaction with Serum Albumin and Hemoglobin. *Journal of Fluorescence*, *17*(5), 580–587. https://doi.org/10.1007/s10895-007-0220-2

Martins, F. J., Senra, M., Caneschi, C. A., Santos, J. A. dos, da Silva, A. D., & Raposo, N. R. B. (2018). New group of azastilbene analogs of resveratrol: Synthesis, anticandidal activity and toxicity evaluation. *Journal of King Saud University - Science*. https://doi.org/10.1016/J.JKSUS.2018.02.003

Mohos, V., Bencsik, T., Boda, G., Fliszár-Nyúl, E., Lemli, B., Kunsági-Máté, S., & Poór, M. (2018). Interactions of casticin, ipriflavone, and resveratrol with serum albumin and their inhibitory effects on CYP2C9 and CYP3A4 enzymes. *Biomedicine & Pharmacotherapy*, *107*, 777–784. https://doi.org/10.1016/j.biopha.2018.08.068

N′ soukpoé-Kossi, C. N., St-Louis, C., Beauregard, M., Subirade, M., Carpentier, R., Hotchandani, S., & Tajmir-Riahi, H. A. (2006). Resveratrol Binding to Human Serum Albumin. *Journal of Biomolecular Structure and Dynamics*, *24*(3), 277–283. https://doi.org/10.1080/07391102.2006.10507120

Nair, M. S. (2015). Spectroscopic study on the interaction of resveratrol and pterostilbene with human serum albumin. *Journal of Photochemistry and Photobiology B: Biology*, *149*, 58–67. https://doi.org/10.1016/j.jphotobiol.2015.05.001

Nunes, N. M., de Paula, H. M. C., Coelho, Y. L., da Silva, L. H. M., & Pires, A. C. S. (2019). Surface plasmon resonance study of interaction between lactoferrin and naringin. *Food Chemistry*, *297*, 125022. https://doi.org/10.1016/J.FOODCHEM.2019.125022

Pantusa, M., Bartucci, R., & Rizzuti, B. (2014). Stability of trans -Resveratrol Associated with Transport Proteins. *Journal of Agricultural and Food Chemistry*, *62*(19), 4384–4391. https://doi.org/10.1021/jf405584a

Pantusa, M., Sportelli, L., & Bartucci, R. (2012). Influence of stearic acids on resveratrol-HSA interaction. *European Biophysics Journal*, *41*(11), 969–977. https://doi.org/10.1007/s00249-012-0856-y

Patching, S. G. (2014). Surface plasmon resonance spectroscopy for characterisation of membrane protein–ligand interactions and its potential for drug discovery. *Biochimica et Biophysica Acta (BBA) - Biomembranes*, *1838*(1), 43–55. https://doi.org/10.1016/j.bbamem.2013.04.028

Perozzo, R., Folkers, G., & Scapozza, L. (2004). Thermodynamics of protein-ligand interactions: history, presence, and future aspects. *Journal of Receptor and Signal Transduction Research*, *24*(1-2), 1–52. https://doi.org/10.1081/RRS-120037896

Petersson, G. A. (2000). Perspective on "The activated complex in chemical reactions." *Theoretical Chemistry Accounts: Theory, Computation, and Modeling (Theoretica Chimica Acta)*, *103*(3-4), 190–195. https://doi.org/10.1007/s002149900102

Privalov, P. L. (1996). Intermediate States in Protein Folding. *Journal of Molecular Biology*, *258*(5), 707–725. https://doi.org/10.1006/jmbi.1996.0280

Rezende, J. de P., Hudson, E. A., de Paula, H. M. C., Coelho, Y. L., da Silva, L. H. M., & Pires, A. C. dos S. (2019). Thermodynamic and kinetic study of epigallocatechin-3-gallate-bovine lactoferrin complex formation determined by surface plasmon resonance (SPR): A comparative study with fluorescence spectroscopy. *Food Hydrocolloids*, *95*, 526–532. https://doi.org/10.1016/j.foodhyd.2019.04.065

Schmidt, S., Gonzalez, D., & Derendorf, H. (2010). Significance of Protein Binding in Pharmacokinetics and Pharmacodynamics. *Journal of Pharmaceutical Sciences*, *99*(3), 1107–1122. https://doi.org/10.1002/jps.21916

Shen, Q., Wang, L., Zhou, H., Jiang, H., Yu, L., & Zeng, S. (2013). Stereoselective binding of chiral drugs to plasma proteins. *Acta Pharmacologica Sinica*, *34*(8), 998–1006. https://doi.org/10.1038/aps.2013.78

Shukla, D., Meng, Y., Roux, B., & Pande, V. S. (2014). Activation pathway of Src kinase reveals intermediate states as targets for drug design. *Nature Communications*, *5*(1), 3397. https://doi.org/10.1038/ncomms4397

Taghipour, P., Zakariazadeh, M., Sharifi, M., Dolatabadi, J. E. N., & Barzegar, A. (2018). Bovine serum albumin binding study to erlotinib using surface plasmon resonance and molecular docking methods. *Journal of Photochemistry and Photobiology B: Biology*, *183*, 11–15. https://doi.org/10.1016/j.jphotobiol.2018.04.008

Tang, F., Xie, Y., Cao, H., Yang, H., Chen, X., & Xiao, J. (2017). Fetal bovine serum influences the stability and bioactivity of resveratrol analogues: A polyphenol-protein interaction approach. *Food Chemistry*, *219*, 321–328. https://doi.org/10.1016/J.FOODCHEM.2016.09.154

Wang, W., & Roberts, C. J. (2013). Non-Arrhenius Protein Aggregation. *The AAPS Journal*, *15*(3), 840–851. https://doi.org/10.1208/s12248-013-9485-3

Wu, Q.-H., Zhou, X., Zang, X.-H., Wang, C., Zhang, Z.-H., & Wang, Z. (2009). Spectroscopic study on the interaction between resveratrol and human serum albumin. *Guang Pu Xue Yu Guang Pu Fen Xi = Guang Pu*, *29*(1), 226–30. http://www.ncbi.nlm.nih.gov/pubmed/19385245

Zimmermann-Franco, D. C., Esteves, B., Lacerda, L. M., Souza, I. de O., Santos, J. A. dos, Pinto, N. de C. C., … Macedo, G. C. (2018). In vitro and in vivo anti-inflammatory properties of imine resveratrol analogues. *Bioorganic & Medicinal Chemistry*, *26*(17), 4898–4906. https://doi.org/10.1016/j.bmc.2018.08.029

Supporting Information

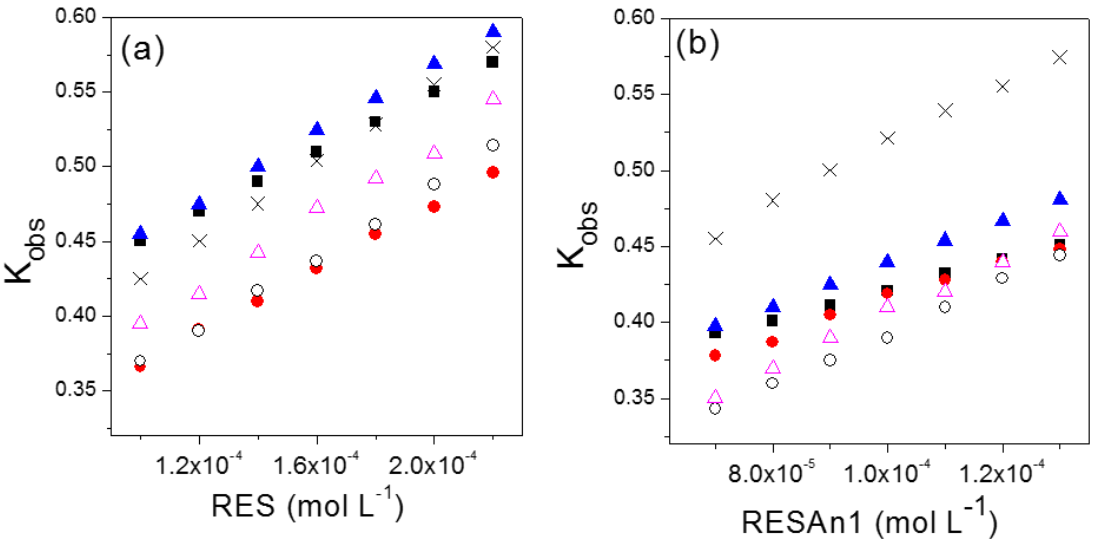

Figure S1. The plot of k_{obs} as a function of polyphenol concentration used to determine k_a at temperatures: (■) 12 °C, (●) 16 °C, (▲) 20 °C, (○) 24 °C, (△) 25 °C and (X) 28 °C. (a) HSA-RES, and (b) HSA-RESAn1. The linear fitting show determination coefficients (R^2)>0.98 in all cases.

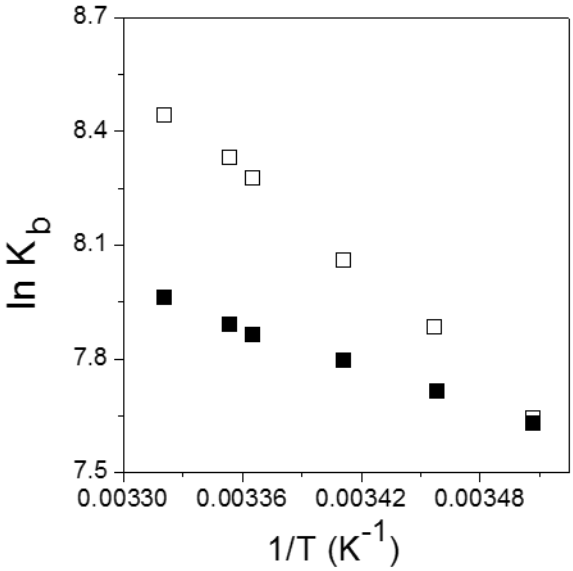

Figure S2. ln K_b associated interactions as functions of reciprocal temperature. (■) HSA-RES or (□) HSA-RESAn1

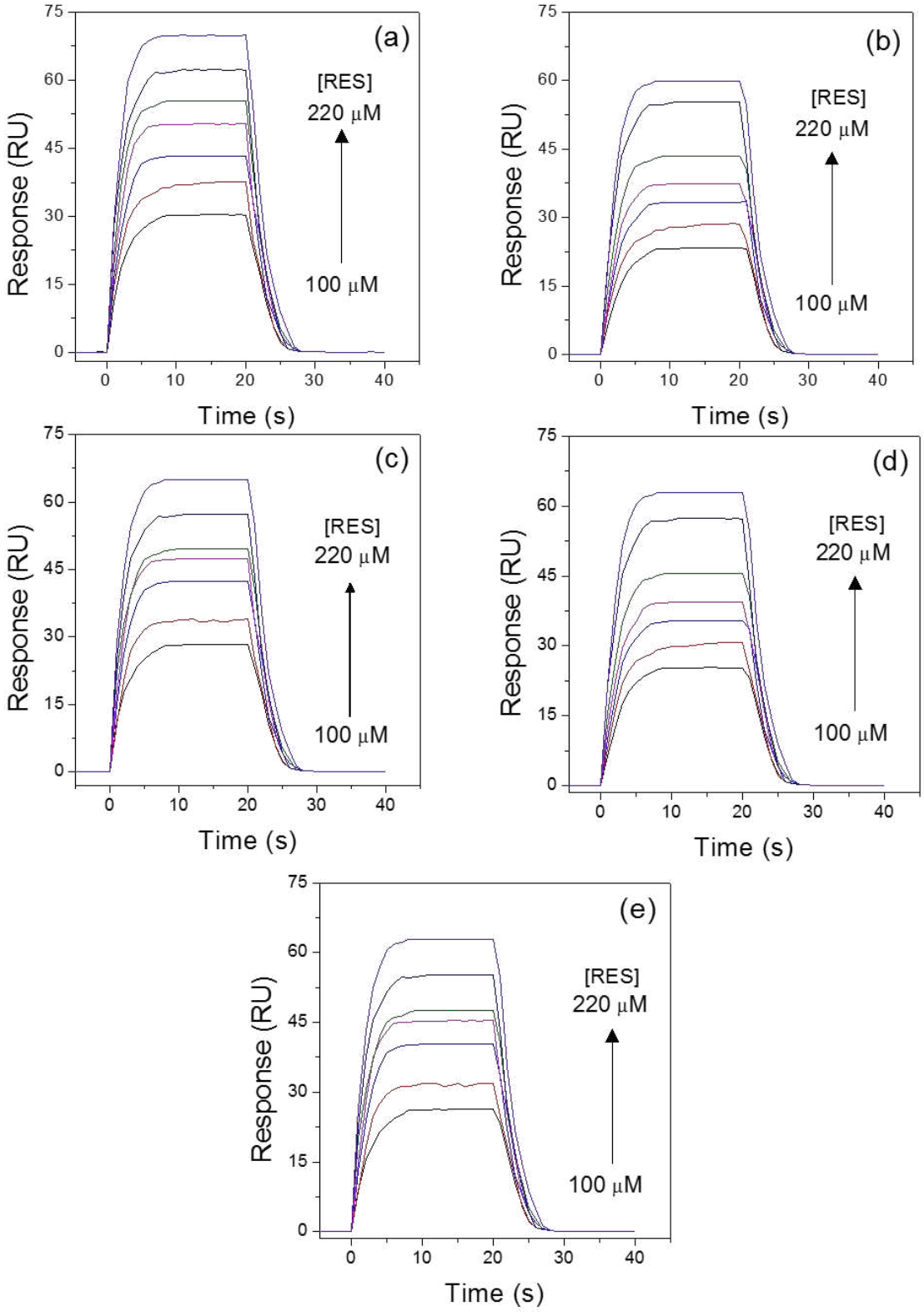

Fig S3. Sensorgrams (Resonance units - RU vs. Time) for HSA-RES, 100-220 µM RES solutions flowing over a CM5 low-density HSA-immobilized sensor-chip surface (3893 RU), at (a) 12 °C, (b) 16 °C, (c) 20 °C, (d) 24 °C and, (e) 28 °C. The arrows indicate increasing RES concentration.

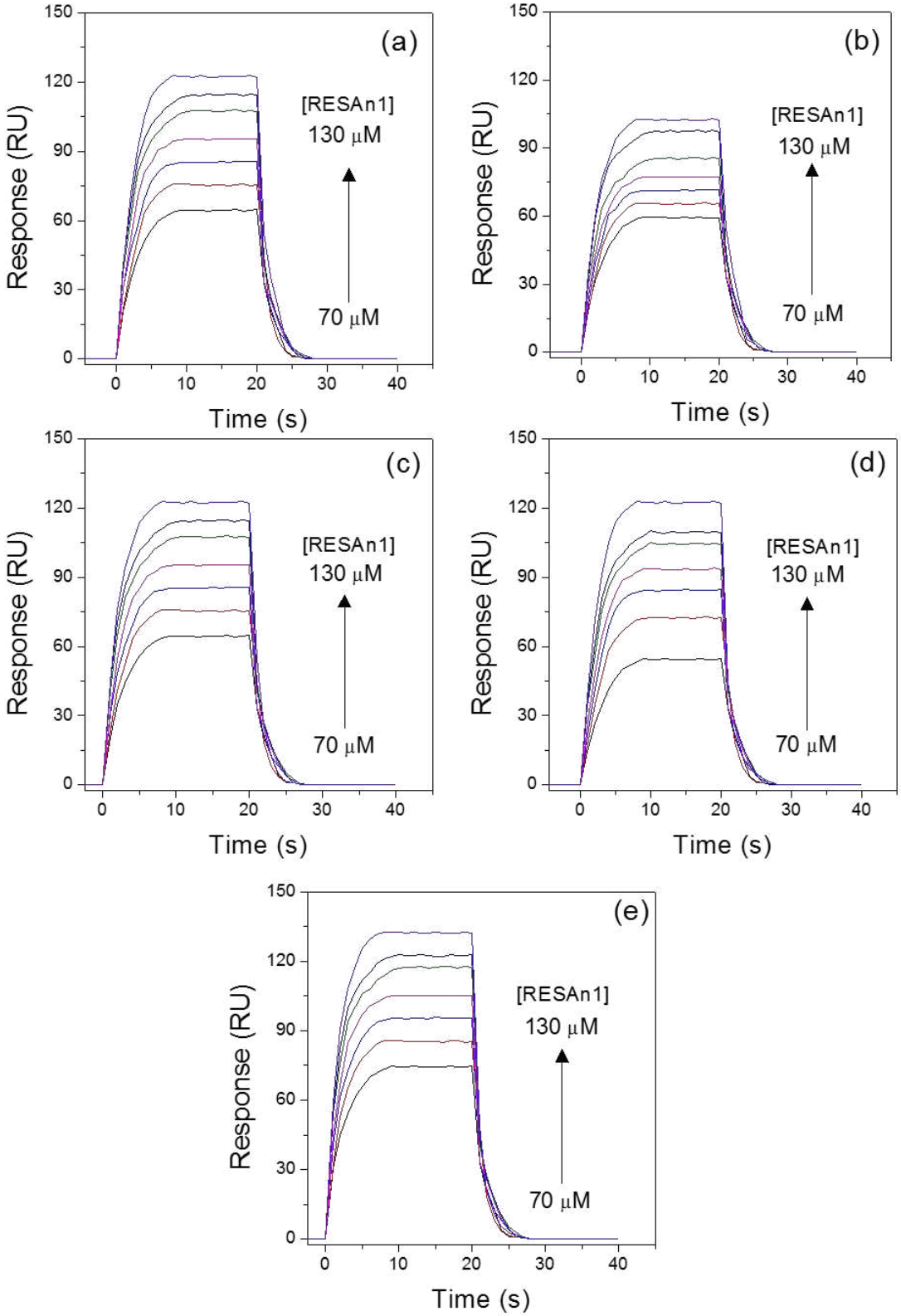

Fig. S4. Sensorgrams (Resonance units - RU vs. Time) for HSA-RESAn1, 70-130 μM RESAn1 solutions flowing over a CM5 low-density HSA-immobilized sensor-chip surface (3893 RU), at (a) 12 °C, (b) 16 °C, (c) 20 °C, (d) 24 °C and, (e) 28 °C. The arrows indicates increasing RESAn1 concentration.

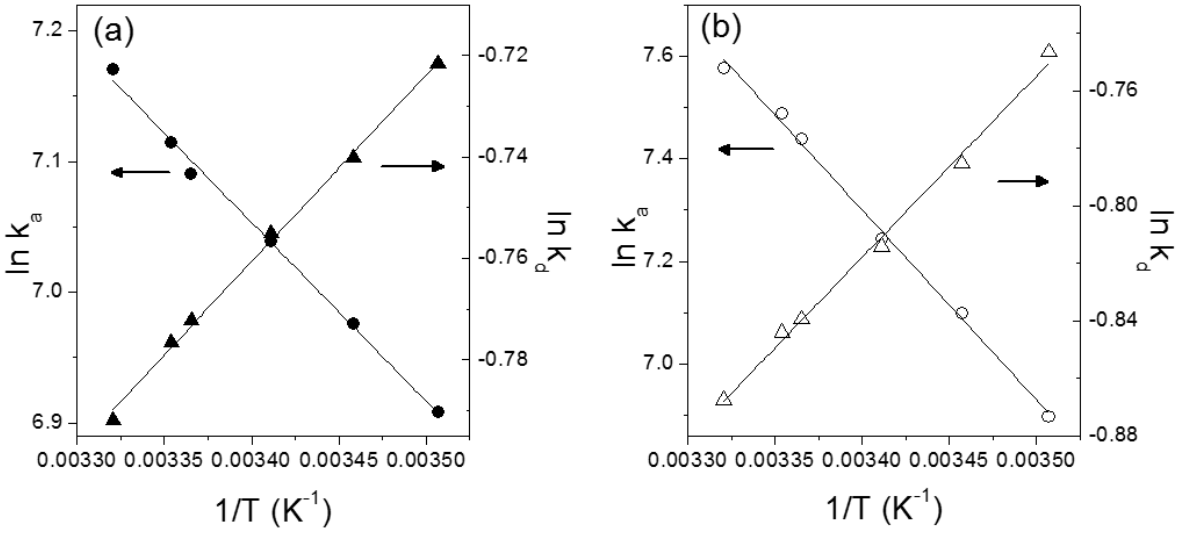

Fig. S5. Arrhenius plots of ln ka (●,○) and ln kd (▲, Δ) *versus* 1/T associated with (a) HSA-RES and (b) HSA-RESAn1 binding. The black lines are the linear fitting, whose determination coefficients (R^2) were higher than 0.99 in all cases.

CONCLUSÕES GERAIS

O nanossensor desenvolvido formado por PDA/ CT/ SDS foi capaz de detectar Enro em meio aquoso em concentrações cerca de cinco vezes menor que o limite máximo permitido pela União Europeia. O estudo da força motriz que causou a mudança colorimétrica do PDA foi importante para verificar que a presença de SDS foi fundamental para aumentar a sensibilidade da nanoblenda. No entanto, a concentração de SDS presente no nanossensor não foi proporcional a sua sensibilidade em razão da influência das interações SDS-SDS e SDS-L64 na energia de barreira rotacional da nanoblenda. A superfície de resposta mostrou que tanto a concentração de ENRO quanto a de SDS influenciaram na taxa de transição colorimétrica, sendo que a nanoblenda contendo 11,6 mM de SDS a 30 ° C gastaria apenas 22 minutos para atingir 40% de CR, que seria facilmente visível. Portanto, essas estruturas são promissoras para a preparação simples e econômica de nanossensores para a detecção de resíduos de antibióticos em diferentes matrizes alimentares.

As técnicas de ressonância plasmônica de superfície (SPR) e espectroscopia de fluorescência (FS) mostraram que bLF e EGCG interagem para formar complexo termodinamicamente estável a pH 7,0. A semelhança entre os parâmetros termodinâmicos obtidos pelas duas técnicas (SPR e FS) indicou que a interação bLF-EGCG ocorreu próximo ao sítio de Trp. A análise cinética da formação do complexo estável entre bLF e EGCG por SPR permitiu obter parâmetros energéticos de formação do complexo ativado bLF-EGCG. A energia de barreira potencial do sistema foi maior para a etapa de associação das moléculas livres (bLF e EGCG) do que para a etapa de dissociação do complexo termodinâmico estável (bLF-EGCG) ($E_{act\,(a)}$ = 49,5 kJ mol^{-1} and $E_{act\,(d)}$ = 17,4 kJ mol^{-1}). No entanto, a formação do complexo ativado a partir da associação de bLF e EGCG foi mais rápida do que da dissociação de bLF-EGCG ($\Delta G_a^{\ddagger}$ = 49.1 kJ mol^{-1} and $\Delta G_d^{\ddagger}$ = 77,9 kJ mol^{-1}). A extensão da mudança conformacional de sítio necessária para formar o complexo ativado foi responsável por essas energias observadas ($T\Delta S_a^{\ddagger}$= -2,10 kJ mol^{-1}; $T\Delta S_d^{\ddagger}$ = -45,10 kJ mol^{-1}). O aumento da temperatura causou aumento nas taxas cinéticas de associação (k_a) e dissociação (k_d), mas em maior intensidade na primeira. Consequentemente, a constante de ligação (K_b) e a estabilidade do complexo foram favorecidas em temperaturas mais altas, evidenciando o papel importante da temperatura na formação e estabilização dos complexos bLF-EGCG.

No estudo da interação do complexo HSA-RES, também foi avaliado a interação da proteína com o análogo RESAn1. Os parâmetros K_b, k_a e k_d indicaram que a HSA interagiu preferencialmente com o análogo RESAn1 (HSA-RESAn1: K_b ~ 3,94 x 10^3 L mol^{-1}, k_a ~ 1,70 x 10^3 M^{-1} s^{-1} e k_d ~ 0,43 s^{-1}; HSA-RES: K_b ~ 2,60 x 10^3 L mol^{-1}, k_a ~ 1,20 x 10^3 M^{-1} s^{-1}, k_d ~ 0,46 s^{-1}). Esses resultados foram atribuídos à menor polaridade do RESAn1 em comparação ao RES, que favoreceu sua entrada nas regiões hidrofóbicas do interior da HSA. A formação dos complexos HSA-RES e HSA-RESAn1 foi dirigida entropicamente ($T\Delta S^0{}_{HSA-RES} \cong$ 33.8 KJ mol^{-1}, $T\Delta S^0{}_{HSA-RESAn1} \cong$ 56.4 KJ mol^{-1}) e, o aumento da temperatura favoreceu a estabilidade do complexo, independentemente do polifenol. Para os dois polifenóis estudados, o custo energético para a formação do complexo ativado a partir da associação das moléculas livres foi maior do que para a dissociação dos complexos estáveis ($E_{act(a)} > E_{act(d)}$). A formação do complexo estável a partir do complexo ativado ocorreu a partir de um grande aumento na entropia do sistema (+80 kJ mol-1), devido à liberação de moléculas de água das camadas de solvatação do sítio de interação do complexo ativado. Esse comportamento foi responsável pela etapa de associação ter sido mais rápida do que a de dissociação ($\Delta G_a^{\ddagger} < \Delta G_d^{\ddagger}$). Esse trabalho mostrou que pequenas diferenças na estrutura de moléculas bioativas, como RES e RESAn1, podem influenciar na termodinâmica e cinética de interação com uma das principais proteínas de transporte sanguíneo.

Assim, fica evidente a importância do estudo das interações intermoleculares entre os componentes que compõem as estruturas supramoleculares para conhecer as condições que otimizam suas funcionalidades. Diante disso, os resultados obtidos nesses trabalhos contribuem para o desenvolvimento de novas tecnologias e aplicações dessas nanoestruturas nas áreas de alimentos, farmacêutica e médica.

REFERÊNCIAS

de Souza, L. C., Rezende, J. de P., Pires, A. C. dos S., da Silva, L. H. M., da Silva, M. do C. H., Castrillon, E. D. C., & de Andrade, N. J. (2016). Polydiacetylene/triblock copolymer nanoblend applied as a sensor for micellar casein: A thermodynamic approach. *Food Chemistry*, *197*, 841–847. https://doi.org/10.1016/j.foodchem.2015.11.071

Faridi Esfanjani, A., & Jafari, S. M. (2016). Biopolymer nano-particles and natural nano-carriers for nano-encapsulation of phenolic compounds. *Colloids and Surfaces B: Biointerfaces*, *146*, 532–543. https://doi.org/10.1016/j.colsurfb.2016.06.053

Foegeding, E. A., Plundrich, N., Schneider, M., Campbell, C., & Lila, M. A. (2017). Protein-polyphenol particles for delivering structural and health functionality. *Food Hydrocolloids*, *72*, 163–173. https://doi.org/10.1016/j.foodhyd.2017.05.024

Gangemi, C. M. A., Puglisi, R., Pappalardo, A., & Trusso Sfrazzetto, G. (2018). Supramolecular complexes for nanomedicine. *Bioorganic & Medicinal Chemistry Letters*, *28*(20), 3290–3301. https://doi.org/10.1016/J.BMCL.2018.09.015

Hu, B., Liu, X., Zhang, C., & Zeng, X. (2017). Food macromolecule based nanodelivery systems for enhancing the bioavailability of polyphenols. *Journal of Food and Drug Analysis*, *25*(1), 3–15. https://doi.org/10.1016/J.JFDA.2016.11.004

Kang, D. H., Jung, H.-S., Ahn, N., Lee, J., Seo, S., Suh, K.-Y., … Kim, K. (2012). Biomimetic detection of aminoglycosidic antibiotics using polydiacetylene–phospholipids supramolecules. *Chemical Communications*, *48*(43), 5313. https://doi.org/10.1039/c2cc31466e

Kwon, D., Lee, H., Yoo, H., Hwang, J., Lee, D., & Jeon, S. (2018). Facile method for enrofloxacin detection in milk using a personal glucose meter. *Sensors and Actuators B: Chemical*, *254*, 935–939. https://doi.org/10.1016/j.snb.2017.07.118

Lehn, J.-M. (2007). From supramolecular chemistry towards constitutional dynamic chemistry and adaptive chemistry. *Chem. Soc. Rev.*, *36*(2), 151–160. https://doi.org/10.1039/B616752G

Mapazi, O., Matabola, P. K., Moutloali, R. M., & Ngila, C. J. (2017). A urea-modified polydiacetylene-based high temperature reversible thermochromic sensor: Characterisation and evaluation of properties as a function of temperature. *Sensors and Actuators B: Chemical*, *252*, 671–679. https://doi.org/10.1016/J.SNB.2017.05.095

Okesola, B. O., & Smith, D. K. (2016). Applying low-molecular weight supramolecular gelators in an environmental setting – self-assembled gels as smart materials for pollutant removal. *Chemical Society Reviews*, *45*(15), 4226–4251. https://doi.org/10.1039/C6CS00124F

Rezaei, A., Fathi, M., & Jafari, S. M. (2019). Nanoencapsulation of hydrophobic and low-soluble food bioactive compounds within different nanocarriers. *Food Hydrocolloids*, *88*, 146–162. https://doi.org/10.1016/J.FOODHYD.2018.10.003

Zhou, J., Li, J., Du, X., & Xu, B. (2017). Supramolecular biofunctional materials. *Biomaterials*, *129*, 1–27. https://doi.org/10.1016/J.BIOMATERIALS.2017.03.014